

POLITECNICO DI TORINO

Corso di Laurea Magistrale
in Ingegneria Civile

Tesi di Laurea Magistrale

Physical and numerical modelling of debris flows



Relatori

Prof. Claudio Scavia

.....

Prof. Marina Pirulli

.....

Candidato

Hervé Vicari

.....

A.A. 2017/2018

Abstract

Debris flows are geohazards consisting of an irreversible deformation of sediment-water mixtures. They have a high destructive potentiality and, therefore, geotechnical engineers have to find effective countermeasures to reduce the risk. The understanding of their behaviour is fundamental to be able to predict the flow and find the best solutions. However, relevant data are difficult to be obtained from natural debris flows: physical modelling is an effective tool to study these mass movements in detail.

Laboratory tests are performed within this thesis. The following issues are analysed:

- Influence of release volume and sediment concentration on the flow behaviour.
- Representativeness of small-scale experiments compared to natural debris flows.
- Numerical simulation of some tests and influence of sediment concentration on the rheological parameters.

Several debris flows are tested on a 5 m long runout channel, sloped 17° , and a 4 m long deposition zone, sloped 2° , aiming at representing 1/20 scale. Height sensors, pore pressure sensors and cameras are used to study the flow. A mixer is used to release the debris mass, avoiding the segregation of water and sediments. The material used in the tests is well graded and mainly made of sand, but with non-negligible contents of gravel and lime.

The peculiar morphological characteristics of debris flows - i.e. longitudinal grain segregation, coarser flow front, liquefied tail, levees formation - are well observed in the experiments. It is found that an increase of sediment concentration decreases the runout distance and the flow velocity. Release volume mainly affects flow height, by increasing it.

The test results are compared to natural debris flows, through Froude number and dimensionless numbers (Savage, Bagnold and friction numbers). High values of Froude number are obtained (from 4, for the highest sediment concentration, to 8, for the lowest sediment concentration), representative of thin and fast flows, compared to natural debris flows with Froude numbers of around 3. The calculation of dimensionless numbers indicates that the three main mechanisms of stress generation (collisional, viscous,

frictional) have the same importance. This is in contrast with natural debris flows, where the frictional behaviour dominates on the viscous one which dominates on collisions. The dimensionless numbers have the same order of magnitude of small-scale experiments found in literature: the overestimation of collisional stresses is therefore a common issue of these laboratory tests. An increase of the importance of the frictional mechanism was however found for the highest solid concentration.

Numerical simulation of these small-scale tests is performed with the RAMMS::DEBRISFLOW software and using the Voellmy rheology. The sensitivity to μ and ξ is analysed: ξ is found to be a turbulent-viscous parameter which mainly affects the flow velocity; μ is a friction parameter which controls the depositional behaviour. The software is able to well simulate the dimensionless parameters along the flume and the runout distance. However, the deposit shape cannot be simulated. The calibrated values of μ and ξ indicate again that the flow is turbulent and with low friction. Finally, the parameter μ is found to be approximately equal to the tangent of the slope angle of the deposition area.

Acknowledgements

First, I would like to thank Professor Steinar Nordal for having accepted me at the Norwegian University of Science and Technology (NTNU) to write my Master Thesis. Next, I would like to thank Professor Vikas Thakur for his continuous supervision of my work. A special thanks to Ashenafi Lulseged Yifru, PhD candidate at NTNU, for his help and guidance during the laboratory experiments and supervision of my thesis. My gratitude also goes to my thesis supervisors, Professor Claudio Scavia and Professor Marina Pirulli, for the useful discussions of my results. Finally, thanks to all my family and all my friends for their encouragements and support.

Hervé Vicari

July 2018

Contents

Abstract	3
Acknowledgements	5
1. Introduction	11
1.1. Debris flows classification	11
1.2. Morphology of debris flows	16
1.2.1. Debris flow characteristics	17
1.3. Physics of debris flows	18
1.3.1. Stress generation	18
1.3.2. Rheological behaviour	19
1.3.2.1. Viscoplastic rheology	19
1.3.2.2. Inertial rheology	22
1.4. Physical modelling	24
1.4.1. Macroscopic scaling	24
1.4.2. Grain-scale mechanics scaling	27
1.5. Numerical modelling	34
1.5.1. Lumped mass models	34
1.5.2. Continuum mechanics models	35
1.5.2.1. RAMMS::DEBRISFLOW model	39
2. Physical modeling and experimental setup	41
2.1. Geometry	44
2.2. Scaling	46
2.3. Debris material	47
2.4. Experiment description	50

2.4.1. Equipment and data processing	52
2.4.2. Test procedure	55
3. Results and analysis	59
3.1. Reference experiment.....	59
3.2. Material G1.....	65
3.3. Runout distance	66
3.4. Deposit shape	68
3.5. Flow velocity.....	69
3.6. Flow height.....	72
3.7. Froude number	75
3.8. Impact pressure.....	76
3.9. Dimensionless parameters	78
3.9.1. Savage number.....	80
3.9.2. Bagnold number.....	81
3.9.3. Friction number	83
3.9.4. Discussion.....	84
4. Numerical simulations of laboratory tests.....	87
4.1. Simulation procedure in RAMMS	87
4.1.1. Simulation procedure and input parameters in RAMMS	87
4.1.2. Output results in RAMMS.....	90
4.2. Influence of Voellmy input parameters on the flow behavior.....	94
4.2.1. Flow behavior	94
4.2.2. Influence of μ and ξ on runout, flow velocity and flow height	95

4.2.3. Influence of μ and ξ on Froude number and dimensionless parameters	99
4.3. Parameter calibration	107
4.4. Discussion	109
5. Conclusions	111
References	113
Appendix 1: results of laboratory flume tests (G2)	119
Appendix 2: results of laboratory flume tests (G1)	120
Appendix 3: deposition shape (G2, repetition 1)	121
Appendix 4: force measurement and impact pressure calculation	123
Appendix 5: calculation of dimensionless numbers	124
Appendix 6: input parameters for RAMMS simulation	126
Appendix 7: results of numerical simulations (RAMMS)	128

1. Introduction

1.1. Debris flows classification

The term debris flow refers to a particular type of landslide, involving the flow, i.e. an irreversible deformation, of sediment-water mixtures. They can originate from the erosion of sediment deposits due to supply of water; from a landslide or from the collapse of a debris dam (Takahashi, 2014).

Several authors have described debris flows and proposed different kinds of classification. The earth scientists mainly treat debris flows through a qualitative explanation of style and rate of movement and morphology and sedimentology of deposits (Pierson et al., 1987). Other scientists have described this natural phenomenon from a more quantitative and physical point of view.

One of the most used landslide classifications was published by Varnes (1958 & 1978), which distinguish mass movements based on two characteristics (Table 1): (i) type of material; (ii) type of movement. In particular, debris flows involve the flow (i.e. fluid-like behaviour) of a predominantly coarse soil (more than 20% of gravel and coarser material); if the flow involves a finer material (less than 20% of gravel and coarser material), it is termed earth flow.

TYPE OF MOVEMENT			TYPE OF MATERIAL		
			BEDROCK	ENGINEERING SOILS	
				Predominantly coarse	Predominantly fine
FALLS			Rock fall	Debris fall	Earth fall
TOPPLES			Rock topple	Debris topple	Earth topple
SLIDES	ROTATIONAL	FEW UNITS	Rock slump	Debris slump	Earth slump
	TRANSLATIONAL		Rock block slide	Debris block slide	Earth block slide
			MANY UNITS	Rock slide	Debris slide
LATERAL SPREADS			Rock spread	Debris spread	Earth spread
FLOWS			Rock flow (deep creep)	Debris flow (soil creep)	Earth flow
COMPLEX			Combination of two or more principal types of movement		

Table 1: Varnes' classification of slope movements (Varnes, 1978)

Coussot et al. (1996) propose a classification based on material type and water content (Figure 1). Debris flows are distinguished from mudflows due to the coarser material. The solid fraction is sufficiently high to carry the sediments in suspension (distinguishing them from hyper-concentrated flows) but low enough to preserve the characteristics of a rapid flow (Coussot et al., 1996).

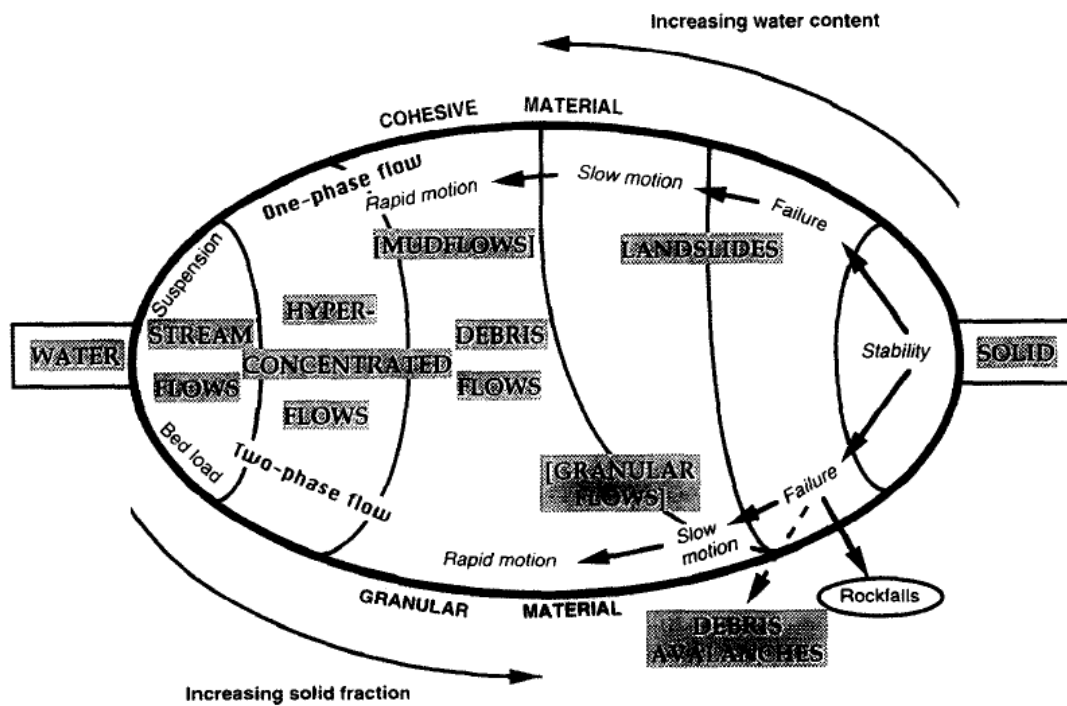


Figure 1: classification of mass movements on steep slopes as a function of solid fraction and material type (Coussot et al., 1996)

Hungr et al. (2001) classify landslides based on material, water content, terrain morphology and velocity. In particular, debris flow is a ‘very rapid to extremely rapid flow of saturated non-plastic debris in a steep channel’ (Hungr et al., 2001). The material is a loose, unsorted soil of low plasticity (Table 2). The velocities range from 1 to 20 m/s (Figure 2). These two criteria, together with the water content, allow to define debris flows (Table 3). Furthermore, debris flows are distinguished from avalanches, due to their motion in a channel.

Origin	Character	Condition ¹	Name
SORTED (marine, lacustrine, fluvial, eolian, volcanic, anthropogenic)	Non-cohesive (Plastic Limit < 5%)	Dry or Saturated	- Gravel - Sand - Silt
	Cohesive (Plastic Limit > 5%)	- Plastic ($I_L < 0.5$) - Liquid ($I_L > 0.5$)	- Clay - Sensitive Clay
UNSORTED (residual, colluvial, glacial, volcanic, anthropogenic)	Non-cohesive (Plastic Limit < 5%)	Dry or Saturated	- Debris ²
	Cohesive (Plastic Limit < 5%)	- Plastic ($I_L < 0.5$) - Liquid ($I_L > 0.5$)	- Earth - Mud
PEAT	Organic	Saturated	- Peat
ROCK	Fragmented	Dry or Saturated	- Rock

Table 2: material involved in landslides of the flow type (Hungr et al., 2001)

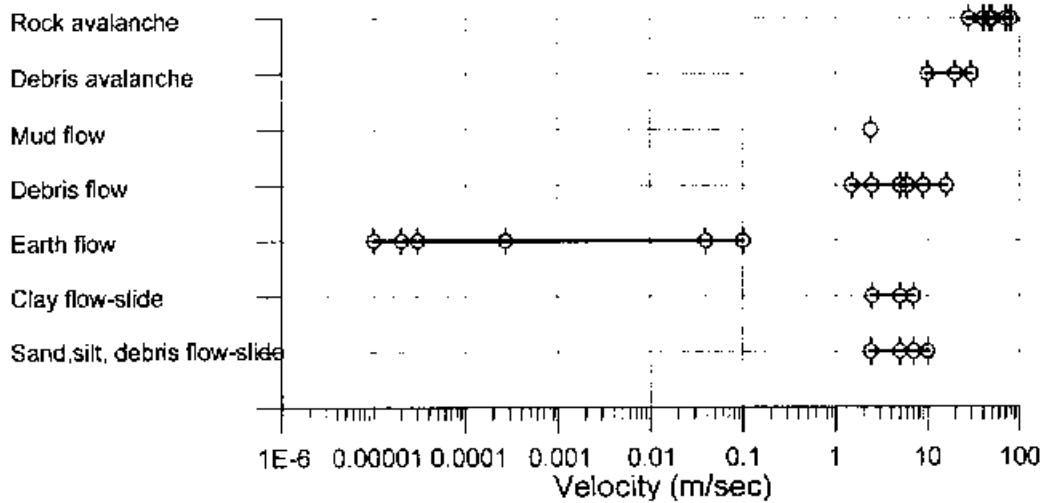


Figure 2: maximum velocities for various types of flow-like landslides, based on observations (Hungr et al., 2001)

Material	Water Content ¹	Special Condition	Velocity	Name
Silt, Sand, Gravel, Debris (talus)	dry, moist or saturated	- no excess pore-pressure, - limited volume	various	Non-liquefied sand (silt, gravel, debris) flow
Silt, Sand, Debris, Weak rock ²	saturated at rupture surface content	- liquefiable material ³ , - constant water	Ex. Rapid	Sand (silt, debris, rock) flow slide
Sensitive clay	at or above liquid limit	- liquefaction <i>in situ</i> , ³ - constant water content ⁴	Ex. Rapid	Clay flow slide
Peat	saturated	- excess pore-pressure	Slow to very rapid	Peat flow
Clay or Earth	near plastic limit	- slow movements, - plug flow (sliding)	< Rapid	Earth flow
Debris	saturated	- established channel ⁵ , - increased water content ⁴	Ex. Rapid	Debris flow
Mud	at or above liquid limit	- fine-grained debris flow	> Very rapid	Mud flow
Debris	free water present	- flood ⁶	Ex. Rapid	Debris flood
Debris	partly or fully saturated	- no established channel ⁵ , - relatively shallow, steep source	Ex. Rapid	Debris avalanche
Fragmented Rock	various, mainly dry	- intact rock at source, - large volume ⁷	Ex. Rapid	Rock avalanche

Table 3: classification of landslides of the flow type (Hungr et al., 2001)

Pierson et al. (1987) propose a classification based on thresholds in rheological behaviour (Figure 3). They distinguish flows according to deformation rate and sediment concentration (the composition of mixture is constant as it is judged less important than sediment concentration). The mean velocity will play a role in the interaction between fluid and sediments and in the mechanisms of stress generation (viscous or inertial). Increasing the sediment concentration will contribute to modify yield strength of the flowing mass. For low concentration the flow behaves as water (Newtonian fluid); then, it will acquire some yield strength (hyperconcentrated streamflows), followed by an abrupt increase in yield strength and the onset of liquefaction behaviour (slurry flow). The loss of the ability to liquefy is linked to the granular flows.

Debris flows correspond to both viscous and inertial slurry flows. Their characteristics are thus those of a plastic flow, with a high yield strength (due to the high sediment concentration), moving as a liquefied mass (Pierson et al., 1987).

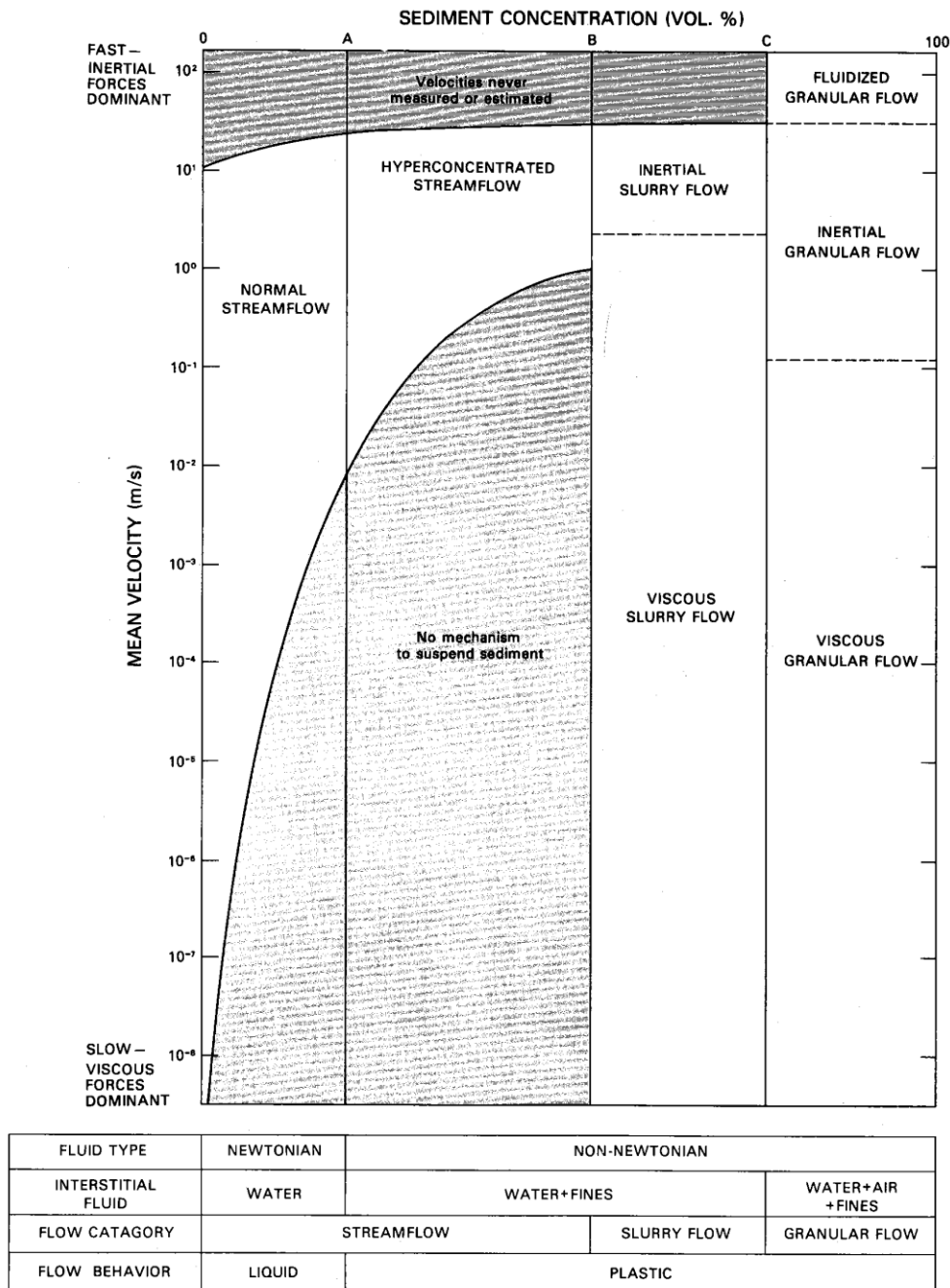


Figure 3: rheologic classification of sediment-water flows (Pierson et al., 1987)

1.2. Morphology of debris flows

A debris flow path comprises an initiation, transport and deposition zone.

The flow can be triggered by several factors. Takahashi (2014) describes three main mechanisms of debris flow generation:

- i. by the erosion of the deposit of the gully bed due to supply of water from outside;
- ii. from a landslide mass;
- iii. sudden burst of a debris dam.

The debris flow process is described in Jakob et al. (2005). Usually, the area of debris-flow initiation has a steep slope, from 20° to 45° (Jakob et al., 2005).

A debris avalanche creates if the rapid initial landslide continue downslope without confinement. If the debris avalanche enters (or originates in) a confined channel (usually steeper than 10°), the phenomenon is more appropriately called debris flow. Erosion may occur, in presence of an erodible soil layer and due to the rapid loading of saturated substrate (Jakob et al., 2005).

Debris flows commonly move as a surge or a series of surges. Surge morphology is depicted in Figure 4. They are characterised by a longitudinal sorting of sediments, which transports the coarser particles and boulders towards the flow front; this one is followed by a finer mass of liquefied debris. Finally, the tail is a dilute, turbulent flow of sediment-charged water (Jakob et al., 2005).

Vertical inverse grading is also a key characteristic of debris flows (Costa, 1984). This can be explained by the high agitation state of the bottom layer which keeps the coarser grains near the free surface of the flow by counteracting their weight: this is sufficient to avoid large grains to drop through voids (Iverson, 1997). This kinetic sieving, together with a vertical velocity gradient (larger longitudinal velocities are recorded at the free surface), produces longitudinal sorting of material (Iverson, 1997).

Deposition, on the so-called debris fan, results from a loss of confinement and a reduction of the slope angle (Jakob et al., 2005). When the flow loses confinement, the slurry flow collapses laterally, cancelling the thrust towards the front. The front slows down, creating elongated levees of coarse material (Jakob et al., 2005). Deposited coarse

material forms a dam (Iverson, 1997), usually characterized by steep fronts and sides (Fisher, 1971). This may be overtaken by the hyper-concentrated, more fluidized, streamflow (Jakob et al., 2005).

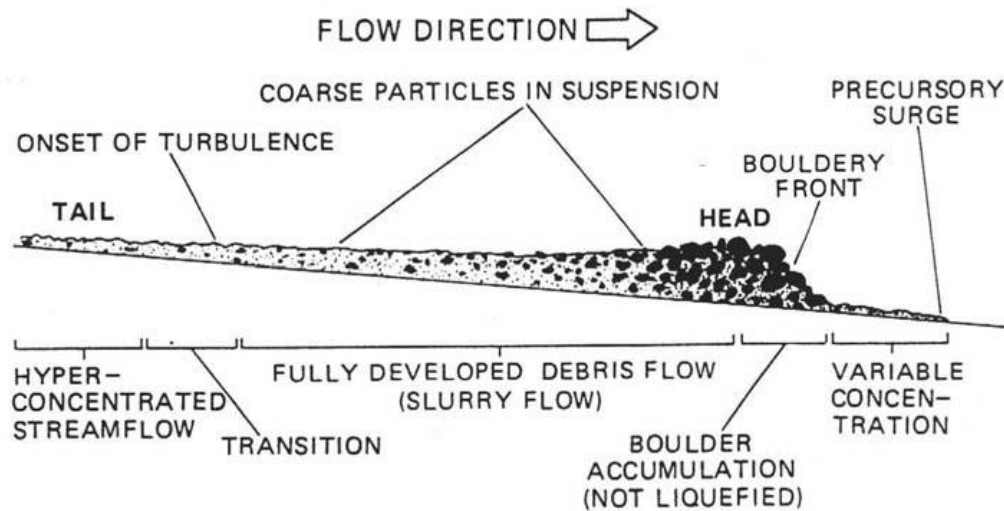


Figure 4: representation of a debris flow surge (Pierson, 1986; adopted from Jakob et al., 2005)

1.2.1. Debris flow characteristics

Physical properties of debris flows are summarized in Table 4 (data from Iverson, 1997).

<i>Property and Unit</i>	<i>Symbol</i>	<i>Typical Values</i>
<i>Solid Grain Properties</i>		
Mass density, kg/m ³	ρ_s	2500–3000
Mean diameter, m	δ	10 ⁻⁵ –10
Friction angle, deg	ϕ_g	25–45
Restitution coefficient	e	0.1–0.5
<i>Pore Fluid Properties</i>		
Mass density, kg/m ³	ρ_f	1000–1200
Viscosity, Pa s	μ	0.001–0.1
<i>Mixture Properties</i>		
Solid volume fraction	v_s	0.4–0.8
Fluid volume fraction	v_f	0.2–0.6
Hydraulic permeability, m ²	k	10 ⁻¹³ –10 ⁻⁹
Hydraulic conductivity, m/s	K	10 ⁻⁷ –10 ⁻²
Compressive stiffness, Pa	E	10 ³ –10 ⁵
Friction angle, deg	ϕ	25–45

Table 4: physical properties of debris flows (Iverson, 1997)

1.3. Physics of debris flows

Iverson (1997) identifies several fundamental aspects of debris flows:

- i. Contemporary presence of solid and fluid forces and their interaction.
- ii. Longitudinal segregation: coarse-grained fronts lack pore pressures; finer-grained tail is nearly liquefied. The presence of fluid pore pressures reduces the effective stresses and, thus, increases the debris flows mobility.
- iii. Vertical inverse grading.
- iv. Unsteady surge dynamics.
- v. Grain fluctuation energy: instantaneous grain velocities differ from their mean velocity. This produce agitation in the flowing debris.

1.3.1. Stress generation

The presence of two phases, i.e. liquid and solid, creates a peculiar physical behaviour in debris flows and affects the mechanisms of momentum transport. Iverson and Denlinger (1987) describe five mechanisms of shear stress generation during steady, simple shearing of an unbounded, uniform mixture of identical, dense spherical grains and Newtonian fluid:

- i. Solid inertial stress:

$$T_{s(i)} = v_s \rho_s \dot{\gamma}^2 \delta^2 \quad (1)$$

It is transmitted by grain collisions.

- ii. Fluid inertial stress:

$$T_{f(i)} = v_f \rho_f \dot{\gamma}^2 \delta^2 \quad (2)$$

It is associated to fluid turbulence.

- iii. Quasi-static solid stress:

$$T_{s(q)} = N v_s (\rho_s - \rho_f) g \delta \tan \varphi \quad (3)$$

It is associated with Coulomb sliding and enduring grain contacts.

iv. Quasi-static fluid stress:

$$T_{s(f)} = v_f \dot{\gamma} \mu \quad (4)$$

It corresponds to viscous stress of a Newtonian fluid.

v. Solid-fluid interaction stress:

$$T_{s-f} = \frac{\dot{\gamma} \mu \delta^2}{k} \quad (5)$$

It derives from grain-scale fluid flow.

Where: v_s is the volumetric sediment content; v_f is the volumetric water content; ρ_s is the bulk density of the solid grains; ρ_f is the fluid bulk density; $\dot{\gamma}$ is the rate of shear strain; δ is the grain diameter; N is the number of grains above the layer of interest; φ is the friction angle; g is the magnitude of gravity acceleration; k is the hydraulic permeability; μ is the dynamic viscosity of intergranular fluid.

As it will be discussed later, based on the boundary conditions, some stresses may dominate on the others. Furthermore, stress generation processes may be different between the flow front and the tail (Iverson, 1997).

1.3.2. Rheological behaviour

To overcome the difficulties related to a double-phase material, debris flows can be considered as an equivalent continuum single-phase fluid. The main models consider viscoplastic and inertial rheologies.

1.3.2.1. Viscoplastic rheology

Viscoplastic models relate shear stress (τ) to strain rate ($\frac{du}{dy}$) (Figure 5). The behaviour can be Newtonian or non-Newtonian, depending on sediment type, particle size distribution and sediment concentration (Pierson and Scott, 1985).

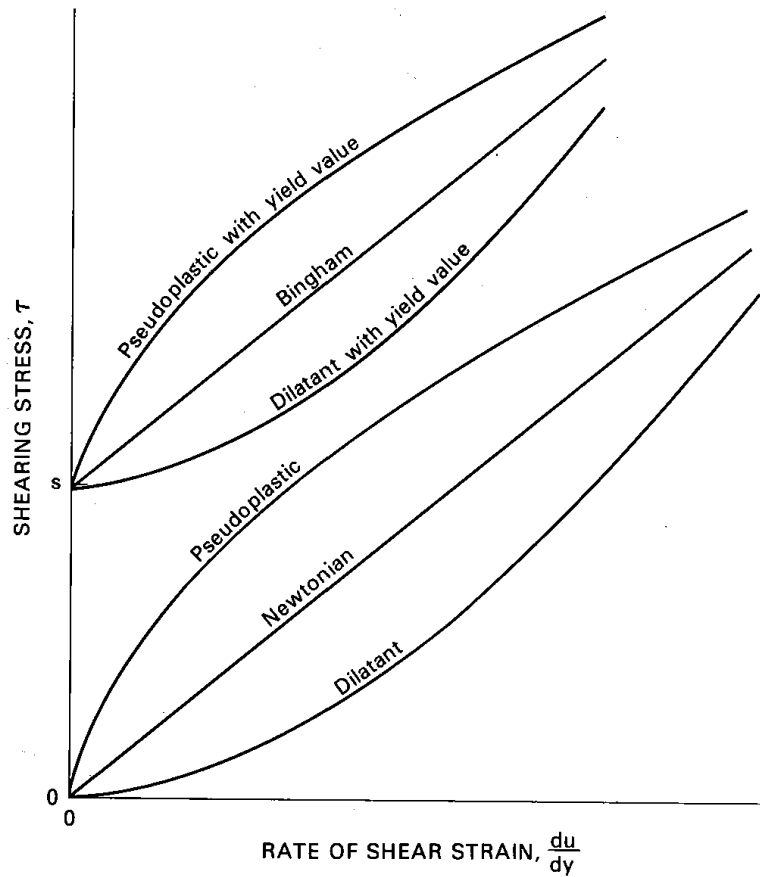


Figure 5: viscoplastic rheological models (Pierson and Costa, 1987)

For a Newtonian fluid this relationship is linear and their ratio is called viscosity:

$$\tau = \mu \frac{du}{dy} \quad (6)$$

Where μ is the viscosity, u is the velocity and y is the flow depth.

Fluids with a negligible content of clay and silt show a Newtonian behaviour till sediment concentrations as high as 50% (Rodine et al., 1974).

Viscosity is also a function of sediment concentration, and in particular increases with it (Fisher, 1971), as shown in Figure 6. Furthermore, it increases with the ratio of cohesive to non-cohesive particles (Fisher, 1971).

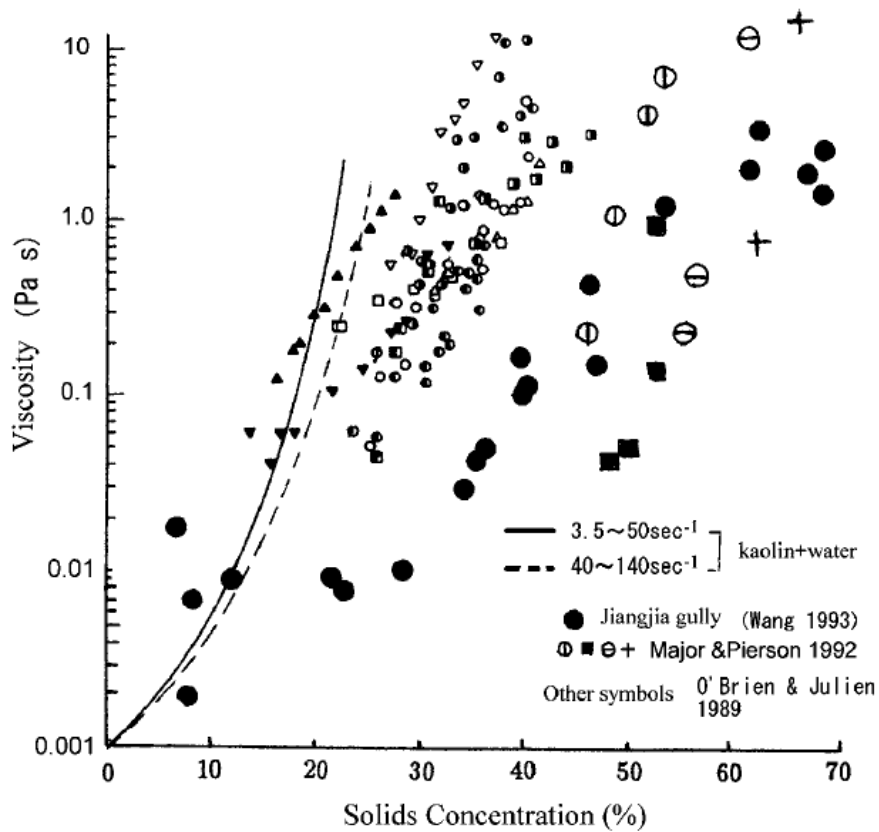


Figure 6: increasing viscosities with increasing solid concentrations (Takahashi, 2014)

A pseudoplastic (shear thinning) fluid exhibits a decreasing viscosity with increasing rate of shear strain (Pierson and Costa, 1987). A dilatant fluid (shear thickening) has an increasing viscosity with increasing rate of shear strain (Pierson and Costa, 1987).

The fluid acquires a non-negligible yield strength (τ_y), i.e. the stress that has to be overcome for flow to occur, for increasing amounts of clay and silt and for increasing sediment concentrations (Pierson and Costa, 1987; Figure 7). This kind of materials can be modelled with a Bingham rheology:

$$\tau = \tau_y + \mu \frac{du}{dy} \quad (7)$$

This yield strength is provided by cohesive forces (Pierson and Costa, 1987) supported by the fine material. For coarse materials, the yield strength is due to the friction between the particles (sliding friction and interlocking), which contributes to the strength provided by cohesive particles and viscosity of the fluid (Pierson and Scott, 1985).

For clay and water mixtures, Sosio et al. (2007) and De Blasio et al. (2011) found experimentally an exponential relationship between the clay content and the yield stress.

Considering that debris flows are made of poorly sorted materials and that they usually exhibit solid concentrations higher than 40%, Bingham rheology looks more appropriate than Newtonian rheology. This is demonstrated by the steep fronts and sides of debris flow deposits (Fisher, 1971) and by the thick deposits on steep slopes (Calligaris and Zini, 2012).

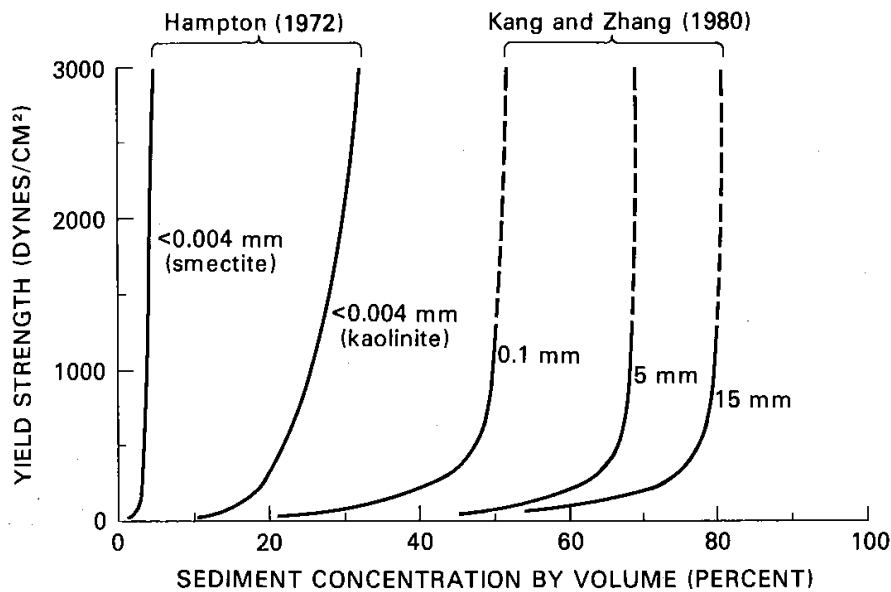


Figure 7: influence of sediment concentration and particle size on yield strength (Pierson and Scott, 1985)

1.3.2.2. Inertial rheology

Bagnold (1954) showed that inertial grain flow is characterized by a direct proportionality between the shear stress and the square of shear rate.

Inertial grain flow is related to the granular temperature, introduced by Ogawa (1978). In an agitated grain flow, the instantaneous velocity of solid particles (v_s) will differ from their mean velocity (\bar{v}_s). Granular temperature is hence defined as (Iverson, 1997):

$$T = \langle (v_s - \bar{v}_s)^2 \rangle \quad (8)$$

Where the brackets indicate an average.

Iverson (1997) discusses the effects of granular temperature on the flow behaviour. A higher granular temperature reduces bulk density, enhancing the flow. However, higher velocities imply greater energy dissipations.

Theoretical considerations demonstrate that shear stress depend on the fluid density and on the square of velocity. Dimensional analysis shows that the following relationship is valid:

$$\tau = \rho g \frac{v^2}{\zeta} \quad (9)$$

Where ζ is a coefficient of turbulence.

As it will be discussed in the following chapters, inertial flow dominates on viscous flow for coarse material and high shear rates.

Another model taking into account turbulence is the Voellmy rheology, which comprises a frictional and a turbulent term:

$$\tau = \rho g \left(h \cos\vartheta \tan\varphi_a + \frac{v^2}{\zeta} \right) \quad (10)$$

Where ϑ is the slope angle and φ_a is the apparent friction angle, i.e. it takes in account the effect of pore water pressure: $\tan\varphi_a = (1 - r_u)\tan\varphi'$ where r_u is the ratio between pore water pressures and total stress and φ' is the angle of shear strength.

Frictional effects dominate at slow shear rates, while turbulence is predominant at high shear rates and at moderate solid concentrations (Savage and Hutter, 1989).

1.4. Physical modelling

Physical modelling assumes a noteworthy importance in the case of debris flows, due to the practical difficulty to study natural events. In this sense, physical modelling permits to completely observe the phenomenon and its morphology, to validate rheological laws (Viccione et al., 2015) and to study how the flow is influenced by initial and boundary conditions.

Similitude between the model and the prototype must exist to well represent the natural debris flows. Two kinds of scaling are necessary (Iverson et al., 2010): that for flow as a whole (where the length scales are the height H and the length L of the flow) and that for grain-scale mechanics that generate stresses (where the length scale is a characteristic diameter δ of the particles).

1.4.1. Macroscopic scaling

The macroscopic scaling of the flow as a whole can be obtained by listing the relationship between the dynamic variables (velocity u and the typical stress τ):

$$(u, \tau) = f(g, L, H, \delta, \rho, \rho_s, \rho_f, D, \mu, \tau_y, \varphi_{int}, \varphi_{bed}, c, E, e, \vartheta) \quad (11)$$

Where: g is the magnitude of gravity acceleration, ρ is the bulk density of the debris material, ρ_s is the bulk density of the solid grains, ρ_f is the fluid bulk density, D is the hydraulic diffusivity of grain-fluid mixture, μ is the dynamic viscosity of intergranular fluid, τ_y is the fluid yield strength, φ_{int} is the internal friction angle of granular mass, φ_{bed} is the basal friction angle, c is the intergranular cohesion, E is the bulk compressive stiffness of the debris material, e is the restitution coefficient of colliding grains, ϑ is the bed slope angle. Scaling adopted by Iverson et al. (2004) and Iverson et al. (2010) leads to the following dimensionless equation:

$$\left(\frac{u}{\sqrt{gH}}, \frac{\tau}{\rho g H} \right) = f \left(\frac{L}{H}, \frac{\delta}{H}, \frac{\rho_s}{\rho}, \frac{\rho_f}{\rho}, \frac{D}{H^{\frac{3}{2}} g^{\frac{1}{2}}}, \frac{\mu}{\rho H^{\frac{3}{2}} g^{\frac{1}{2}}}, \frac{\tau_y}{\rho g H}, \frac{c}{\rho g H}, \frac{E}{\rho g H}, \varphi_{int}, \varphi_{bed}, e, \vartheta \right) \quad (12)$$

Between the variables on the right-hand side of this equation, 3 categories can be recognized: (i) intrinsically dimensionless variables (in this case, a material with similar properties should be used in the laboratory), (ii) density and length ratios, (iii) dynamic scale effects.

The equation can be rewritten considering only the dynamic variables (Iverson et al., 2004):

$$\left(\frac{u}{\sqrt{gL}}, \frac{\tau}{\rho gH} \right) = f_{scale}(N_P, N_R, Y, c^*, E^*) \quad (13)$$

Where:

- $N_P = \frac{\sqrt{L}}{\frac{\mu H^2}{\kappa E}}$ (14) is a timescale ratio between the time of debris flow motion and the

time for excess pore pressure diffusion.

- $N_R = \frac{\rho H \sqrt{gL}}{\mu}$ (15) is similar to the Reynolds number and is the ratio between inertial and viscous effects.

- $Y = \frac{\tau_y}{\rho gH}$ (16) is the fluid yield strength normalized by the characteristic stress.

- $c^* = \frac{c}{\rho gH}$ (17) is the intergranular cohesion normalized by the characteristic stress.

However, Iverson et al. (2010) propose another scaling: cohesion is not assumed to play a role and therefore c is replaced by the solid phase basal shear stress which is obtained from the Coulomb effective friction. In this case, c^* has no, or little, scale dependence.

- $E^* = \frac{E}{\rho gH}$ (18) is the bulk stiffness normalized by the characteristic stress.

As shown in Figure 8, in a small-scale experiment, the effects of pore pressures will be lower, but the influence of viscosity, bulk stiffness, cohesion and fluid yield strength will be more important than in a full-scale flow. Therefore, miniature sediment-water experiments may neglect pore pressure effects and overestimate viscous effects, which is the opposite of nature-scale debris flows (Denlinger and Iverson, 2001).

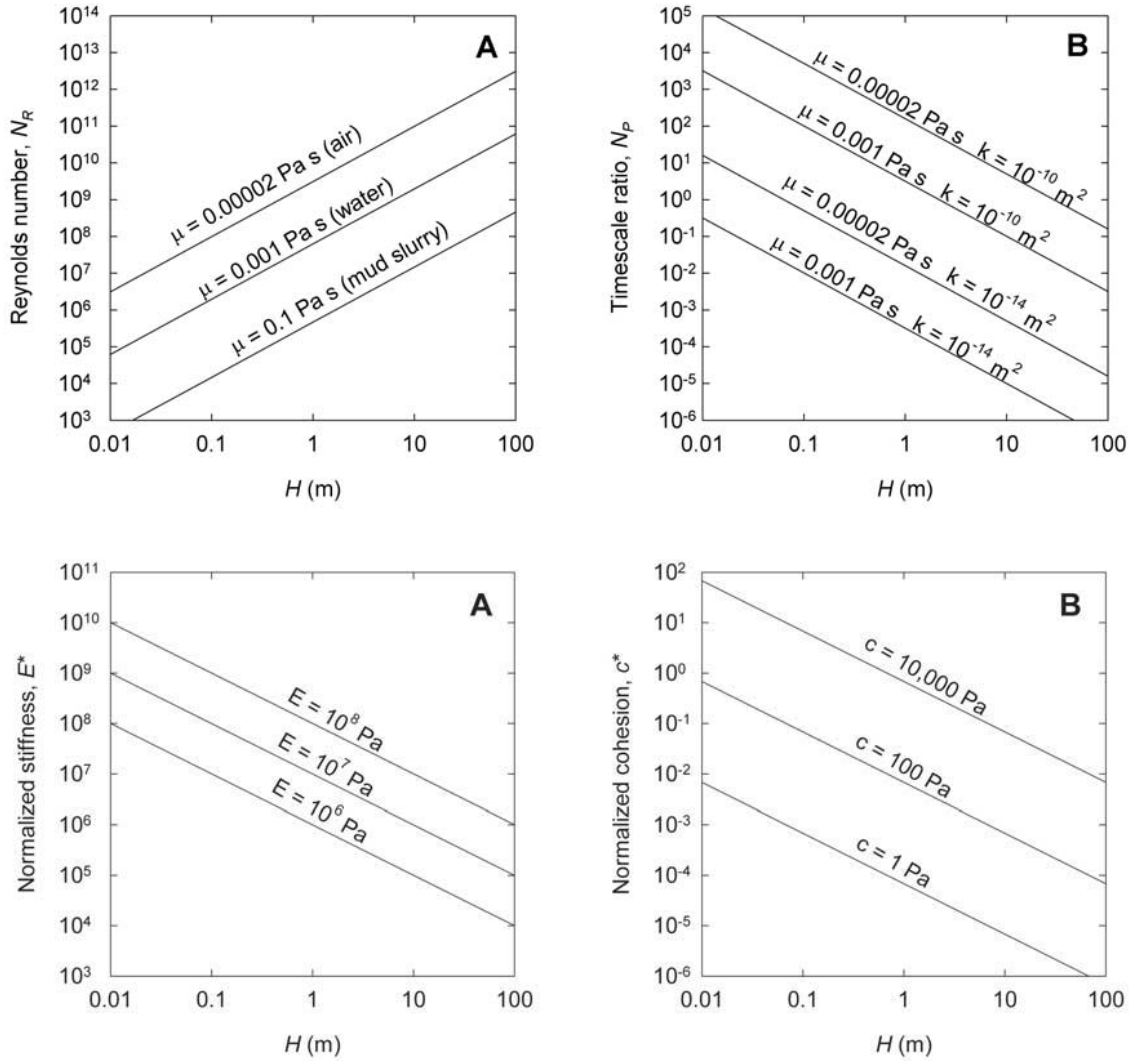


Figure 8: graphs of the dynamic variables as a function of the flow height (Iverson et al., 2004)

From a practical point of view, it is necessary to verify if laboratory experiments effectively well describe the natural phenomenon. A length scale is initially chosen to represent a certain type of debris flow:

$$\lambda = \frac{L_{model}}{L_{nature}} \quad (19)$$

Where L_{model} is a typical length of the debris flow in the model (from the source to the end of the deposit) and L_{nature} is a typical length of debris flows in nature.

To maintain the geometric similarity, the ratio between the flow height and length should be constant between the model and the prototype. It follows that the ratio between the flow heights is:

$$\frac{H_{model}}{H_{nature}} = \lambda \quad (20)$$

It is subsequently necessary to verify if kinematic similitude between the model and the prototype is maintained. In the case of debris flows, gravitational forces primarily influence the mass movement; therefore, Froude number is used to verify this similitude (Crowe et al., 2009):

$$Fr = \frac{u}{\sqrt{gL}} \quad (21)$$

It follows that the ratio between the velocities is:

$$\frac{u_{model}}{u_{nature}} = \sqrt{\lambda} \quad (22)$$

Iverson et al. (2010) consider that high clay contents and slope roughness are key factors to simulate real debris flows by small scale experiments.

Furthermore, also dynamic similarity, as the ratio between model and nature forces, should be verified (Crowe et al., 2009; Coussot and Meunier, 1996).

1.4.2. Grain-scale mechanics scaling

Considering the mechanisms of shear stresses generation described in paragraph 1.3.1., it is possible to define dimensionless numbers (Iverson, 1997), as the ratio between stresses:

i. Savage number:

$$N_{sav} = \frac{T_{s(i)}}{T_{s(q)}} = \frac{\gamma^2 \rho_s \delta}{N(\rho_s - \rho_f) g \tan \varphi} \quad (23)$$

It describes the dominance of grain collisions on the friction due to the weight of the granular mass.

ii. Bagnold number:

$$N_{Bag} = \frac{T_{s(i)}}{T_{f(q)}} = \frac{v_s}{1 - v_s} \frac{\rho_s \delta^2 \dot{\gamma}}{\mu} \quad (24)$$

It represents the importance of grain collisions over viscous fluid forces.

iii. Mass number:

$$N_{mass} = \frac{T_{s(i)}}{T_{f(i)}} \quad (25)$$

iv. Darcy number:

$$N_{Dar} = \frac{T_{s-f}}{T_{s(i)}} \quad (26)$$

It characterizes the tendency of pore fluid pressures to moderate the interactions between colliding grains.

v. Reynolds Number:

$$N_{Rey} = \frac{T_{f(i)}}{T_{f(q)}} \quad (27)$$

vi. Friction number:

$$N_{fric} = \frac{T_{s(q)}}{T_{f(q)}} = \frac{v_s}{1 - v_s} \frac{N(\rho_s - \rho_f)g\delta \tan\varphi}{\mu \dot{\gamma}} \quad (28)$$

Iverson (1997) provide some guidelines to identify the thresholds between the different behaviors:

- In dry granular flows, grain collisions dominate grain friction if $N_{Sav} > 0.1$ (Savage and Hutter, 1989). Natural debris flows have a typical value of $N_{Sav} = 10^{-6}$ (from the data of Iverson, 1997).

- In neutrally buoyant mixtures of spherical grains and liquid, collisional stresses dominate viscous stresses if $N_{Bag} > 200$. Natural debris flows have a typical value of $N_{Bag} = 1$ (from the data of Iverson, 1997).
- Transition from viscous to frictional behaviour at $N_{fric} > 1400$ (Iverson and LaHusen, 1993). Natural debris flows have a typical value of $N_{fric} = 10000$ (from the data of Iverson, 1997).
- Inertial fluid effects dominate on fluid viscosity from $N_{Rey} > 1$.
- Solids and fluids strongly interact for $N_{Dar} > 1000$.

Dimensionless numbers have been estimated by Iverson (1997) for the USGS debris flow experiment and for some natural debris flows (Table 5). Data obtained from laboratory experiments (at large scale, as in the USGS experiment, Major, 1997 and at small scale, as Braat, 2014) show that collision stresses dominate, but also friction and viscosity contribute (Iverson, 1997). Thus, small-scale experiments overestimate the collisional stresses transmitted by the coarse fraction and underestimate the importance of friction versus viscosity.

Parameter	Debris Flow Prototype			
	USGS Flume Experiment (Sand-Gravel)	Oddstad Debris Flow (Figure 1), Jan. 4, 1982	South Toutle River, May 18, 1980	Osceola Mudflow, circa 5700 B.P.
<i>Dimensional Parameters</i>				
δ , m	0.001*	0.001*	0.001*	0.001*
$h = N\delta$, m	0.1	1	5	20
v , m/s	10	10	20	20
$\dot{\gamma}$, 1/s	100	10	4	1
ρ_s , kg/m ³	2700	2700	2700	2700
ρ_f , kg/m ³	1100	1100	1100	1200
μ , Pa s	0.001	0.01*	0.01*	0.1*
g , m/s ²	9.8	9.8	9.8	9.8
k , m ²	10^{-11}	10^{-11} *	10^{-12}	10^{-12}
E , Pa	10^4 *	10^4 *	10^4 *	10^4 *
v_s	0.6	0.6	0.6	0.6
v_f	0.4	0.4	0.4	0.4
ϕ , deg	40	30	30	30
<i>Dimensionless Parameters</i>				
N_{Sav}	0.2	2×10^{-4}	6×10^{-6}	1×10^{-7}
N_{Bag}	400	4	0.2	0.4
N_{mass}	4	4	4	4
N_{Dar}	600	60,000	2×10^6	6×10^7
N_{Rey}	100	1	0.04	0.01
N_{fric}	2×10^3	2×10^4	3×10^4	4×10^5

Table 5: typical values of dimensionless numbers for laboratory tests and natural debris flows (Iverson, 1997)

Braat (2014) analyses the influence of the debris composition on the stress generation processes (Figure 9):

- N_{Bag} increases for larger coarse material content and decreases for larger clay content.

For clay contents lower than 10%, collisional stresses dominate on fluid viscosity, due to the high shear rates that develops in thin, fast flows.

- N_{Sav} decreases for high clay and coarse contents. The last trend is explained to depend on the friction developed at the flow front. In all the experiments grain collisions dominate on friction.

- N_{fric} increases with the coarse material content and decreases for clay contents higher than 5%, since clay increases viscosity. In general, the friction number is low, indicating that friction is less important than viscosity.

- N_{mass} decreases with clay content.

- N_{Dar} increases with clay content; for a clay content higher than 5% approximately, the fluid prevents grain collisions.

- N_{Rey} increases with the coarse material and decreases with the clay content. In the case of small-scale experiments, contrary to full-scale debris flows, inertial fluid effects are more important than viscosity.

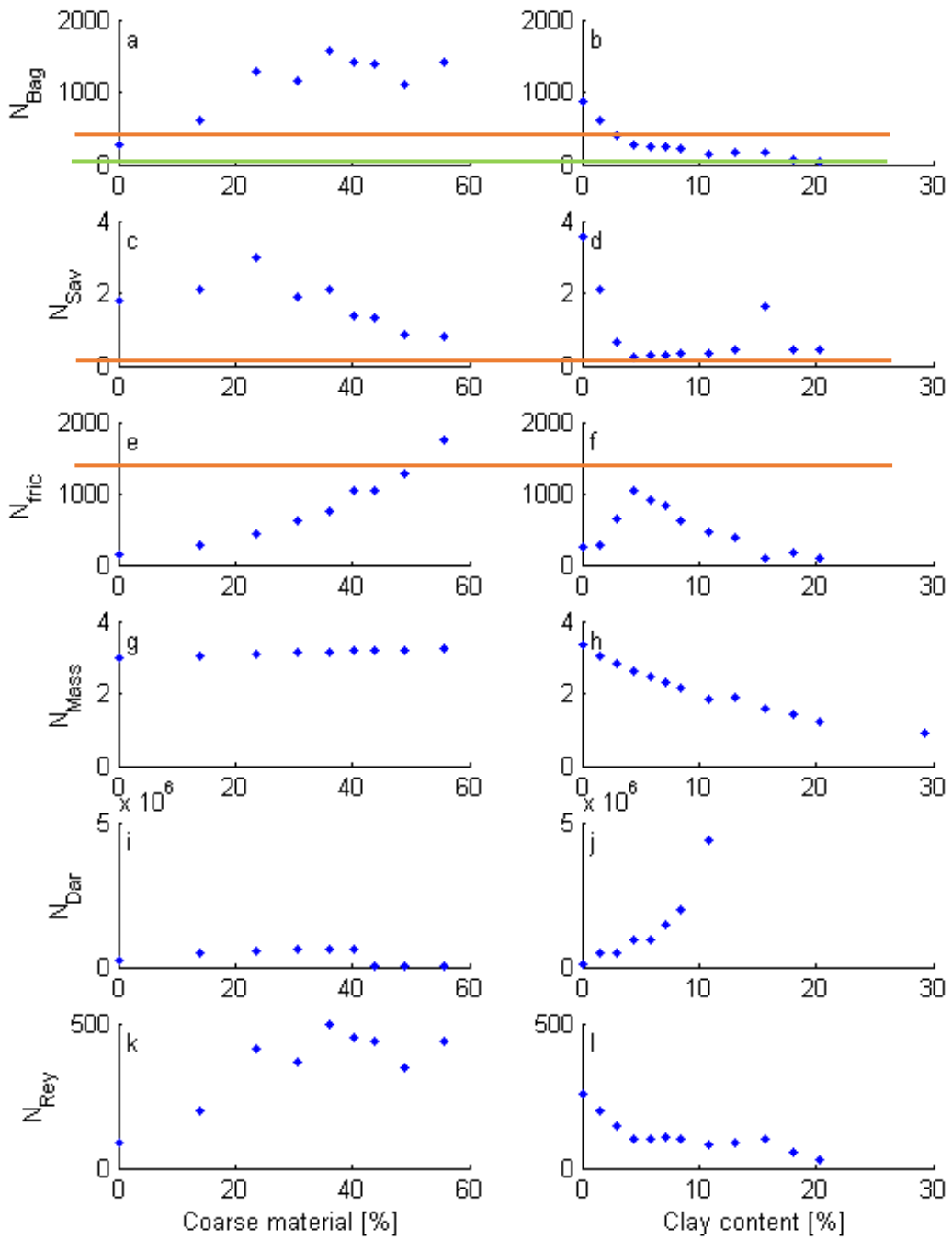
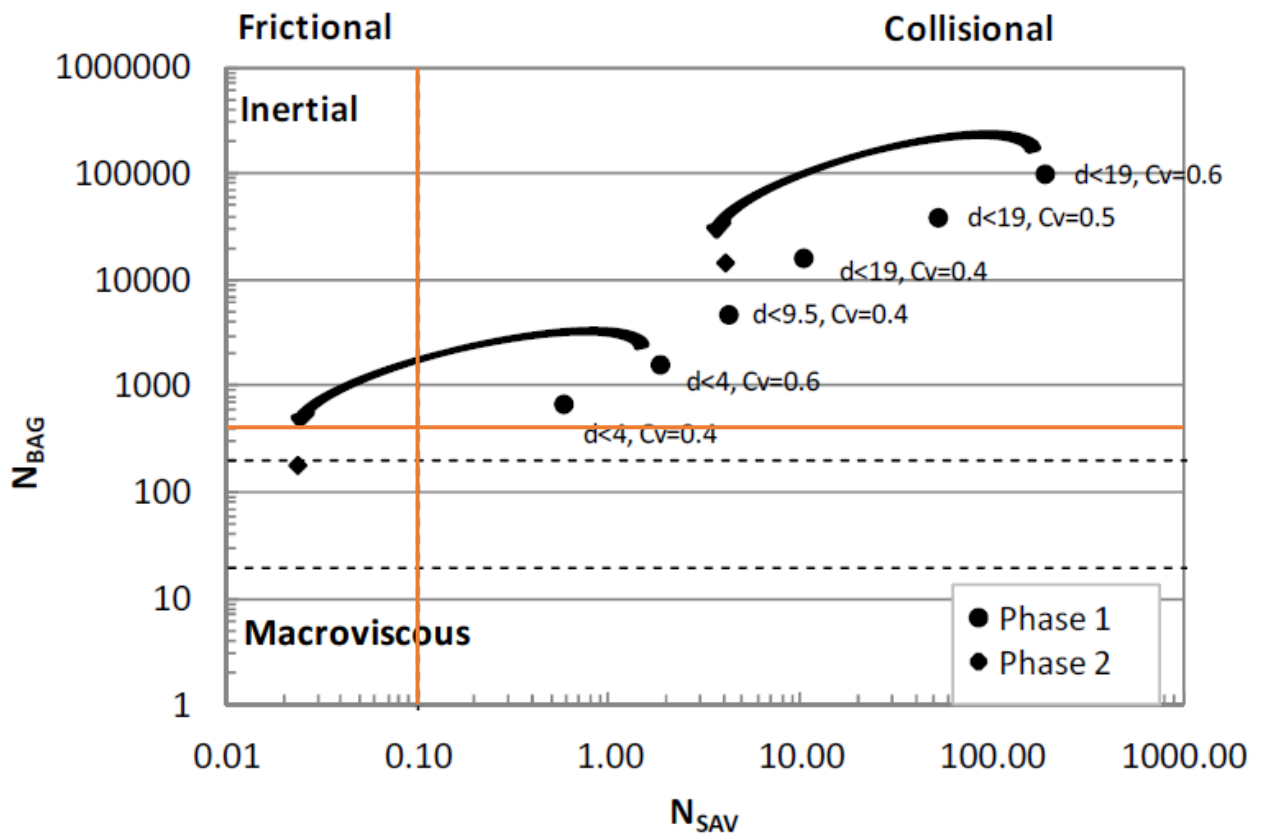


Figure 9: experimental results of Braat (2014). Orange lines represent the transition between stress generation processes. Green lines represent an order of magnitude of the values observed in real debris flows

Battella et al. (2012) performed laboratory tests on a debris material made of limestone fragments in a sandy-silt matrix, to study the influence of sediment concentration and grain diameter on the stress generation processes (Figure 10).

It is observed that collisional stresses dominate in almost all the tests. A macroviscous regime is approached by decreasing the sediment concentration and with finer material. Frictional stresses might contribute, and also prevail on other stresses, during the depositional process, if the solid concentration is high enough (0.6) to allow the segregation process.



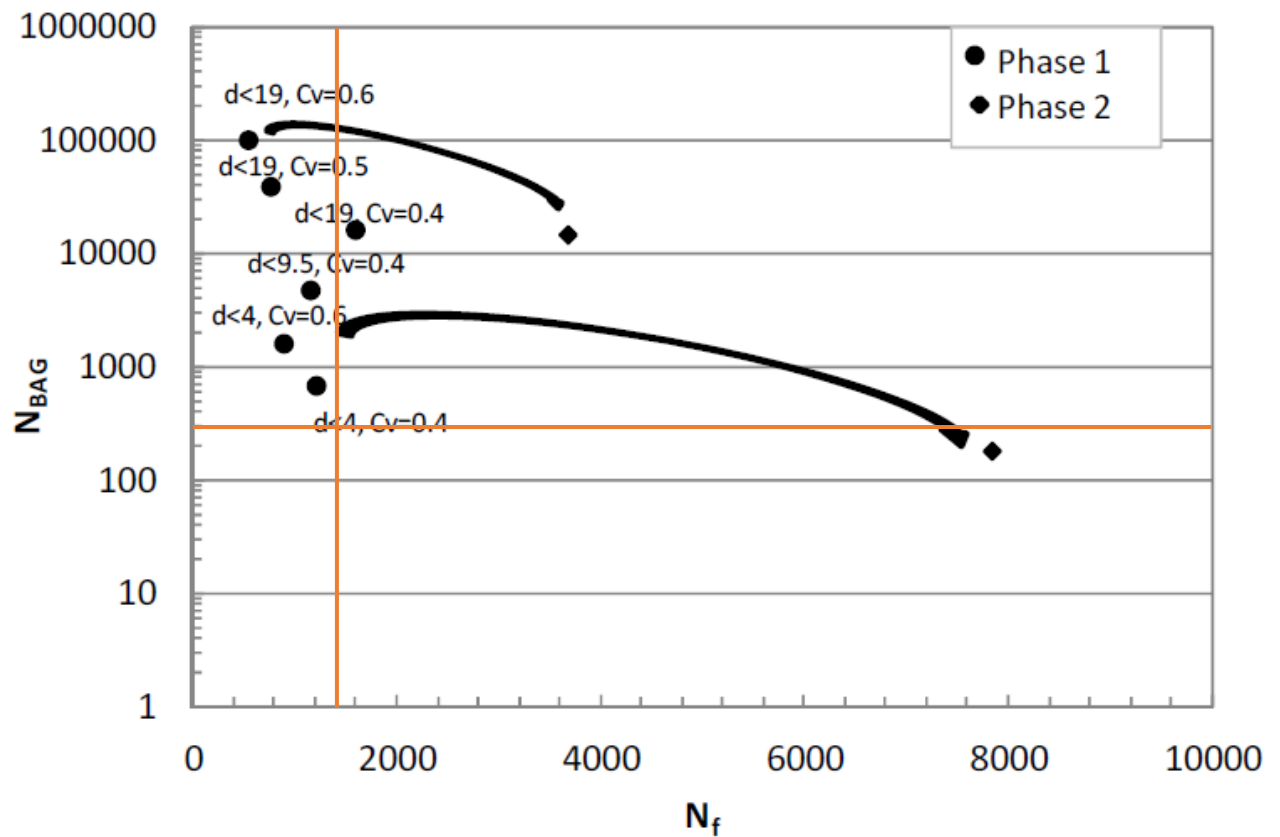


Figure 10: experimental results of Battella et al. (2012). Orange lines represent the transition between stress generation processes.

Parsons et al. (2001) conducted a series of experiments on a 10 m long slope and concluded that viscous stresses dominate. However, frictional behaviour is also observed at the snout (in this work, the onset of frictional regime over viscous one is observed to be at friction number equal to 100, for the body, and 250, for the snout), as a result of coarse particles segregation and low water content. The inertial regime is generally not observed (corresponding to low values of Bagnold and Savage numbers) and it is explained by the high viscosity of the slurry as a result of ‘‘the poorly sorted, highly angular makeup of the constituent silts and the presence of a minor but nonnegligible amount of clay’’ (Parsons et al., 2001).

Holmes (2017) showed that also the slope angle influence stress generation processes. Flatter slopes will produce lower velocities and thus lower Savage and Bagnold numbers but a higher friction number.

1.5. Numerical modelling

Analytical and numerical approaches are fundamental for the simulation of debris flows, since they allow to analyse the flow runout for risk assessment and design of remedial measures (Hung, 1995). Three main analytical approaches have been developed: lumped mass models and models based on continuum and discontinuum mechanics.

1.5.1. Lumped mass models

Lumped mass models idealize the motion of the whole debris mass as a single mass point, without considering the internal deformation (Pirulli, 2005). Energetic balance of the centre of mass of the slide allows to predict some runout characteristics.

The debris mass, prior the movement takes place, has a potential energy mgh . As it propagates downslope, it will lose energy, due to the dissipation mechanisms described in the previous sections, but it will gain kinetic energy due to the conversion of the potential energy. Considering the scheme of Figure 11, the kinetic energy at a generic distance x from the source can be found from the energy balance:

$$E_p(x = 0) = mgh = E_p(x) + E_k(x) + E_L(x) = mgh(x) + \frac{1}{2}mv(x)^2 + E_L(x) \quad (29)$$

Where E_p is the potential energy, E_k is the kinetic energy and E_L is the energy loss during motion. The energy loss will depend on the resisting force considered in the model. If a frictional stress is assumed, the energy loss is equal to:

$$E_L(x) = mgx \tan \delta_a \quad (30)$$

Where δ_a is an apparent friction angle taking into account the effective friction angle of the material (φ') and the existence of pore fluid pressures which decrease the effective stress. A total stress approach is in fact considered to derive (30) because the mass is

treated as an equivalent single-phase material. The shear resisting stress, which causes energy loss, is related to the normal effective stress through the Coulomb equation:

$$\tau = \sigma'_n \tan \varphi' = \sigma_n (1 - r_u) \tan \varphi' = \sigma_n \tan \delta_a \quad (31)$$

Where $r_u = \frac{u}{\sigma_n}$, u is the pore pressure.

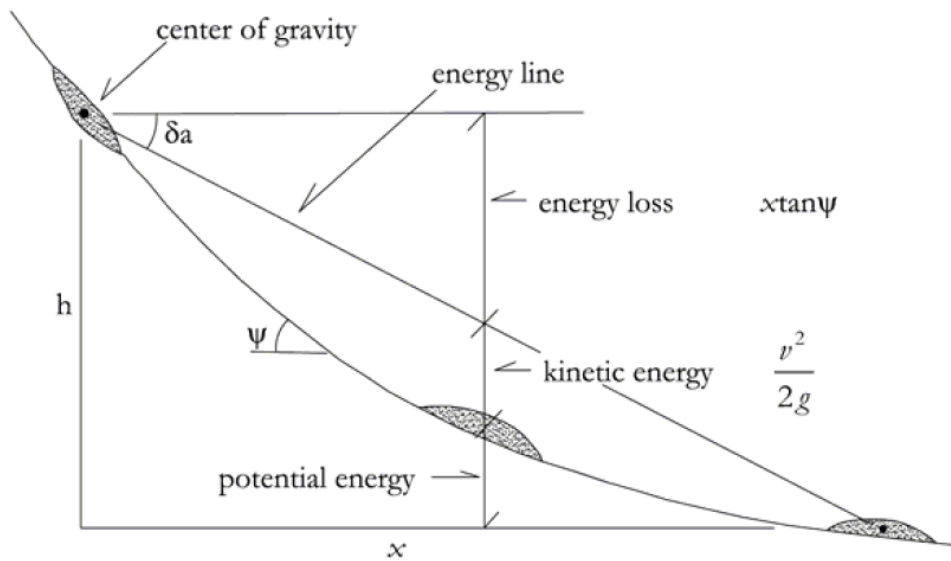


Figure 11: Energy analysis (from Sassa, 1988; adopted from Pirulli, 2005)

1.5.2. Continuum mechanics models

These models allow to determine flow paths, runout distances, flow heights, velocities. The debris flow is treated as an equivalent continuum, implying that the flow thickness extends over several grain diameters (Savage and Hutter, 1989), and two approaches can be followed to idealize the debris mass: single-phase and two-phase flow. Two-phase flow model considers separately solid and fluid constituents, while single-phase model uses global rheological properties able to simulate the behaviour of the real two-phases flow (figure 12). Majority of available software model a single-phase material: thus, only this will be considered in the following.

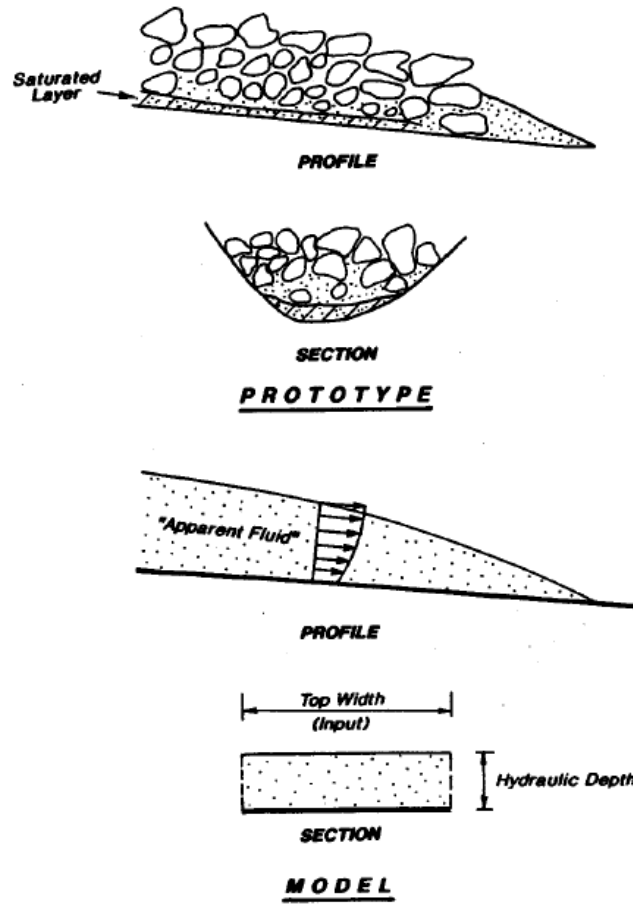


Figure 12: prototype of a two-phase debris flow and single-phase model which replaces the complex natural phenomenon (Hungri, 1995)

The fundamental equations to physically represent the flow dynamics are:

i. Mass conservation:

$$\frac{d\rho}{dt} + \nabla \cdot (\rho \mathbf{u}) = m \quad (32)$$

Where \mathbf{u} is the velocity, ρ is the mixture density and m is the rate of mass addition

ii. Momentum conservation:

$$\rho \left(\frac{\partial \mathbf{u}}{\partial t} + \mathbf{u} \cdot \nabla \mathbf{u} \right) = \nabla \cdot \boldsymbol{\sigma} + \rho \mathbf{g} \quad (33)$$

Where $\boldsymbol{\sigma}$ is the total stress tensor.

Some simplifications are usually considered (Savage and Hutter, 1989):

- Incompressible material: density is constant in space and time.
- Shallow flow: the avalanche thickness (H) is much smaller than its extent (L), which allows to depth averaging the equations. In this case, the rheology is only expressed by one term, representing the stress at the interface between the flow and the topography (Pouliquen and Forterre, 2002).
- Boundary condition: the velocity is parallel to the bed. In fact, the component of velocity normal to the bed can be neglected, since it is scaled with the depth of the flow.

To derive the depth averaged equations, it is possible to follow two approaches (Pirulli, 2005): direct integration of the equations (Savage and Hutter, 1989); balance of forces on a narrow column dx of material.

The latter will be described, following the calculations described in Pudasaini and Hutter (2007). A one-dimensional flow along a plane inclined by α is considered for simplicity (figure 13).

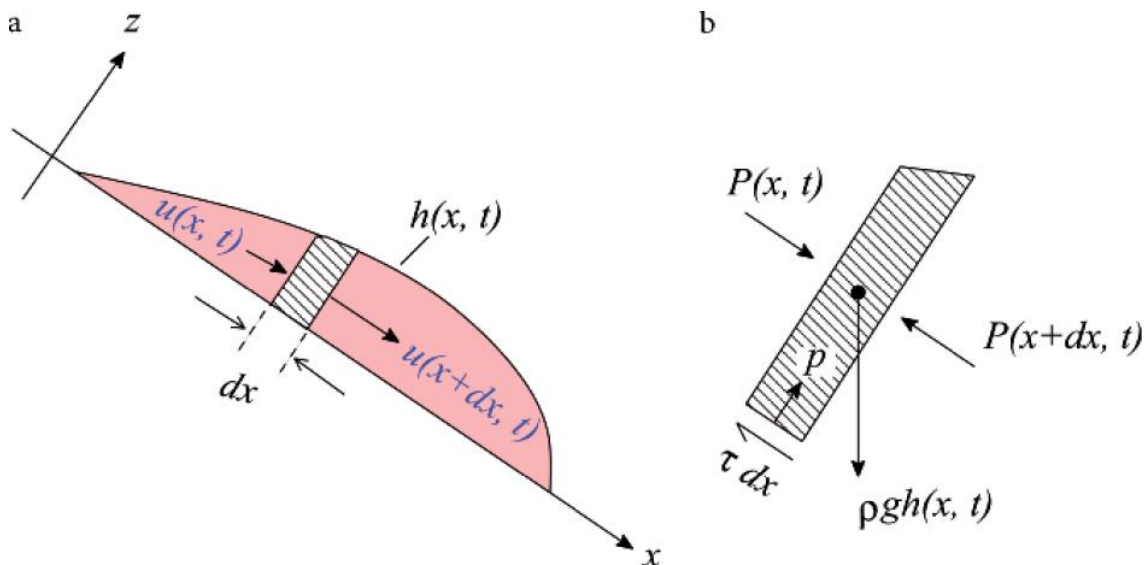


Figure 13: flow of a mass of debris along an inclined plane (a) and free body diagram of an elemental column (Pudasaini and Hutter, 2007)

The main hypotheses are (Pudasaini and Hutter, 2007):

- The flow has a constant volume. The volume may change due to deposition and entrainment.
- The material is cohesionless.
- The shear stress lateral to the flow is neglected.
- Isothermal conditions.
- Constant density.
- Constant velocity of the flow over the depth z : $u(x, t) = \frac{1}{h(x, t)} \int_0^h u(x, z, t) dz$

The mass conservation applied to the elemental column gives:

$$\begin{aligned} \frac{\partial}{\partial t}(\rho h(x, t)) &= \rho h(x, t)u(x, t) - \rho h(x + dx, t)u(x + dx, t) \\ &= -\frac{\partial}{\partial x}(\rho h(x, t)u(x, t))dx \quad (34) \end{aligned}$$

And applying the hypothesis:

$$\frac{\partial h}{\partial t} + \frac{\partial(hu)}{\partial x} = 0 \quad (35)$$

The momentum balance is obtained considering that the time rate change of momentum - $\frac{\partial}{\partial t}(\rho h(x, t)u(x, t))dx$ - is balanced by:

- The convected flux of momentum: $\rho u^2(x, t) - \left(\rho u^2(x, t) + \frac{\partial}{\partial x}(\rho u^2(x, t)h(x, t))dx\right)$;
- The body force, i.e. the component of gravity parallel to the plane: $\rho gh \sin\alpha dx$;
- The basal friction: $-\tau dx$;
- The longitudinal pressures, assumed to be related to the overburden pressure by an earth pressure coefficient ($k_{a/p}$): $\frac{1}{2}k_{a/p}\rho g \cos\alpha h^2(x, t) - \left(\frac{1}{2}k_{a/p}\rho g \cos\alpha h^2(x, t) + \frac{\partial}{\partial x}\left(\frac{1}{2}k_{a/p}\rho g \cos\alpha h^2(x, t)\right)\right)$.

The following equation is thus obtained:

$$\frac{\partial(hu)}{\partial t} + \frac{\partial(hu^2)}{\partial x} = g \sin\alpha h - \frac{\tau}{\rho} \quad (36)$$

The set of equations is completed by adding a rheological equation, which expresses the basal friction. Different models can be implemented (paragraph 1.3.2).

1.5.2.1. RAMMS::DEBRISFLOW model

The RAMMS model was first implemented for snow avalanches at the Swiss Federal Institute for Snow and Avalanche Research SLF.

It is a three-dimensional software based on depth averaged continuum equations (equations 35, 36). The equations are integrated in an Eulerian reference frame (Christen et al., 2010). Voellmy rheology is implemented. The earth pressure coefficient $k_{a/p}$ can be set equal to the active or passive conditions or equal to 1 (default setting).

2. Physical modeling and experimental setup

Tests are carried out on a debris flow model, located at the Hydraulics laboratory at NTNU in the department of Civil and Environmental Engineering (Figures 14, 15). This model allows to study the behaviour of a generic debris flow event.

The experiments performed within this thesis aim at representing 1/20 scale (λ).



Figure 14: the physical model to test debris flows

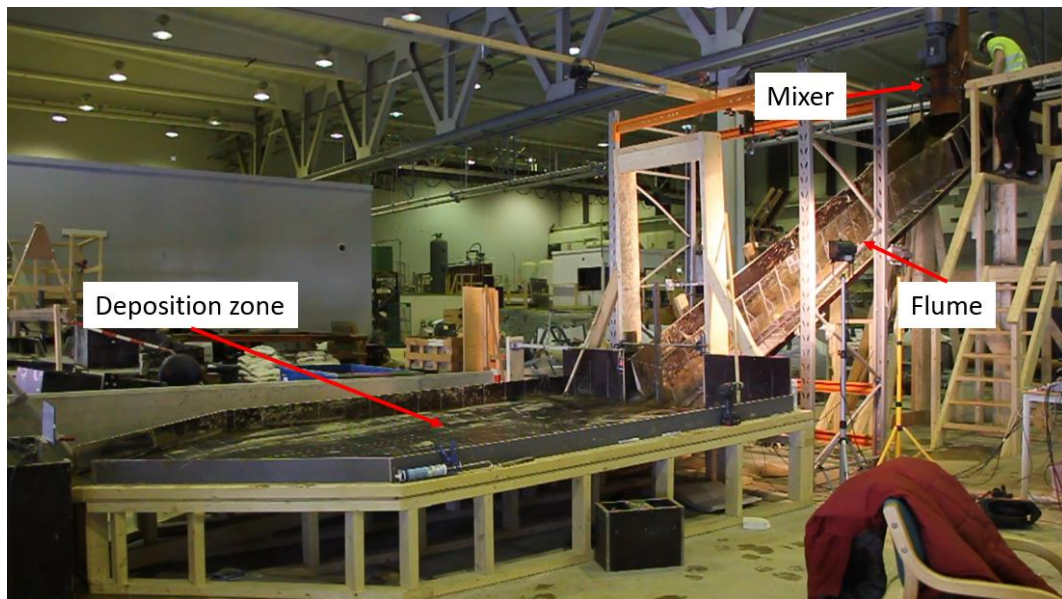


Figure 15: different parts of the model and release cylinder

A physical model of debris flows was already used at NTNU (Figure 16). As described in Laache (2016), Heller and Jensen (2009) studied the effect of deflection structures to channel debris flow under a bridge. Fiskum (2012) investigated the effectiveness of check dams, slit dams and baffles. Christiansen (2013) studied the effect of deflection structures and channels. Laache (2016) tested the effects of the drainage screen type debris flow breaker. Pradhan (2017) examined the effects of debris material (grain size distribution), volume of material and solid concentration on flow behaviour (velocity, runout and impact force).

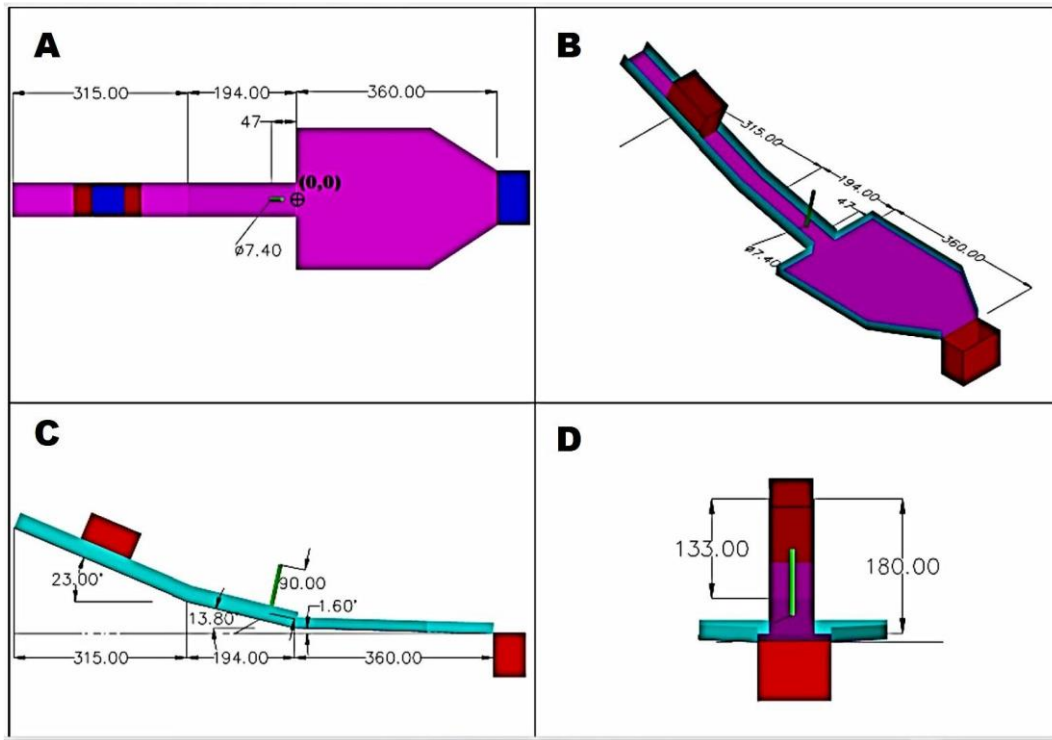


Figure 16: geometry of the physical model previously used at NTNU (from Pradhan, 2017)

A new model was constructed in 2018 which makes an improvement of the previous one about the following aspects:

- Longer flume (5 m vs. 3.25 m).
- Narrower flume channel (30 cm vs. 60 cm), which allows to create a thicker flow.
- Possibility to change the flume slope from 17.5° to 30°.
- Improved release mechanism, consisting of a mixing cylinder (Figure 17). In the old model, segregation problems happened due to the lack of mixing.



Figure 17: release cylinder. The cylinder contains a rotating device which allows to mix the debris material

2.1. Geometry

The geometry of the new model is shown in Figure 18. The equipment used to study the flow is shown in Figures 19 and 20.

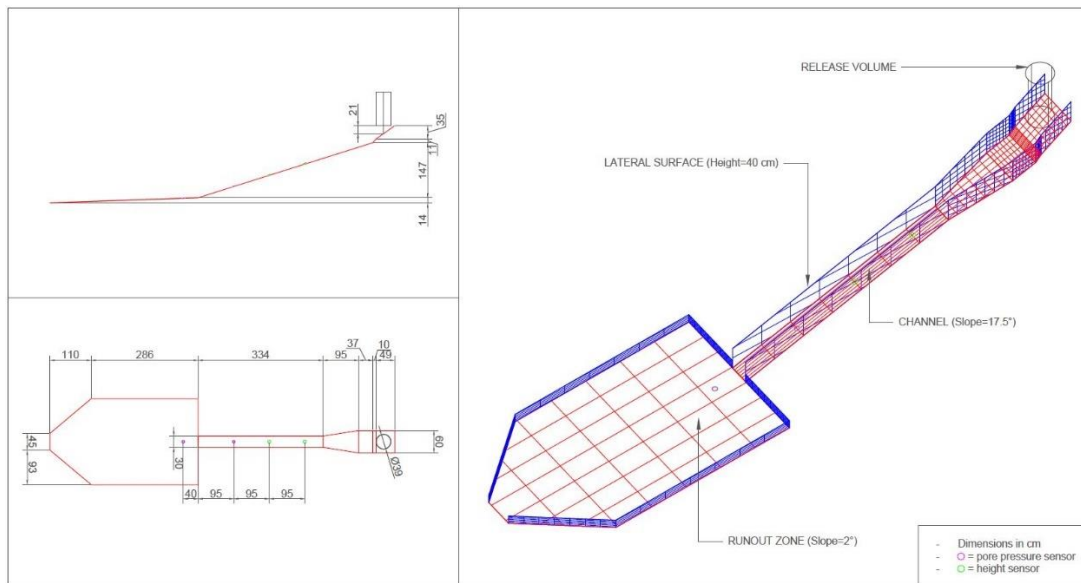


Figure 18: geometry of the model

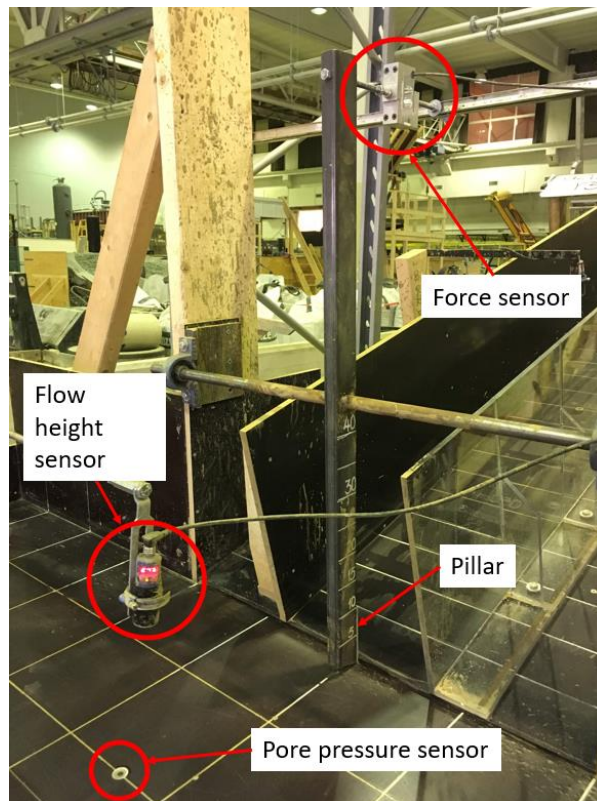


Figure 19: equipment used to study the flow

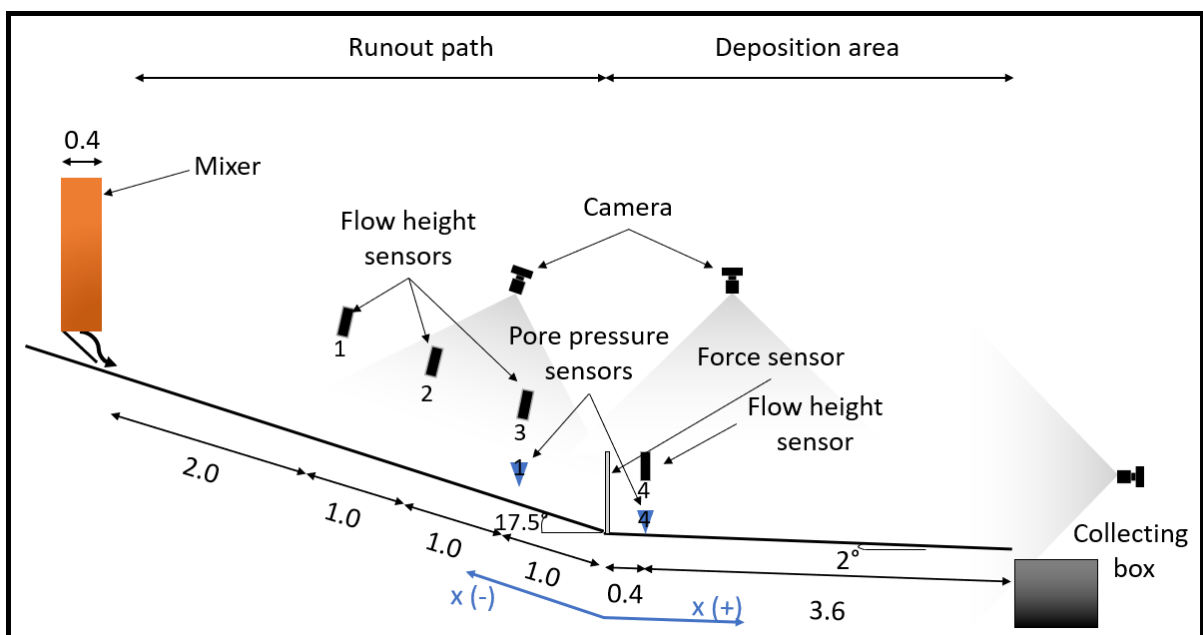


Figure 20: position of the equipment. The 'x' indicated the reference axis that will be used later to indicate the positions along the flume

The model consists of a 5 m long flume at a constant slope - 17.5° for these experiments - and a 3.86 m runout zone sloped of 2° . Along the channel, a 10 cm spaced grid is drawn, while in the runout zone the spacing is 20 cm.

Four height sensors and two pore pressure sensors are placed along the slope. Four cameras are used to track the velocity and to observe the flow behaviour. The camera located above the runout path allows to calculate the flow velocity, recording at 120 frames per second. The second camera is installed above the deposition zone to record the behaviour during the deposition. A third camera, near the collecting box, allows an overview of the model. For some tests, an high speed camera, recording at 1000 frames per second, is used to study in detail the behaviour on both the runout path, the deposition zone and the pillar.

2.2. Scaling

The experiments performed within this thesis aim at representing 1/20 scale (λ). Considering that the total runout length of the model (L_{model}), from the release area to the end where the flow stops, is approximately 8 m, from this scaling, the experiment can represent a natural debris flow with a total runout length (L_{nature}) of 160 m.

The geometric similarity implies that the ratio between the flow height and length should be constant between the model and the prototype. Therefore, equation (20) should be verified. Considering that the typical height of debris flows in nature is 1 m, the correspondent height in the model should be equal to 5 cm.

The kinematic similitude (same Froude number) implies the (22). The velocities observed in nature are usually comprised between 1 and 10 m/s: the velocities measured in the laboratory should therefore vary between 0.22 and 2.24 m/s.

The previous relationships allow to verify the consistency of scale similitude and the results obtained from the model can consequently be scaled up to understand and interpret the behaviour of natural debris flows.

2.3. Debris material

From equation (12), it derives that the debris flow material must be scaled: the ratio δ/H should be maintained constant. It follows that the ratio between the grain diameter of the model and that of a natural debris flow should be equal to:

$$\frac{\delta_{model}}{\delta_{nature}} = \lambda = \frac{1}{20}$$

Considering $\delta_{nature} = 10$ cm as a characteristic grain diameter for natural debris flows, the grain size of the material tested in the model should be of the order of magnitude of 0.5 cm.

Furthermore, the debris material must be well graded, since this is a characteristic of debris flows.

Two different materials have been tested: one with a coarser grain size distribution (material G1) and one more fine-grained soil (material G2).

The material G1 has the grain size distribution reported in Figure 21, obtained through a sieve analysis and a hydrometer test for the finer material.

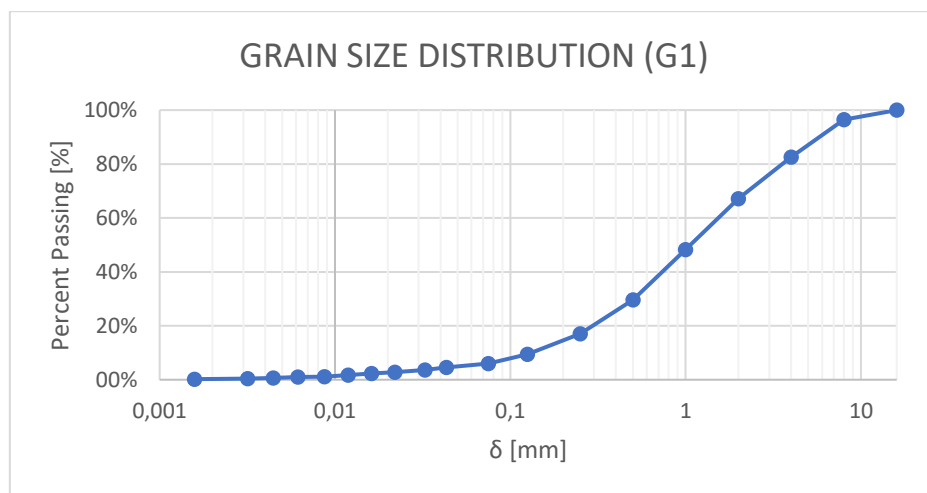


Figure 21: grain size distribution of material G1

The material G1 is characterized by a coefficient of uniformity equal to:

$$C_u = \frac{\delta_{60\%}}{\delta_{10\%}} = 12$$

The mass median diameter is equal to: $\delta_{50} = 1.09 \text{ mm}$.

It contains the following percentages of solid fractions:

- Gravel (>2 mm): 32.8%
- Sand (0.075-2 mm): 61.1%
- Lime (0.002-0.075 mm): 5.6%
- Clay (<0.002 mm): 0.5%

The fine material is here considered as the material finer than 0.03 mm: G1 contains 3.4% of fines.

The pycnometer test, performed on the solid fraction passing through the 4 mm sieve, gives a grain density of $\rho_s = 2.75 \frac{g}{cm^3}$.

The material G2 is characterized by a higher fine content. To make this material, 11.3% of a silty material was added to G1 (this percentage being equal to the mass of the fine material to be added over the total mass of G2). The natural water content of the material added to G1 is equal to 35%.

The grain size distribution is represented in Figure 22.

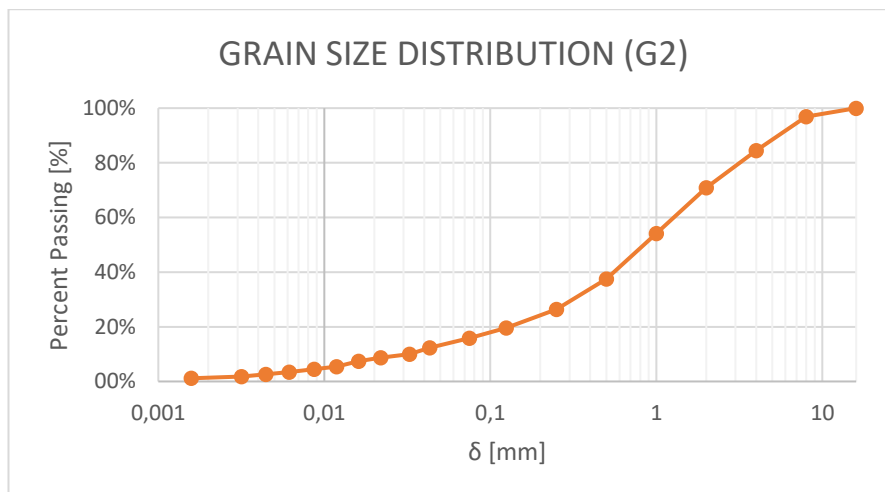


Figure 22: grain size distribution of material G2

The material G2 is characterized by a coefficient of uniformity equal to:

$$C_u = \frac{\delta_{60\%}}{\delta_{10\%}} = 42$$

It contains the following percentages of solid fractions:

- Gravel (>2 mm): 29.1%
- Sand (0.075-2 mm): 55.0%
- Lime (0.002-0.075 mm): 14.5%
- Clay (<0.002 mm): 1.3%

The mass median diameter is equal to: $\delta_{50} = 0.88 \text{ mm}$.

The fine material is considered as the material finer than 0.03 mm: G2 contains 9.7% of fines.

The pycnometer test, performed on the solid fraction passing through the 4 mm sieve, gives a grain size density of $\rho_s = 2.75 \frac{g}{cm^3}$.

The grain size distributions of G1 and G2 are compared in Figure 23.

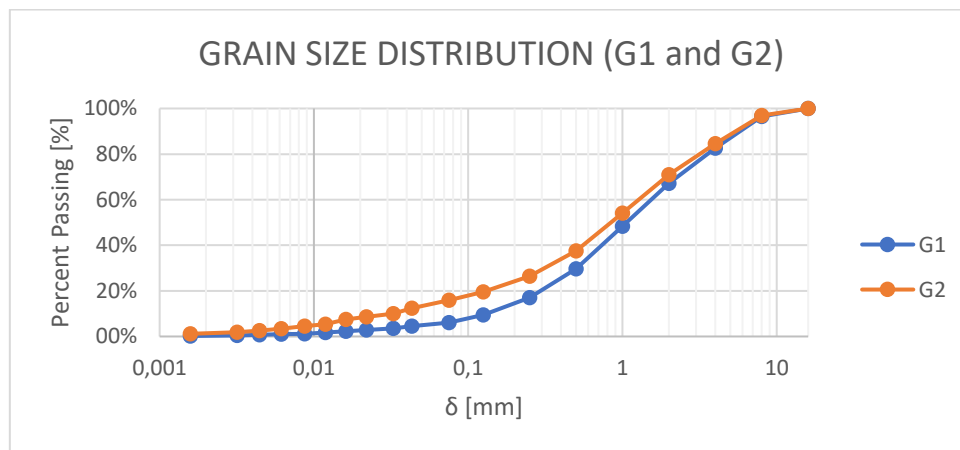


Figure 23: comparison of grain size distributions for G1 and G2

2.4. Experiment description

The aim of these tests is to understand the influence of initial and boundary conditions on the flow behaviour. The initial parameters considered in this thesis are the followings: material type (G1 and G2), release volume (25, 30, 35 L), solid concentration (60 %, 55 %, 50%). For each material type, a total of 9 combinations of volume and solid concentration parameters exist. However, to check the repeatability of each test, two more repetitions are needed, one of which to measure the force transmitted to a pillar placed at the end of the flume (named 'repetition 3', r3).

After some repetition tests, it was demonstrated that the results are reliable. Therefore, some repetitions were skipped. Furthermore, the material G1 didn't exhibit the typical flow and shape characteristics of natural debris flows: thus, more consideration was given to the material G2. The list of the tests performed in the laboratory is shown in Tables 6 and 7.

Some calibration tests have also been carried out before the debris flow tests, in order to calibrate the sensors and identify the volumes and concentrations to be used.

MATERIAL	VOLUME	CONCENTRATION	REPETITION	NAME	V [L]	C _s [%]
G1	v1	c1	r1	G1v1c1-r1	25	60%
			r2	G1v1c1-r2	25	60%
			r3	G1v1c1-r3		
		c2	r1	G1v1c2-r1		
			r2	G1v1c2-r2		
			r3	G1v1c2-r3		
		c3	r1	G1v1c3-r1	25	50%
			r2	G1v1c3-r2		
			r3	G1v1c3-r3		
	v2	c1	r1	G1v2c1-r1		
			r2	G1v2c1-r2		
			r3	G1v2c1-r3		
		c2	r1	G1v2c2-r1	30	55%
			r2	G1v2c2-r2	30	55%
			r3	G1v2c2-r3		
		c3	r1	G1v2c3-r1		
			r2	G1v2c3-r2		
			r3	G1v2c3-r3		
	v3	c1	r1	G1v3c1-r1		
			r2	G1v3c1-r2		
			r3	G1v3c1-r3		
		c2	r1	G1v3c2-r1		
			r2	G1v3c2-r2		
			r3	G1v3c2-r3		
		c3	r1	G1v3c3-r1	35	50%
			r2	G1v3c3-r2		
			r3	G1v3c3-r3		

Table 6: list of tests (G1)

MATERIAL	VOLUME	CONCENTRATION	REPETITION	NAME	V [L]	C _s [%]
G2	v1	c1	r1	G2v1c1-r1	25	60%
			r2	G2v1c1-r2	25	60%
			r3	G2v1c1-r3	25	60%
		c2	r1	G2v1c2-r1	25	55%
			r2	G2v1c2-r2	25	55%
			r3	G2v1c2-r3	25	55%
		c3	r1	G2v1c3-r1	25	50%
			r2	G2v1c3-r2		
			r3	G2v1c3-r3	25	50%
	v2	c1	r1	G2v2c1-r1	30	60%
			r2	G2v2c1-r2	30	60%
			r3	G2v2c1-r3	30	60%
		c2	r1	G2v2c2-r1	30	55%
			r2	G2v2c2-r2	30	55%
			r3	G2v2c2-r3	30	55%
		c3	r1	G2v2c3-r1	30	50%
			r2	G2v2c3-r2		
			r3	G2v2c3-r3	30	50%
	v3	c1	r1	G2v3c1-r1	35	60%
			r2	G2v3c1-r2		
			r3	G2v3c1-r3	35	60%
		c2	r1	G2v3c2-r1	35	55%
			r2	G2v3c2-r2		
			r3	G2v3c2-r3	35	55%
		c3	r1	G2v3c3-r1	35	50%
			r2	G2v3c3-r2		
			r3	G2v3c3-r3	35	50%

Table 7: list of tests (G2)

By varying these initial parameters, it is possible to study their influence on the flow behaviour. In particular, the following flow characteristics are considered: runout distance, velocity, flow height, deposition height, impact force.

2.4.1. Equipment and data processing

Runout distance is measured in the deposition area, taking the end of the flume as the origin of the reference axes and measuring until the point where the debris material stops (Figure 24). In some tests, the water was flowing longer than the debris material

(intended as a mixture of fluid and sediments): this is not taken into account in the runout distance measurement.

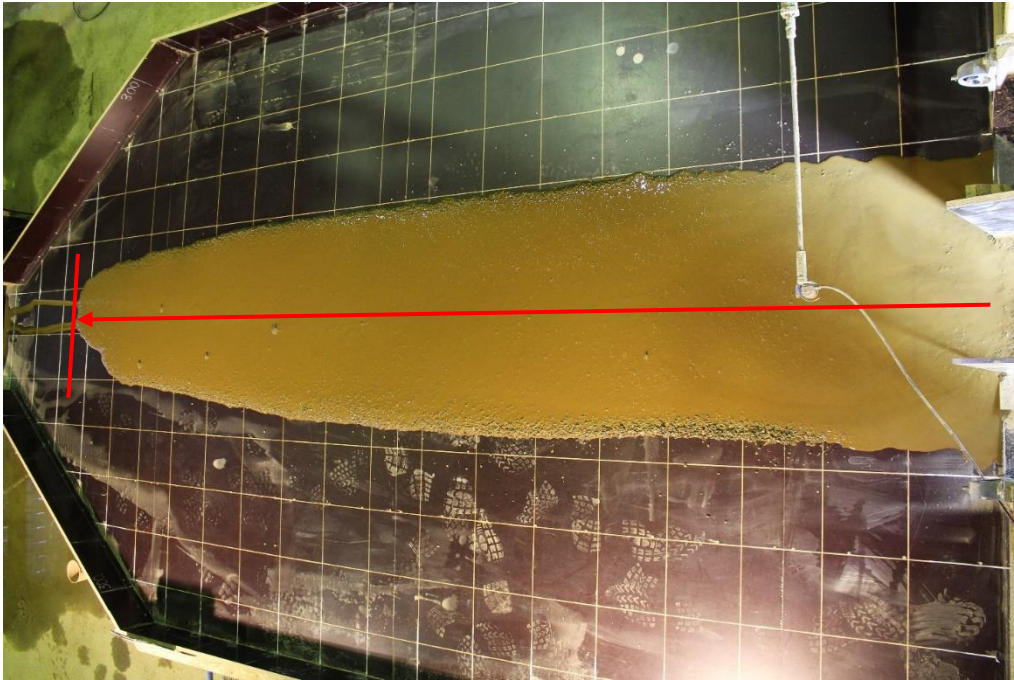


Figure 24: runout distance measurement

Velocity is obtained by taking the video of the flume and the deposition area, using cameras oriented orthogonal to the slope. For some selected tests, the complete velocity profile is plotted; however, in the other cases, velocity is only calculated at some selected locations (-2 m, -1 m, -0.2 m), using the video recorded by the camera on upstream.

To calculate the velocity, the flow front position is tracked using the software 'Tracker' (Figure 25). The following procedure is adopted:

- Creation of a coordinate axes;
- Selection of a homogeneous zone (constant ground sampling distance) and creation of a calibration stick, which converts the pixels to a metric value;
- Tracking the flow front (the more advanced part of the flow) at each frame;

- Plotting the velocity. To get the value at the selected locations (e.g. -1 m), velocity was calculated in around ± 10 cm (e.g. -1.1 m - -0.9 m); a linear trendline was plotted and the value at the selected location was taken.

The quality of the velocity tracking depends on the lighting conditions. At each frame, the flow front moves approximately 3 cm. Taking 1 cm as an order of magnitude of the error during the picking process (due to the difficulty to identify the flow front), and considering the camera recording frequency of 120 fps, the order of magnitude of the error in calculating the velocity is 1 m/s. However, this error reduces by taking the trendline in the arounds of the point of interest.

Only the velocity of the flow front has been tracked: this doesn't necessarily follow the centre of the flow line. Furthermore, the shape of the flow front changes during the flow and it is therefore difficult to follow it.

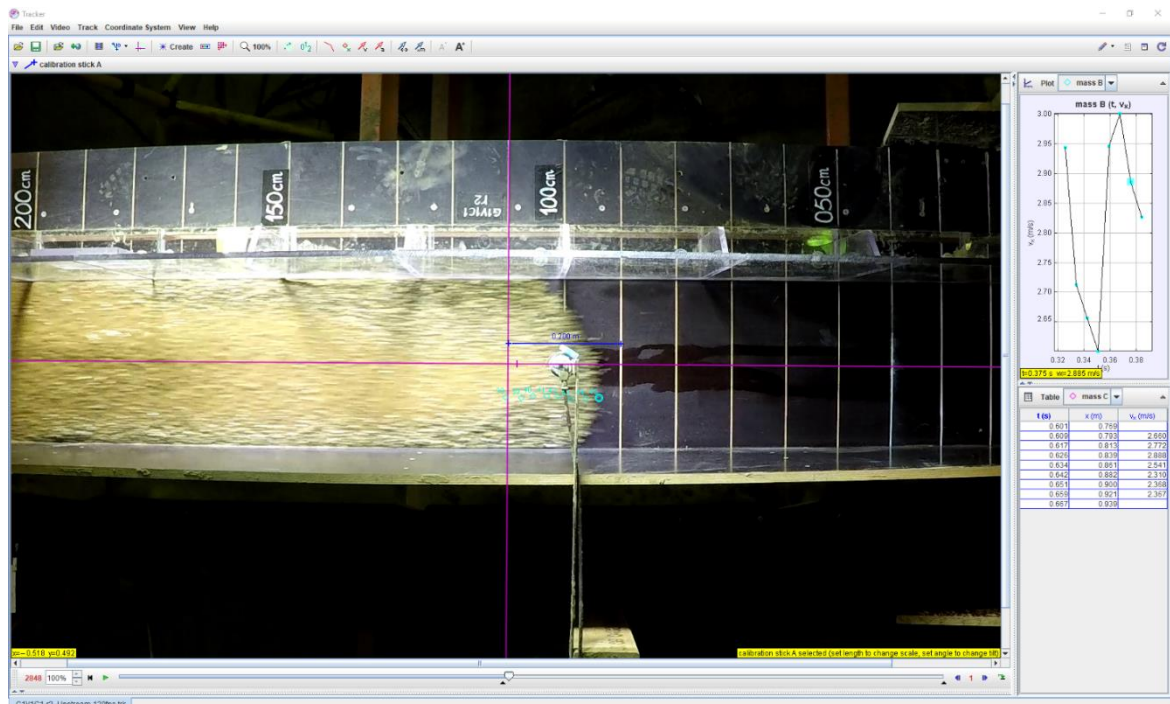


Figure 25: software 'Tracker' to track the flow front velocity

Four ultrasonic sensors were recording the flow height at -3 m, -2 m, -1 m and 0.4 m.

The impact force was measured by placing a rectangular pillar with a sensor, at the end of the flume (Figure 26).

Finally, two pore pressure sensors were used to calculate the pore fluid pressure.

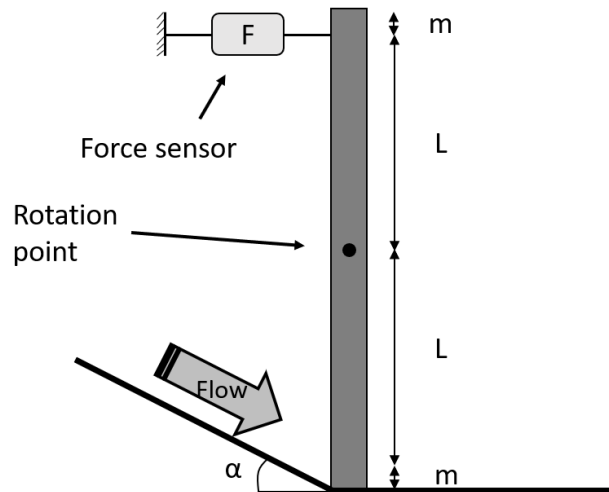


Figure 26: pillar measuring the force transmitted by the flow

2.4.2. Test procedure

The procedure to carry out the experiment is the following:

- Clean the model runout surface.
- Indicate the test number on a white board.
- Put the debris components in the cylinder.
- Lift the cylinder in correspondence of the release point; the mixer is started and kept running for approximately 10 minutes.
- Start the recording of the cameras.
- Start the pore pressure and height flow sensors. At the same moment, the release cylinder is opened.
- Take pictures of the runout zone and eventually collect some samples for grain size distribution analysis.
- Clean the release cylinder.
- Results are saved.

The debris mixture is made up of the following components:

- The total volume (V_{tot}) and the solid concentrations (C_s) are chosen based on the test to be performed.
- The solid volume is calculated as: $V_s = C_s \cdot V_{tot}$.
- The total water volume is: $V_w = V_{tot} - V_s$.
- The total mass of dry solids is: $M_{s,tot} = \rho_s \cdot V_s$. where ρ_s is the grain density, which has been estimated to be equal to 2.75 g/cm^3 . For the material G1, the solid mass is only made up of a dry soil.
- For G1, the mass of water to be added to the dry soil is equal to: $M_{w,tot} = V_w \cdot \rho_w$. Where ρ_w is the density of water (1 g/cm^3).
- In the case of G2, the soil mass is made of two components: the dry material G1 and a silty material which is added to the mixture. The quantity of fine material to be added to G1 is equal to: $M_{fine,dry} = \%f \cdot M_s$, where $\%f$ is the percentage of fine material to be added (11.3%). Therefore, the mass of the solid material G1 is equal to: $M_{G1} = M_{s,tot} - M_{fine,dry}$.
- Since the fine material is wet, the total mass of fine material to be added is: $M_{fine,tot} = M_{fine,dry} \cdot (1 + w)$. Where w is the natural water content of the fine material (measured equal to 35%).
- The extra water to be added is therefore equal to: $M_{w,added} = M_{w,tot} - (M_{fine,tot} - M_{fine,dry})$.

Summarizing, the debris mixture G1 is prepared weighting the following materials: $M_{w,tot}$ of water; $M_{s,tot}$ of dry material G1. The debris mixture G2 is made of: $M_{w,added}$ of added water; M_{G1} of dry material G1; $M_{fine,tot}$ of fine silty material. The results are summarized in tables 8 and 9.

The density of the debris material can be calculated as:

$$\rho = \frac{M_{s,tot} + M_{w,tot}}{V_{tot}} \quad (37)$$

In tables 8 and 9 the composition of the mixture is summarized.

G1

TEST	V_{tot} [L]	C_s [%]	$M_{s,\text{tot}}$ [kg]	$M_{w,\text{tot}}$ [kg]	ρ [kg/m ³]
G1V1C1	25	60	41.3	10.0	2050.0
G1V1C2	25	55	37.8	11.3	1962.5
G1V1C3	25	50	34.4	12.5	1875.0
G1V2C1	30	60	49.5	12.0	2050.0
G1V2C2	30	55	45.4	13.5	1962.5
G1V2C3	30	50	41.3	15.0	1875.0
G1V3C1	35	60	57.8	14.0	2050.0
G1V3C2	35	55	52.9	15.8	1962.5
G1V3C3	35	50	48.1	17.5	1875.0

Table 8: quantities of material to create the debris flow mixture (G1)

G2

TEST	V_{tot} [L]	C_s [%]	M_{G1} [kg]	$M_{\text{fine,tot}}$ [kg]	$M_{w,\text{added}}$ [kg]	ρ [kg/m ³]
G2V1C1	25	60	36.7	6.6	8.4	2050.0
G2V1C2	25	55	33.7	6.1	9.8	1962.5
G2V1C3	25	50	30.6	5.5	11.2	1875.0
G2V2C1	30	60	44.1	6.6	10.1	2050.0
G2V2C2	30	55	40.4	6.1	11.8	1962.5
G2V2C3	30	50	36.7	5.5	13.4	1875.0
G2V3C1	35	60	51.4	6.6	11.8	2050.0
G2V3C2	35	55	47.1	6.1	13.7	1962.5
G2V3C3	35	50	42.8	5.5	15.6	1875.0

Table 9: quantities of material to create the debris flow mixture (G2)

3. Results and analysis

The results of the laboratory tests are presented here. In particular, the behaviour of one reference tests is fully analysed, examining the morphology of the flow, the velocity profile, the flow height, the pore pressure generation, the depositional process and the pressure transmitted to the pillar. The flow characteristics (flow front velocity, flow height, runout distance) are then compared to the initial and boundary conditions (material type, solid concentration, release volume), in order to determine how the latter influence the flow.

The analysis concerns the material G2, since the data are complete, reliable and this material better represent real debris flows from a morphological and behavioural point of view. Test results are reported in Appendix 1 for G2 and in Appendix 2 for G1.

Finally, dimensionless parameters are calculated to be compared to other small-scale experiments and to natural debris flows.

3.1. Reference experiment

The experiment G2V1C1R1 is fully analysed. It exhibits the typical features of natural debris flows.

The flow behaviour along the flume is characterized by a dry flow front, followed by a more wet body. At -1.7 m (Figure 27), this distinction is evident; however, as the debris flows downslope, e.g. at -0.7 m (Figure 28), the wet body tends to reach the dry flow front.

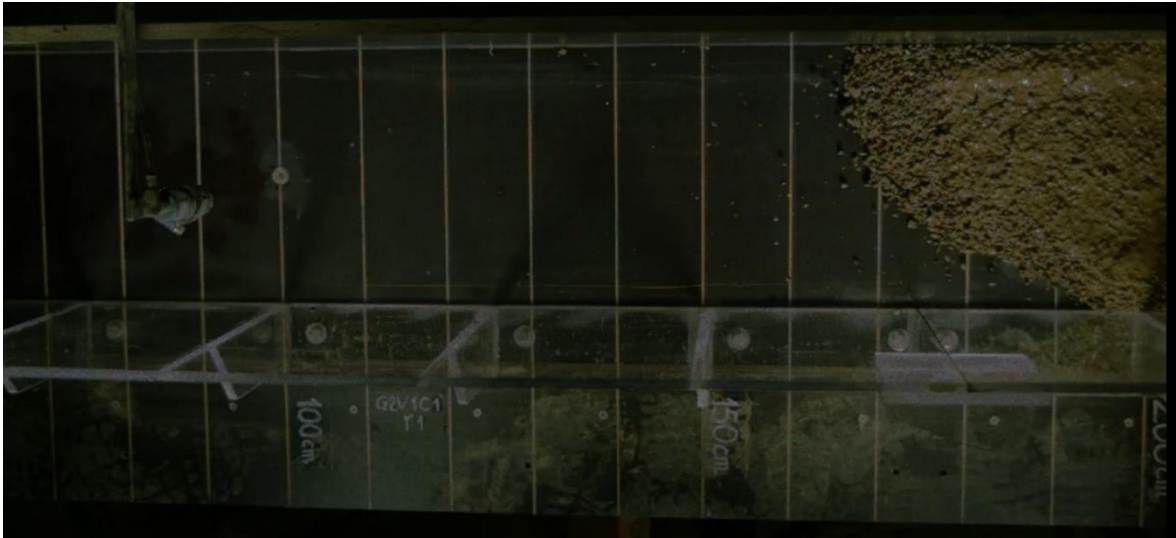


Figure 27: flow at -1.7 m for test G2VIC1R1

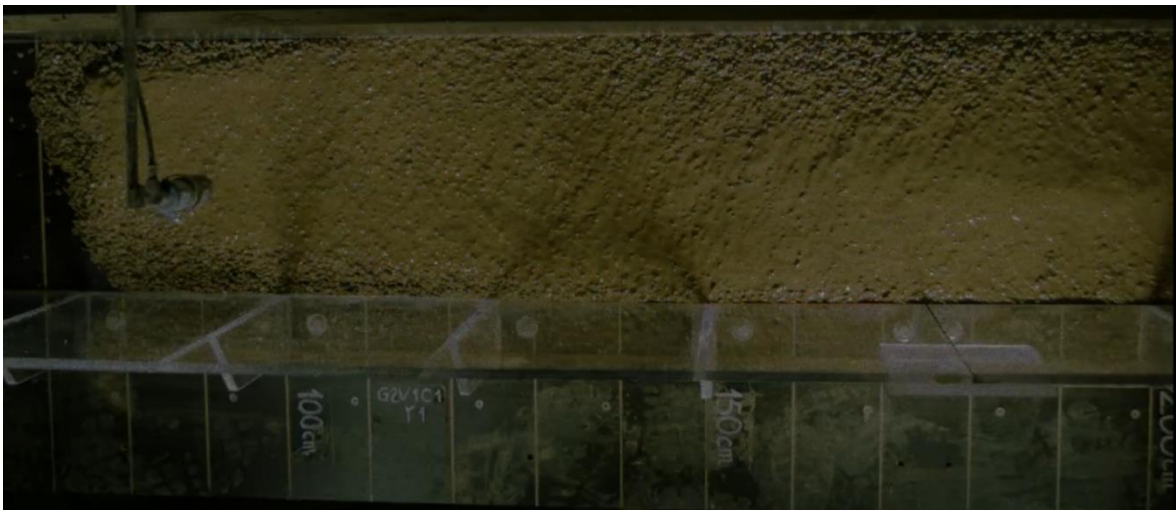


Figure 28: flow at -0.7 m for test G2VIC1R1

This behaviour affects the velocity trend. In fact, at -1.7 m, the flow is slower; when the wet body comes, the flow accelerates again (Figure 29). This observation can probably be explained by the fact that a more wet debris material is able to keep excess pore pressures, which decrease the shear stress resisting the flow.

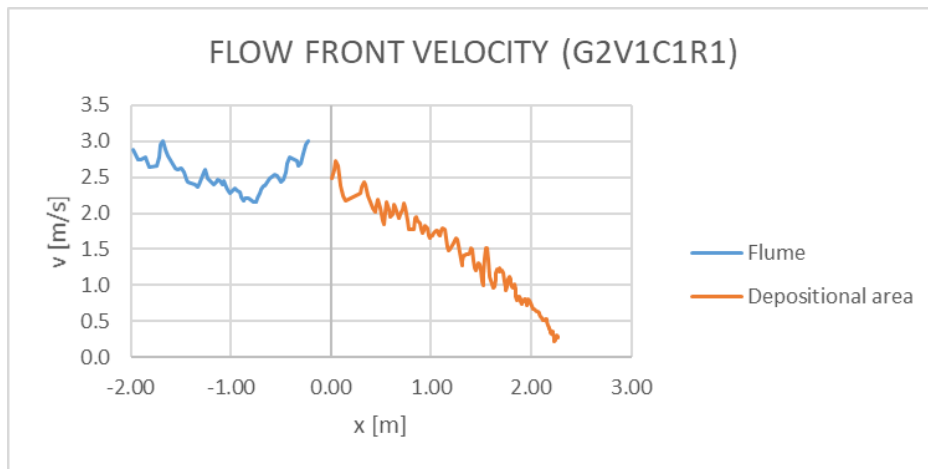


Figure 29: velocity profile for test G2V1C1R1

It should also be noticed the non-symmetry of the flow – which may affect the flow height measurements. This can be explained by the flow mass hitting the walls.

About the flow height, it decreases moving downslope (Figure 30). This is related to the tendency of debris flows to elongate, which has been explained theoretically by Iverson (Jakob et al., 2005) and is due to the steepness of the flow front.

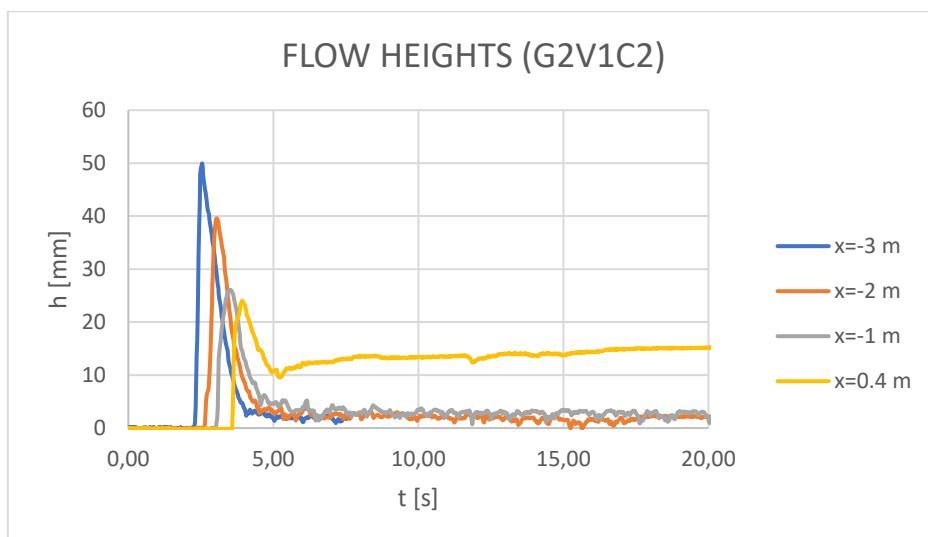


Figure 30: flow height in function of time, at different locations along the flume (-3 m, -2 m, -1 m) and at the beginning of the deposition zone (0.4 m), for test G2V1C1R1

The pore pressure has been measured at -1 m (Figure 31). When compared to the flow height, it greatly exceeds the hydrostatic pressure (by a factor of almost 4). It is believed that, even if excess pore pressures are a common characteristics of debris flows, the magnitude of the pore pressure is too high, which may have been affected by air bubbles trapped in the pore pressure sensor. However, its shape is in accordance with the one of the flow height: therefore, the pore pressure measurement may also have been affected by grain collisions on the sensor.

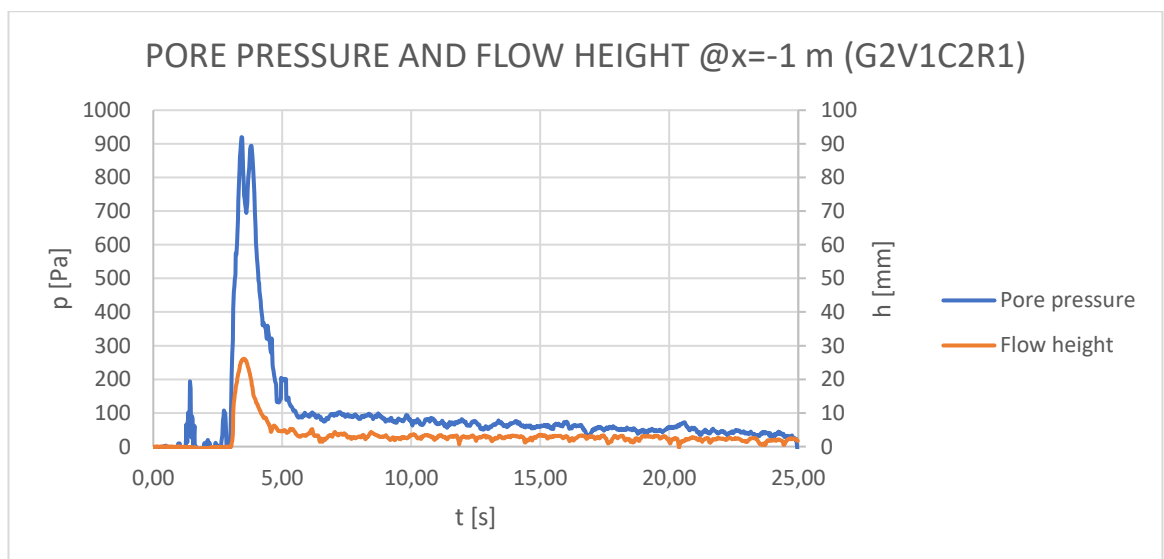


Figure 31: pore pressure in function of time at -1 m for test G2VIC1R1, compared to flow height

When the debris material reaches the depositional zone, it decelerates and stops at 2.32 m (Figures 32 and 33). The deceleration is due to both the slope angle reduction to 2° and to the lateral expansion of the flow. Some peculiar debris flow characteristics are exhibited: levee formation (Figure 34), coarser front and consequent longitudinal grain sorting. For this high sediment concentration, levees particularly influence the flow behaviour as they avoid the material to expand laterally; this gives to the deposit an elongated shape (Figures 32 and 33).

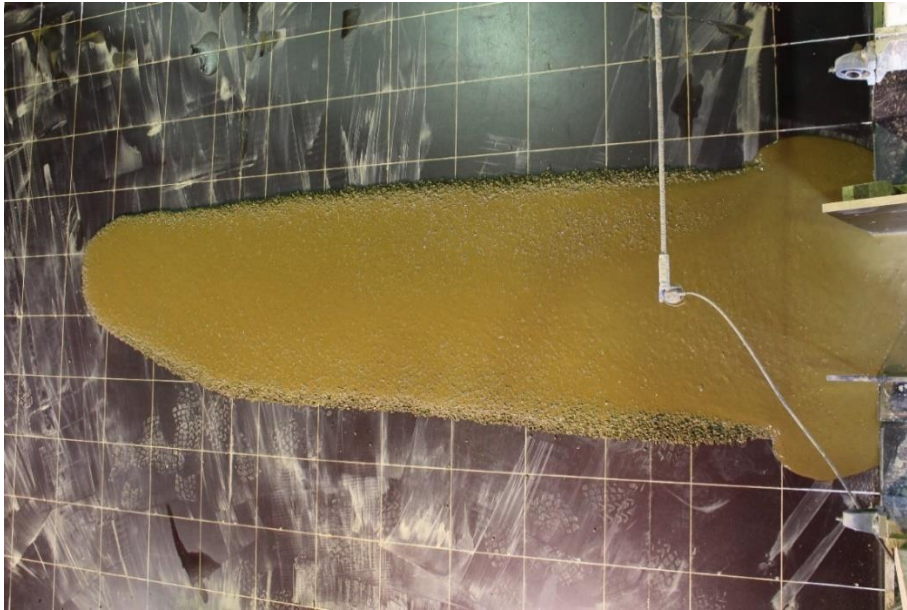


Figure 32: elongated deposit shape for test G2V1C1R1



Figure 33: elongated deposit shape for test G2V1C1R1, with the front in detail



Figure 34: coarse levees

The plot of the flow height (figure 30) at the beginning of the deposition area (0.4 m) shows the flow of the debris front, followed by an increase in the flow height, i.e. the formation of the deposit.

The deposit thickness has been measured at different locations and is almost constant (1.5 cm).

The force has been measured by a pillar placed at the end of the channel. The plot of the force measurement for the test G2V1C1R3 is reported in Figure 35.

An initial build-up of the force is recorded, which may be due to the vibration caused by the opening of the release cylinder. This is followed by the arrival of the flow front, which causes the force to rise to a value of 13.8 N. Then, the force transmitted to the pillar gradually decreases to a stationary value of approximately 3 N.

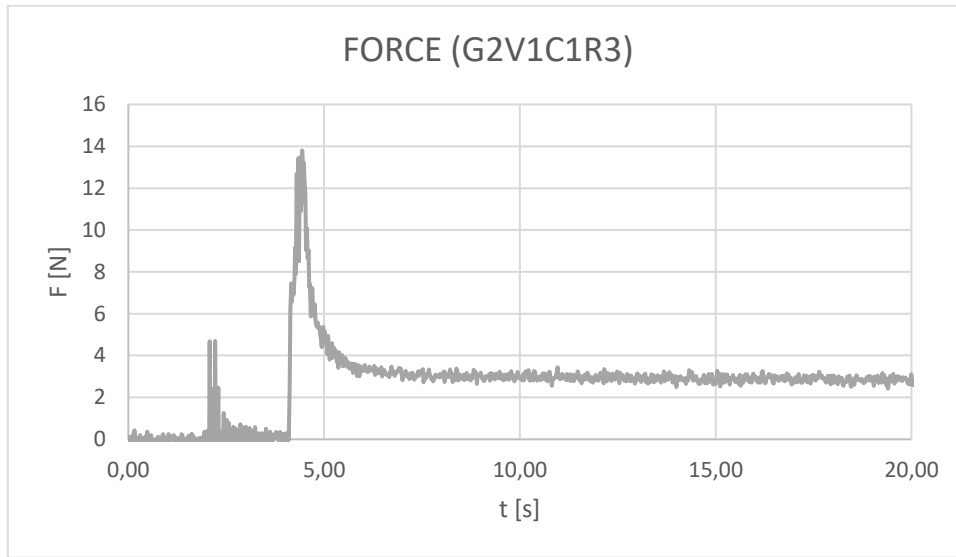


Figure 35: force measurement for G2V1C1R3

The maximum impact pressure can be calculated considering the width of the pillar (2.5 cm) and the maximum flow height of the flow, as follows:

$$p_{max} = \frac{F_{max}}{0.025 \cdot h_{max}} \quad (38)$$

For test G2V1C1R3, a maximum pressure of 20.6 kPa is obtained.

The hydrostatic pressure can be calculated as:

$$p_{hydro} = \rho g h_{max} \quad (39)$$

Which corresponds to 0.5 kPa for this test. The measured pressure is therefore considerably higher than the hydrostatic one.

3.2. Material G1

In this paragraph, the material G1 is briefly analysed, as only few tests were conducted with it and the material G2 was considered more representative of natural debris flows. Test results are reported in Appendix 2. The direct comparison with material G2 was tricky and it shows opposite, and sometimes difficult to explain, trends. Therefore, only some key features of tests with G1 are considered.

Figure 36 shows the deposit shape of the test G1V1C1R2. Compared to the test G2V1C1R1, the levees are not well developed, and this is confirmed by the fact that water can easily escape from the deposit. A lower fine content is not able to keep the two constituents (fluid and solids) together.

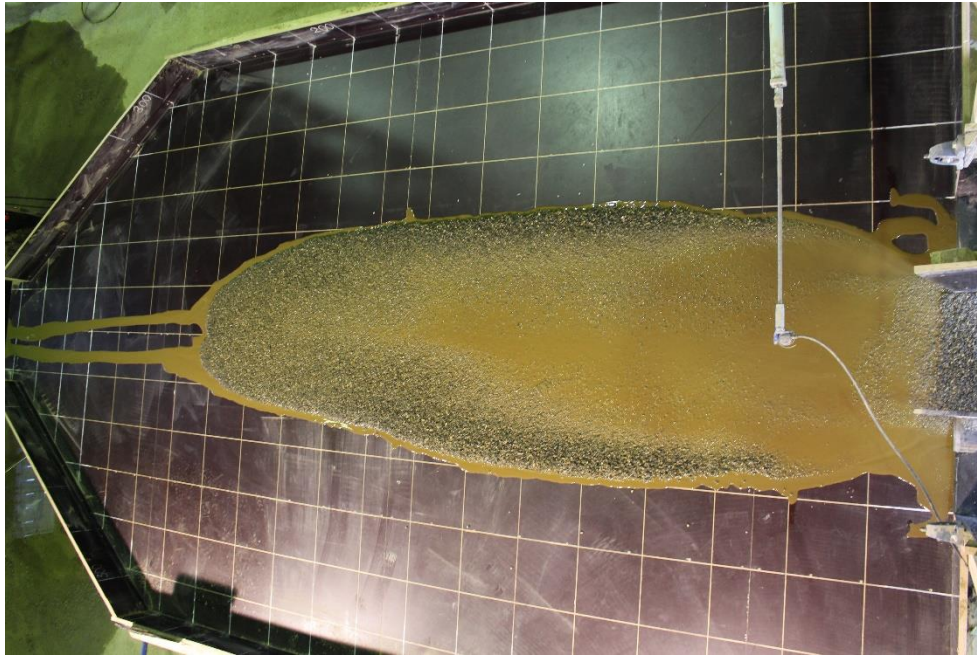


Figure 36: deposit shape of G1V1C1R2 test

3.3. Runout distance

In this and in the following chapters, only material G2 is considered.

Runout distance has been measured for repetitions 1 and 2. The third repetition of each combination of volume and sediment concentrations is not used to determine the travel distance, since this result is affected by the presence of the rectangular pillar.

The complete series of data is reported in Appendix 1 and the pictures of the deposition zone are shown in Appendix 3. Some tests produced a runout that slightly exceeded the runout table. In this case, an estimated value has been considered, to be able to draw a trend.

For each combination of release volume and sediment concentration, the average value is calculated (Figure 37). The repeatability of the runout distance is high. The results are plotted in function of the sediment concentration, since it is expected that this variable will mainly affect the runout distance; the influence of the release volume is lower. A linear regression is able to well represent this trend.

As the sediment concentration increases, the runout distance decreases. The material becomes in fact more homogeneous, thicker and friction will increase. This kind of material is also able to develop levees and a coarse dry snout, which also increases the friction (Figures 32 and 33). A drier material will limit the raise of excess pore pressures, which are responsible of the decrease of the frictional stress. On the contrary, a higher water content keeps the material dilated, which is therefore able to develop granular temperature and exhibit a more turbulent flow, enhancing the mobility. Levees and coarse snout are not fully developed and the dam stopping effect is therefore not established (Figure 38). Finally, the solid concentration also affects the viscosity and the yield strength: a lower concentration will decrease the yield stress and the viscosity (refer to paragraph 1.3.2.1.) and, thus, the runout increases.

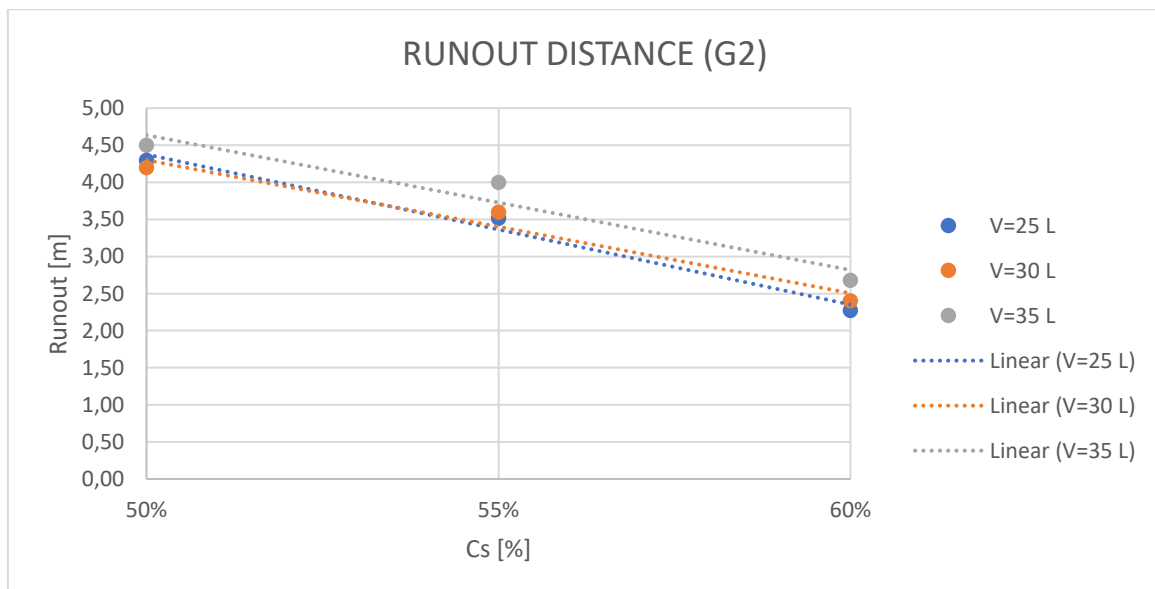


Figure 37: averaged values of runout distance in function of solid concentration and volume

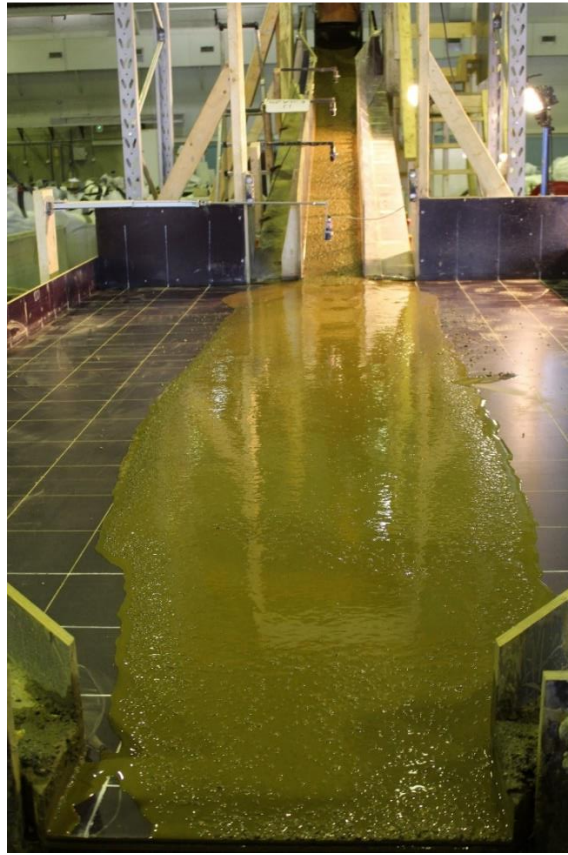


Figure 38: deposit shape for test G2VIC3R1, with the front in detail

3.4. Deposit shape

The solid concentration will affect the deposit shape (Appendix 3). A low solid concentration will not allow the formation of levees, which are able to block the lateral expansion of the debris flow: the deposit width is higher in this case (Figure 38, for 50% solid concentration and Figure 33, for 60% solid concentration). A low concentration is also associated to a higher velocity and agitation of the moving mass: this also contributes to the lateral expansion and longer runout of more wet debris flows.

3.5. Flow velocity

Flow velocity has been calculated at -2 m, -1 m, -0.2 m for each test (Appendix 1). The average values at each location are shown in Figures 39, 40, 41. The standard deviation of the three repetitions of each tests is not negligible (in the order of magnitude of 0.25 m/s): as discussed previously, this might be affected by the flow front picking process, by the lighting conditions which make difficult to precisely identify the flow front, but also by the intrinsic variability of this parameter.

As for runout distance, velocity decreases with increasing solid concentration, the reasons being the same. The trends with release volume are not clear, which may be due to the lower precision of velocity measurement.

From a morphological point of view, the flows at different concentrations look different. A lower concentration is characterized by front particles separated from the flow, moving faster (Figure 42): this can be explained by the higher velocity of these flows, which increases the agitation. After the passage of these isolated particles, the debris flow comes and is characterized by a more homogeneous material – i.e. absence of a drier and coarser flow front – compared to the higher solid concentrations flows (Figure 43). Finally, a lower concentration is visibly more turbulent and characterized by ‘splashes’ due to the impact of the material on the lateral walls.

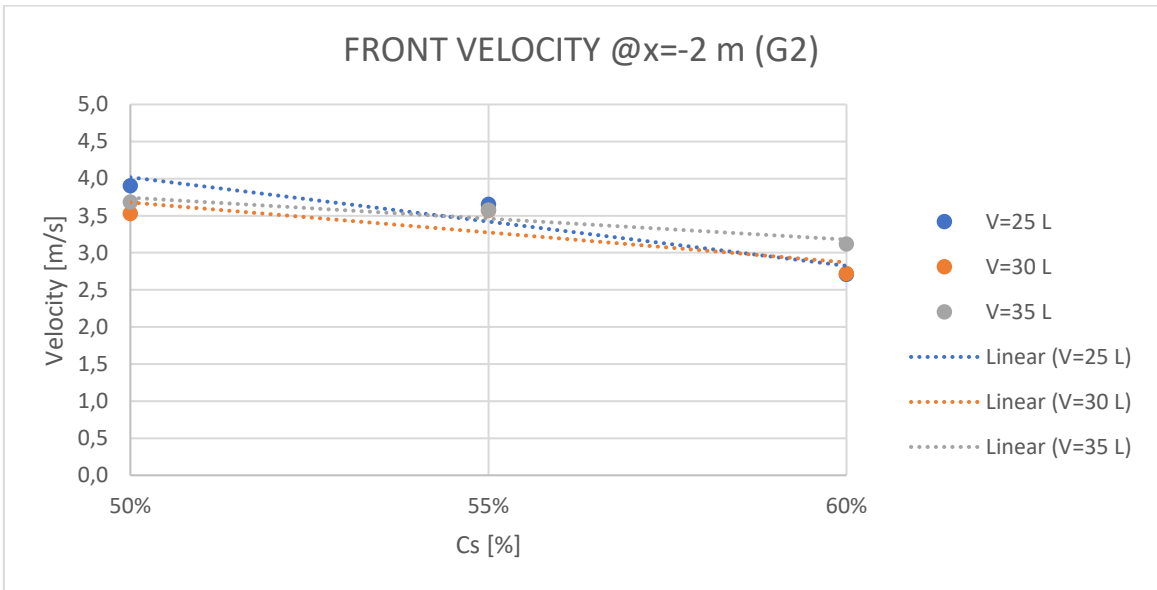


Figure 39: averaged flow front velocity at -2 m in function of solid concentration and volume

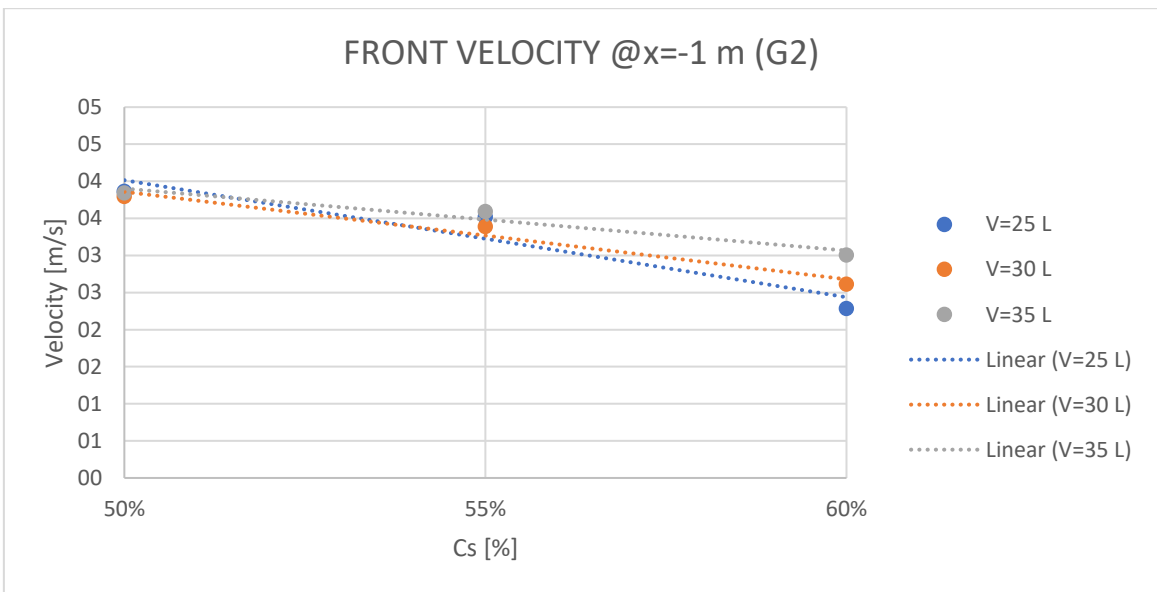


Figure 40: averaged flow front velocity at -1 m in function of solid concentration and volume

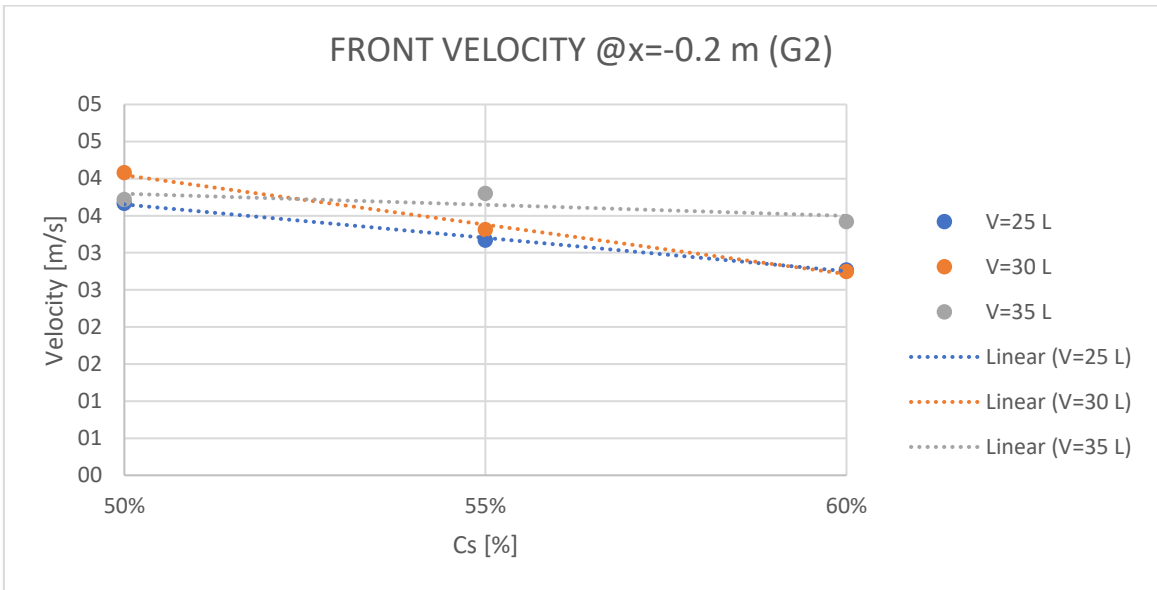


Figure 41: averaged flow front velocity at -0.2 m in function of solid concentration and volume



Figure 42: behaviour in the flume for test G2V2C3R1 (lowest concentration)



Figure 43: behaviour in the flume for test G2V2C1R1 (highest concentration)

The expected values of velocity, considering the Froude scaling presented in chapter 1.4.1., are between 0.22 and 2.24 m/s. The values obtained in these experiments are between 3 and 4 m/s and are therefore too high to show Froude similarity with natural debris flows. However, how it will be discussed later, this is a result of the mechanisms of stress generation that set in small scale debris flows; this kind of flow will be more representative of a thin and fast mass movement.

3.6. Flow height

The maximum values of the flow height have been picked at -3 m, -2 m, -1 m, 0.4 m. In this case, the dependency on the volume is believed to be more important (averaged values in Figures 44, 45, 46, 47): in all the cases, the flow height increases as the volume increases, which is due to the greater quantity of material flowing at the same time. However, when the material flows downslope, this dependency becomes less important, as the debris flow tends to elongate (Jakob et al., 2005).

The influence of the solid concentration is also important, in particular in upstream. However, it is difficult to give a physical motivation to this observation, also because of the different trends observed at different locations.

Finally, it should be observed that the standard deviation of the flow height may be quite high (in the order of magnitude of 0.5 cm) and in particular in upstream, due to the presence of splashes.

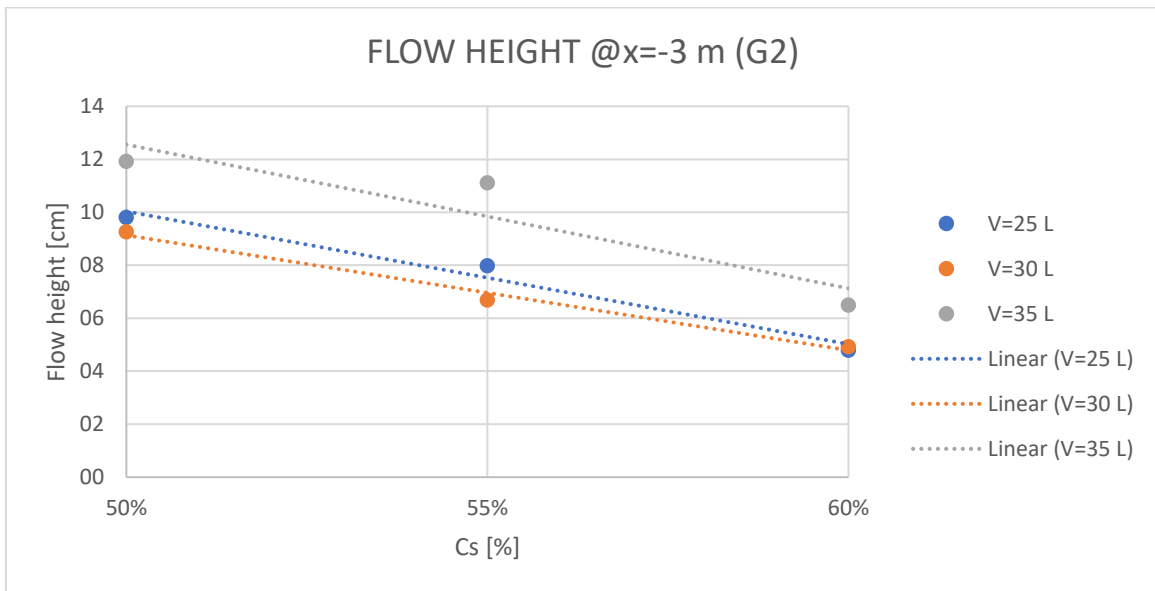


Figure 44: averaged maximum flow height at -3 m in function of solid concentration and volume

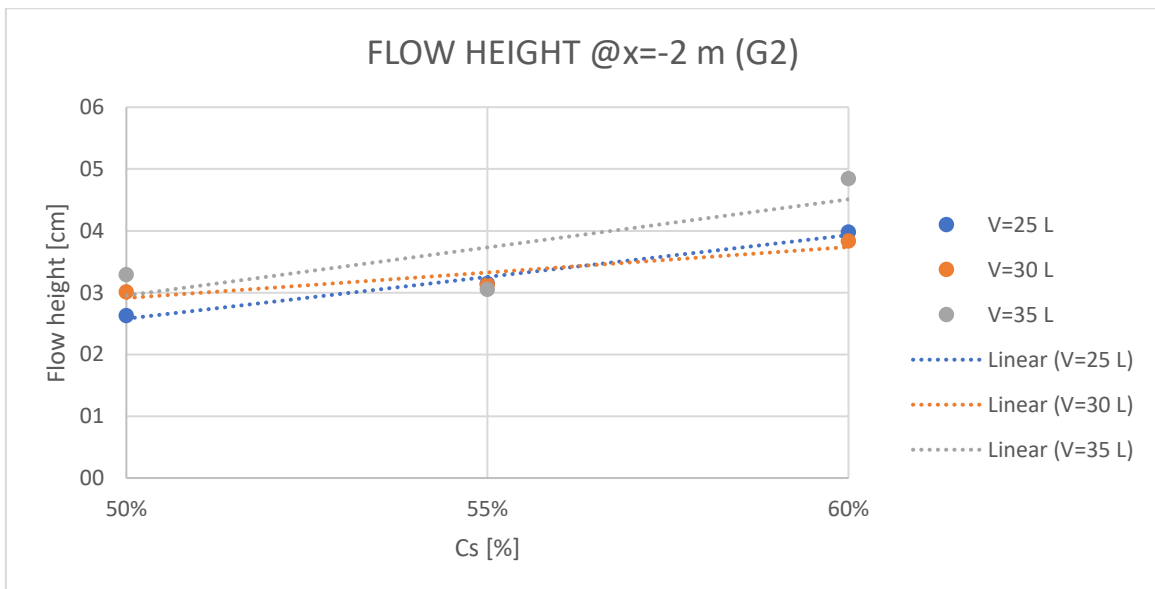


Figure 45: averaged maximum flow height at -2 m in function of solid concentration and volume

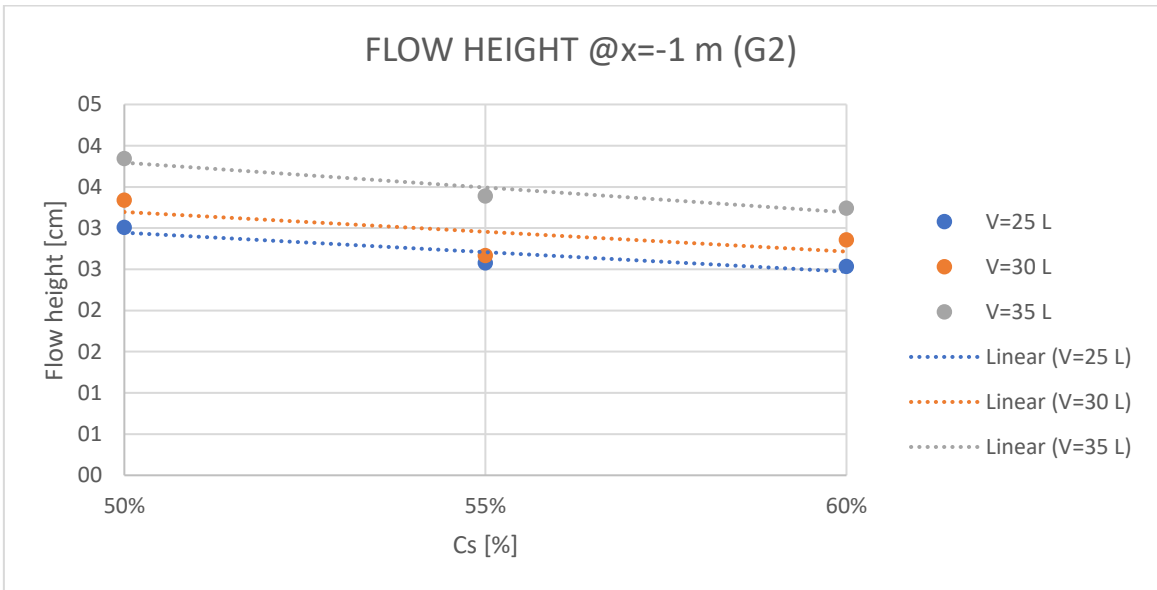


Figure 46: averaged maximum flow height at -1 m in function of solid concentration and volume

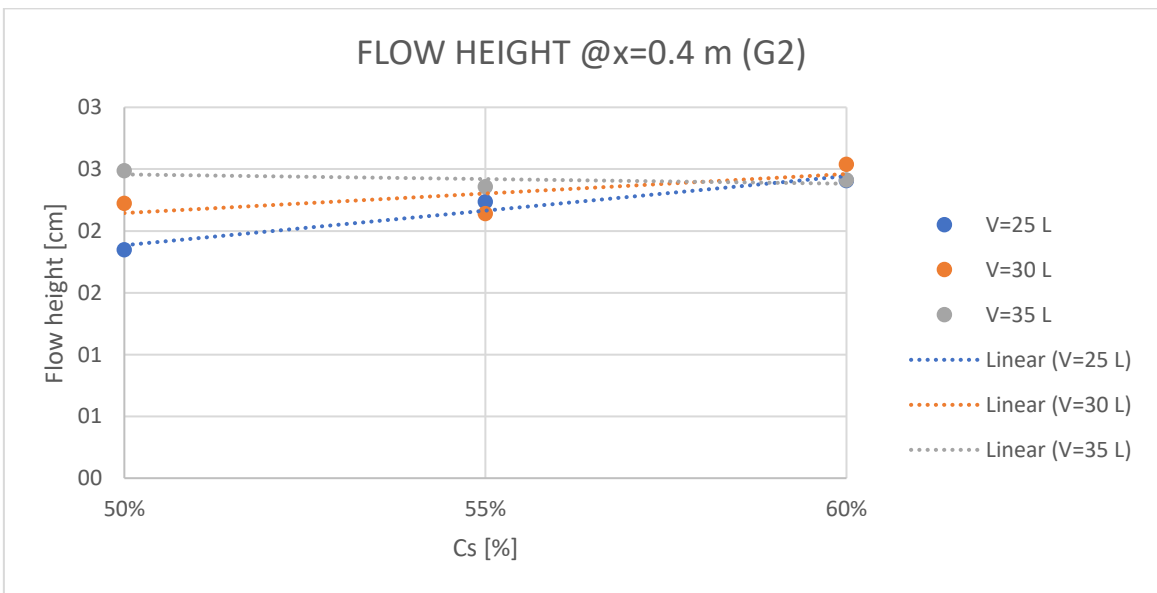


Figure 47: averaged maximum flow height at 0.4 m in function of solid concentration and volume

Considering the scaling issues presented in chapter 1.4.1., the flow height should be equal to approximately 5 cm, to represent a prototype debris flow of 1 m thickness. In these experiments, the flow heights have values around 3-4 cm. As for the velocity, this

scaling ($\lambda = \frac{1}{20}$) is not able to exactly represent a natural debris flows, but only a thinner flow.

3.7. Froude number

Froude number has been calculated at -2 m and -1 m, where both the velocity and the flow height are available. The following formula has been used:

$$Fr = \frac{v_{flow\ front}}{\sqrt{gh_{max}}} \quad (40)$$

The results are reported in Figures 48 and 49. It is expected that, increasing the solid concentration, the Froude number decreases, as the velocity decreases and the flow becomes thicker.

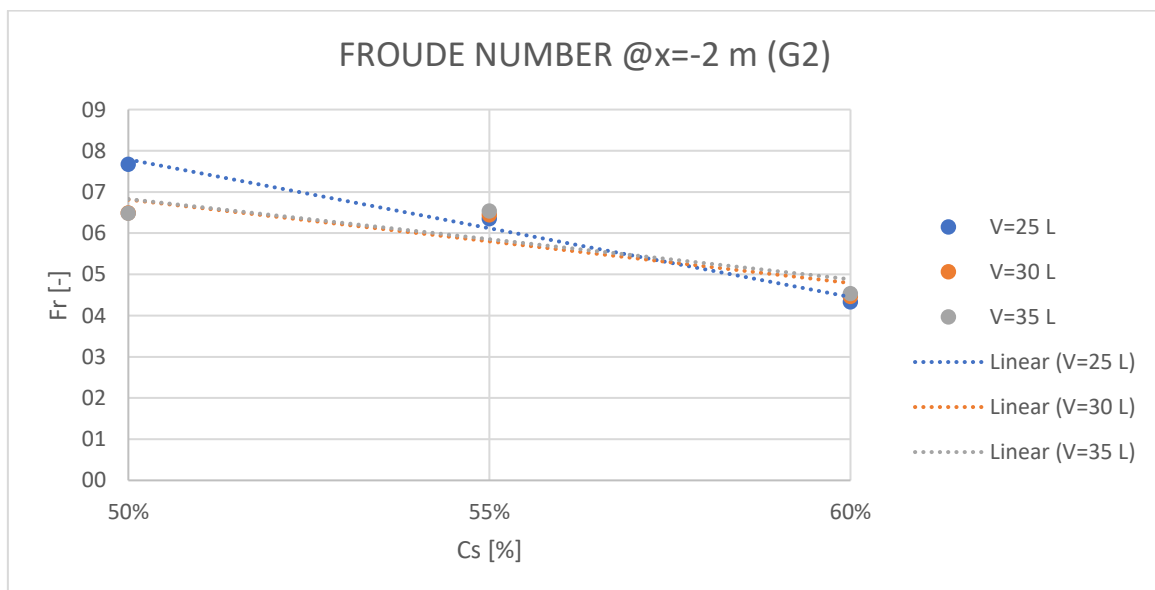


Figure 48: averaged Froude number at -2 m in function of solid concentration and volume

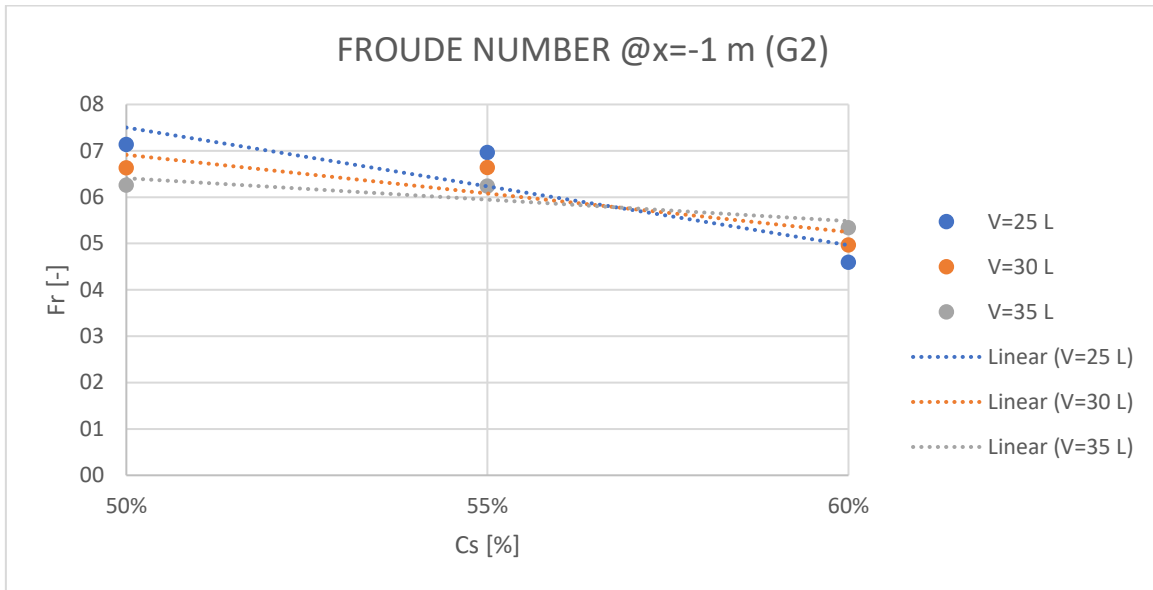


Figure 49: averaged Froude number at -1 m in function of solid concentration and volume

The values of the Froude number obtained in these tests are quite high (between 5 and 8) compared to the values that are usually observed in nature (around 3). This is a result of the high velocities and low thicknesses observed in the experiment. This confirms again the fact that small scale laboratory tests can not exactly represent natural debris flows but may characterize some particular kinds of debris flows.

3.8. Impact pressure

Impact pressure is calculated for all the tests, using the following formula:

$$p_{max} = \frac{F_{max}}{w \cdot h_{max@-1 m}} \quad (41)$$

Where w is the width of the pillar (2.5 cm) and $h_{max@-1 m}$ is the maximum flow height at -1 m. Results and calculations are reported in Appendix 4 and the results are plotted in Figure 50. The pressure shows an optimum at 55% concentration. This can be explained considering that, for low concentrations, the flow is faster but less dense. Instead, for high concentrations, the flow is slower but denser.

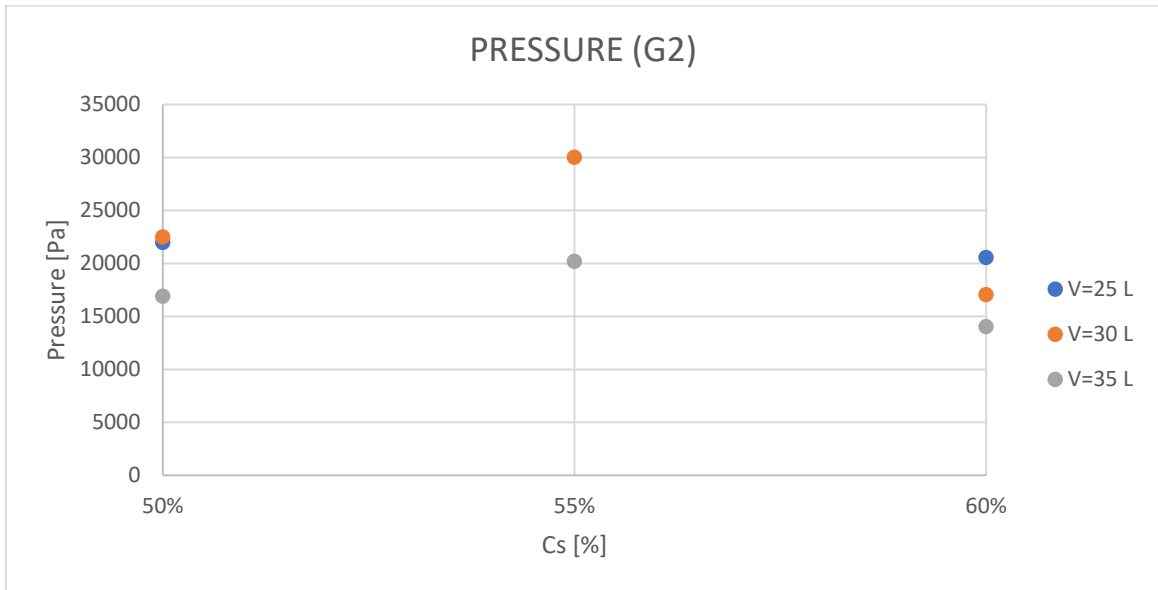


Figure 50: impact pressure on the pillar in function of solid concentration and volume

The pressure can be compared to empirical formula found in literature.

The hydrostatic model (Lichtenhan, 1973 and Armanini, 1997) can be written as:

$$p_{max} = k\rho gh \quad (42)$$

The hydrodynamic formula can be expressed as:

$$p_{max} = a\rho v^2 \quad (43)$$

Where k and a are empirical factors. k-values usually vary between 2 and 8 (Scheidl et al., 2012). In this thesis they have been back-calculated (Appendix 4) and show values between 30 and 90. a-values usually vary between 0.4 and 5 (Scheidl et al., 2012). In this thesis, they range from 0.6 to 2.2.

The hydrodynamic formula looks more appropriate to calculate the impact pressure. In general, high k-values and low a-values are observed compared to the ones reported in literature. This indicates again that the flow is fast and thin (i.e. high Froude number).

If the pressure is scaled up ($\lambda = \frac{1}{20}$), values between 280 and 600 kPa are found. Huang et al. (2007) indicate dynamic pressures of full-scale debris flows between 10 and 5000 kPa. The results of the experiments are therefore within this range.

3.9. Dimensionless parameters

As it was discussed in chapter 1.4., to be able to compare debris flows at different scales, scaling is necessary. In particular, dimensionless parameters at the grain-scale allow to compare the mechanisms of stress generation. This can provide a useful tool to classify, from a mechanical point of view, the flows and to compare them to natural ones. Furthermore, this will be a key issue to calibrate the parameters in the numerical simulation.

In this paragraph, Savage, Bagnold and friction numbers are calculated. Firstly, some material properties need to be estimated.

The grain density ρ_s is equal to $2.75 \frac{g}{cm^3}$ (chapter 2.3.).

The grain size δ used in the calculations is chosen to be equal to δ_{50} (0.88 mm for G2). These values are similar to those used by Iverson (1997), 1 mm.

The fluid density can be calculated as:

$$\rho_f = \rho_s v_{fines} + \rho_w (1 - v_{fines}) \quad (44)$$

Where: ρ_w is the density of water, ρ_s is the grain density (in this case, the density of the silty material, which has been measured equal to $2.85 \frac{g}{cm^3}$) and v_{fines} is the fine volume fraction of fluid. This has been calculated considering as fines the material below 0.03 mm and using the following equation:

$$v_{fines} = \frac{V_{fines}}{V_{fines} + V_w} \quad (45)$$

Where $V_{fines} = (M_{s,tot} \cdot \%fines) / \rho_s$ and $\%fines$ is the percentage of mass of the material finer than 0.03 mm, calculated from the grain size distribution. For G2, this is equal to 9.7%; for G1, this is equal to 3.4%.

The friction angle φ is considered constant and equal to 20° . Some other works assume an angle of 30° (Braat, 2014; Iverson, 1997) and of 40° (Iverson, 1997, for the USGS flume experiment). A lower value is chosen in this thesis to take into account the very smooth flowing surface.

The viscosity has been estimated using the Einstein's formula (1906):

$$\mu = \mu_w \cdot (1 + 2.5 \cdot v_{fines}) \quad (46)$$

Where μ_w is the viscosity of water ($1.0005 \cdot 10^{-3} \text{ Pa} \cdot \text{s}$).

The number of solid grains (N) is calculated considering the basis of the flow as the layer of interest:

$$N = \frac{h_{max}}{\delta_{50}} \quad (47)$$

The shear rate is calculated using the approach followed by Iverson (1997):

$$\dot{\gamma} = \frac{v_{flow\ front}}{h_{max}} \quad (48)$$

The three dimensionless numbers are calculated at -2 m and -1 m, where both the velocity and the flow height values are available. The results of the calculations are shown in Appendix 5.

For each test type (same release volume and solid concentration), the average of each dimensionless number has been calculated and plotted in the following figures.

The range of values of the dimensionless numbers calculated in this thesis, for the USGS flume test (Iverson, 1997), in the Braat's thesis (2014) and for the Oddstad debris flow (Iverson, 1997) are reported in Table 10. This will allow to compare the results of the experiments of this thesis to other laboratory tests (Braat, 2014 and USGS test) and to a natural debris flow (Oddstad), whose total travel distance was 172 m (Schlemon et al., 1987), i.e. a distance similar to the scaling up of the experiment ($\lambda=1/20$).

Parameter	Experiments	Braat (2014)	USGS	Oddstad debris flow, 4th January 1982
NSav	0.026-0.315	0.3-3.5	0.2	0.0002
NBag	140-297	34-1571	400	4
Nfric	852-5381	82-1741	2000	20000

Table 10: dimensionless parameters calculated for the experiments in this thesis, for laboratory tests (Braat, 2014; USGS flume test, from Iverson, 1997) and for Oddstad debris flow (Iverson, 1997)

3.9.1. Savage number

Savage number (23) is the ratio between collisional and frictional stresses. At both locations, the calculated Savage numbers (Figures 51 and 52) have an order of magnitude similar to the transition value from frictional to collisional behaviour (0.1, as indicated by Savage and Hutter, 1989). This means that both stresses are significantly affecting the behaviour of this flow. As shown in Table 10, natural debris flows usually show much lower values of Savage number, as the frictional stresses dominate on collisional stresses.

The values obtained in this thesis are comparable to those of the USGS flume experiment and to the small-scale experiments of Braat (2014). It can be therefore argued that small-scale experiments tend to overestimate the importance of collisional stresses, as a result of a thin and fast flow, as discussed in chapter 3.7.

The trend with volume and solid concentration is not clear. However, regarding the solid concentration, it can be hypothesized that an increase in solid concentration will increase the flow height and decrease the shear rate and therefore reducing the Savage number. Limiting the analysis to the concentrations 55% and 60%, the 55% concentration can be considered more collisional, while the 60% concentration more frictional.

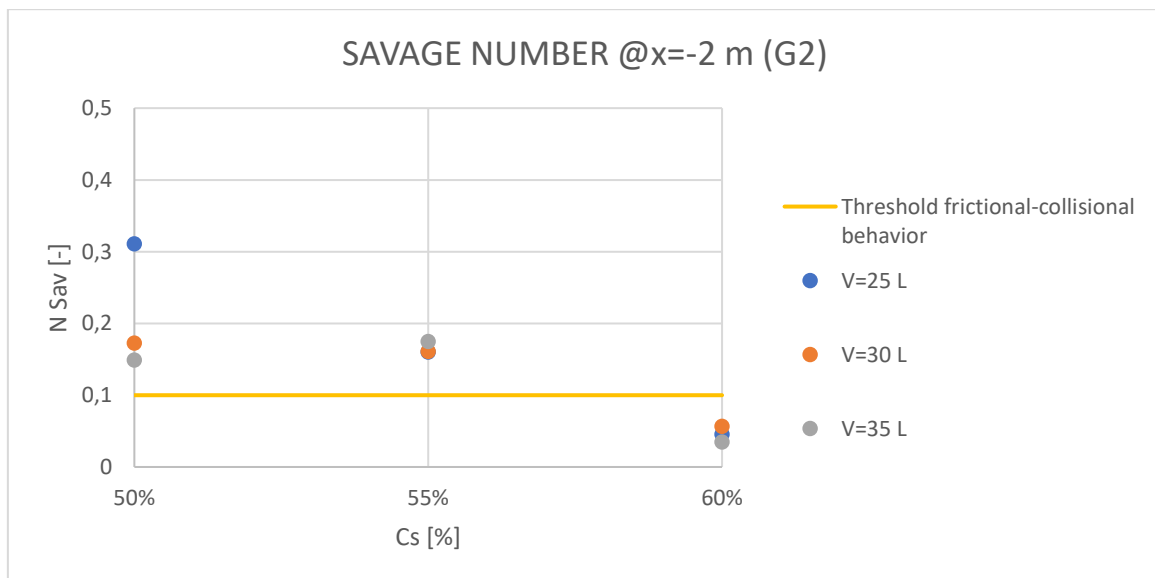


Figure 51: averaged Savage number at -2 m in function of solid concentration and volume

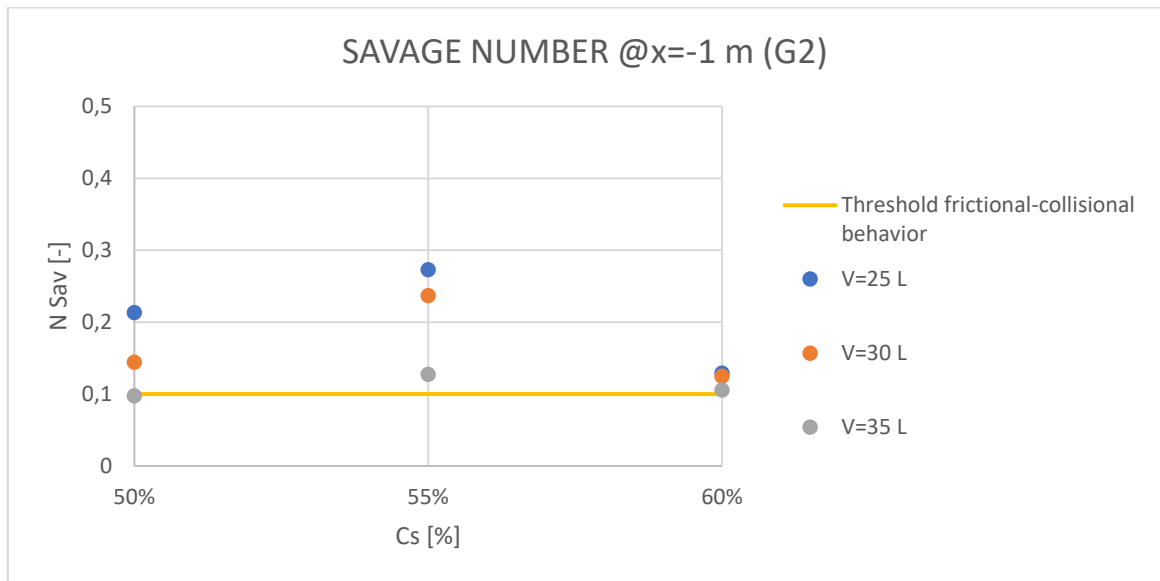


Figure 52: averaged Savage number at -1 m in function of solid concentration and volume

3.9.2. Bagnold number

Bagnold number (24) is the ratio between collisional and viscous stresses. At both locations, the calculated Bagnold numbers (Figures 53 and 54) have an order of magnitude similar to the transition value from viscous to collisional behaviour (200, as indicated by Iverson, 1997). This means that both stresses are significantly affecting the behaviour of this flow. As shown in Table 10, natural debris flows usually show much lower values of Bagnold number, as the viscous stresses dominate on collisional stresses.

The values obtained in this thesis are comparable to those of the USGS flume experiment and to the small-scale experiments of Braat (2014). Small-scale experiments overestimate again collisional stresses.

The trend with solid concentration is again difficult to be explained. In this case, the Bagnold number should increase with the solid concentration since the term $\frac{C_s}{1-C_s}$ increases. However, the Bagnold number decreases with solid concentration since the shear rate decreases and the viscosity increases. An optimum may therefore be present, but more concentrations should be tested to define its position.

Limiting the analysis to the concentrations 55% and 60%, the 55% concentration can be considered more collisional, while the 60% concentration more viscous.

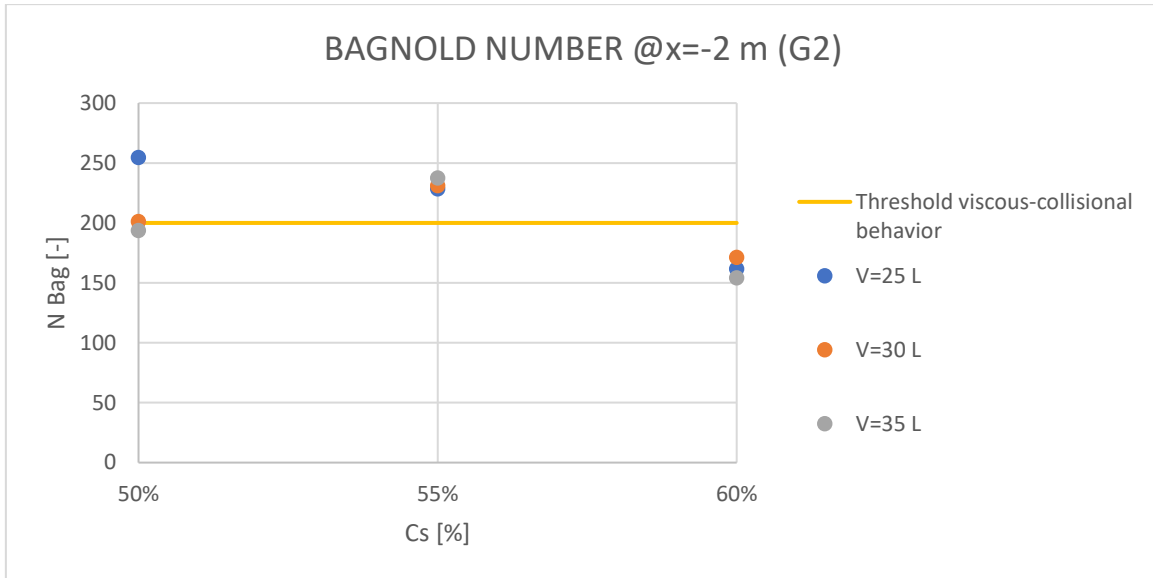


Figure 53: averaged Bagnold number at -2 m in function of solid concentration and volume

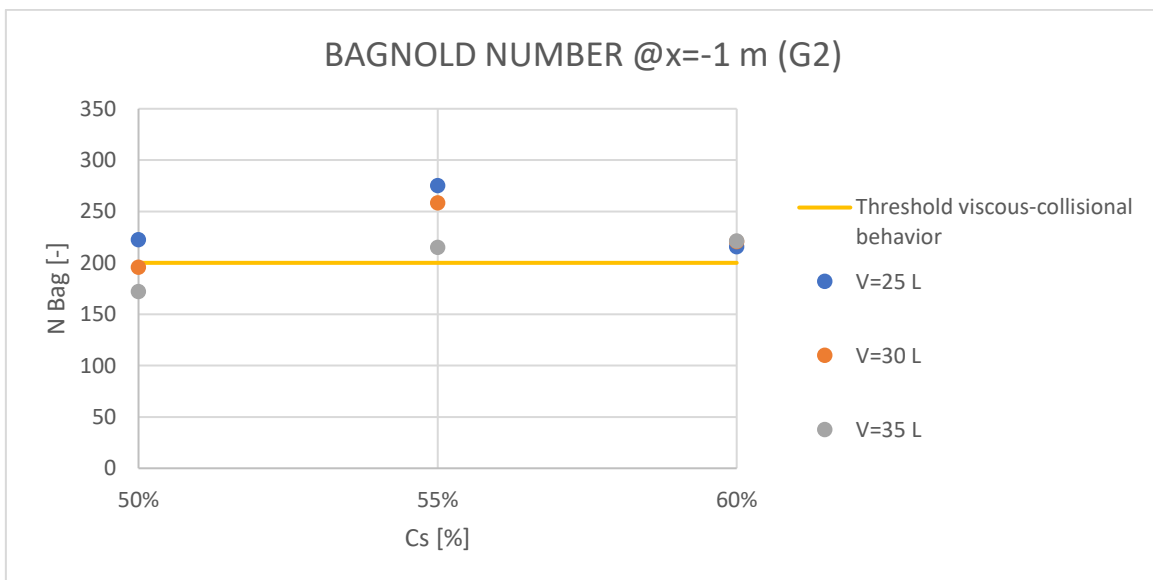


Figure 54: averaged Bagnold number at -1 m in function of solid concentration and volume

3.9.3. Friction number

Friction number (28) is the ratio between frictional and viscous stresses. At both locations, the calculated friction numbers (Figures 55 and 56) have an order of magnitude similar to the transition value from viscous to frictional behaviour (1400, as indicated by Iverson and LaHusen, 1993). This means that both stresses are significantly affecting the behaviour of this flow. As shown in Table 10, natural debris flows usually show much higher values of friction number, as the frictional stresses dominate on viscous stresses.

The values obtained in this thesis are comparable to those of the USGS flume experiment and to the small-scale experiments of Braat (2014). Small-scale experiments overestimate viscous stress over frictional stress.

The trend with solid concentration is complex. In this case, the friction number should increase with the solid concentration since the term $\frac{C_s}{1-C_s}$ increases and the flow height increases. However, the friction number decreases with solid concentration since the viscosity increases. An optimum may therefore be present, but more concentrations should be tested to define its position.

For the concentrations tested here, an increasing trend is shown. The 55% concentration could be characterized by the same importance of viscous and frictional stresses; the 60% concentration appears more friction dominated.

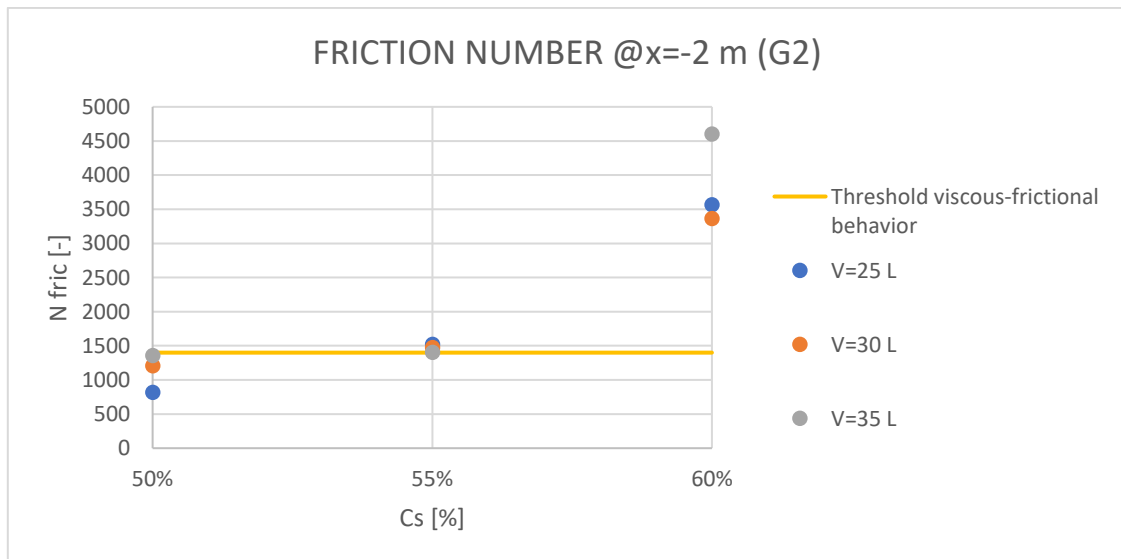


Figure 55: averaged friction number at -2 m in function of solid concentration and volume

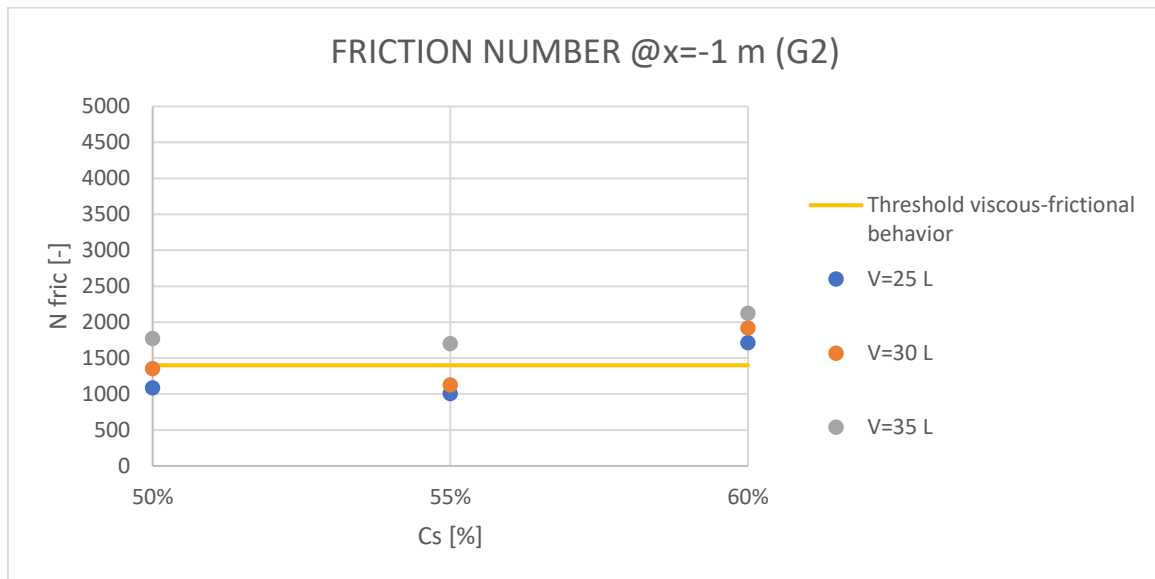


Figure 56: averaged friction number at -1 m in function of solid concentration and volume

3.9.4. Discussion

As shown by the data collected by Iverson (1997) shown in Table 10, natural debris flows exhibit the following relative importance of mechanisms of stress generation: frictional over viscous over collisional. Small-scale experiments in this thesis, in the USGS flume experiment and in the small-scale tests of Braat (2014) show almost the same importance of all these stresses. An important peculiarity of these kind of experiments is the overestimation of collisional stresses; it can be concluded that small-scale experiments may be particularly useful for the physical modelling of thin and fast debris flows.

For the numerical simulation of the laboratory tests of this thesis, two kinds of flows can be classified, even though all the stress mechanisms are important in these kind of flows:

- Frictional debris flow: 60% of solid concentration.
- Viscous/turbulent debris flow: 55% of solid concentration.

This will be useful, in the following chapter, to find a relationship between the kind of flow and the parameters to be used in the numerical simulation (friction and turbulence

coefficients). The viscous and turbulent behaviours have been put together, since, as it will be discussed later, the turbulence parameter - ξ - used in the Voellmy rheology affects both stress mechanisms.

4. Numerical simulations of laboratory tests

Numerical simulations of the laboratory tests described in the previous chapters have been carried out using the RAMMS::DEBRISFLOW software (version 1.7.17). The aim is to calibrate the parameters of the Voellmy rheology that better represent the flow behaviour of these small-scale tests.

4.1. Simulation procedure in RAMMS

4.1.1. Simulation procedure and input parameters in RAMMS

To perform a numerical simulation in RAMMS, it is necessary to set some preferences and to input the following data: topography (digital elevation model, DEM), release area (polygon and height), Voellmy rheological parameters.

The following procedure has been adopted to simulate the debris flow tests in RAMMS (RAMMS manual):

i. A DEM file has been prepared in Excel. An ESRI ASCII grid was created (Figure 57): each value corresponds to the height (in meters) of a point belonging to the topographical surface of the model. Points are equally spaced 1 cm in both x and y directions (resolution of 0.01 m). The model has therefore not been scaled up (as in Yifru, 2014 and in Scherchan, 2016), since this version of RAMMS allows a resolution inferior to 1 m. The geometry of the model is shown in Figures 58 and 59.

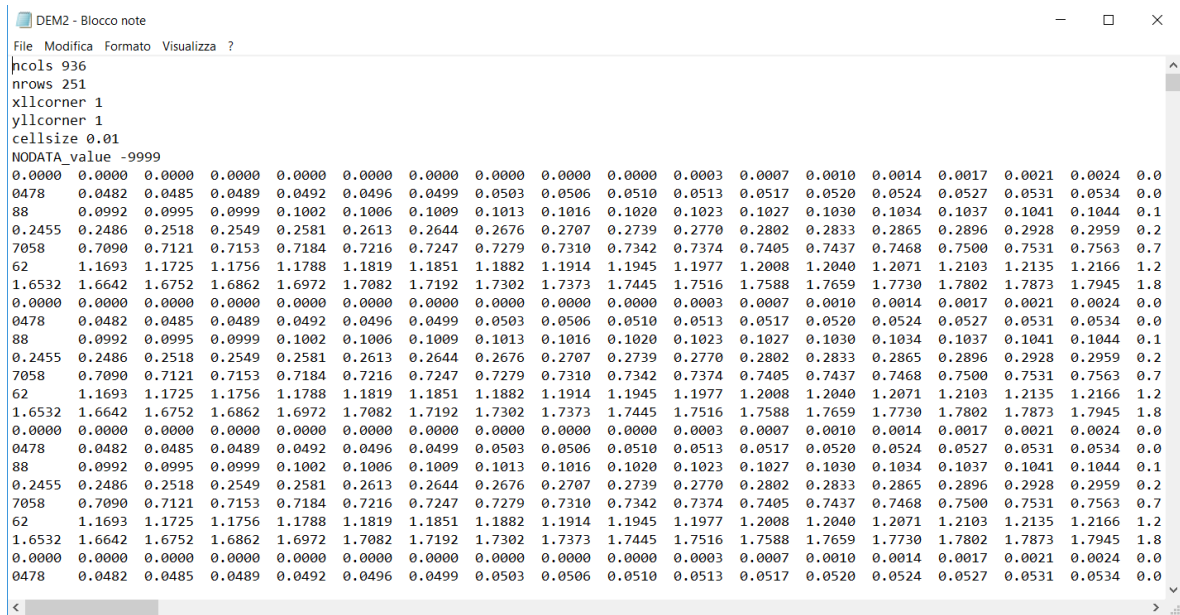


Figure 57: ESRI ASCII grid

- ii. The calculation domain is chosen to enclose the full model previously built.
- iii. The release area is drawn on that surface (red surface in Figures 58 and 59). A precise representation of the releasing mechanism, in which the debris mass is dropped from a certain height, is not possible. The release volume is therefore placed on the topographical surface and made of vertical lateral surfaces. When the simulation starts, the volume will ‘collapse’ and flow down without dropping vertically from the cylinder. It is believed that this approximation will not affect the results, since when the material is dropped from the cylinder, it will lose part of the energy acquired, through the impact with the flume surface. Furthermore, this approximation may influence the behaviour at the initial stages of the flow, but in the points of interest (e.g. at -2 m and -1 m and in the deposition zone), the effect should be negligible.

For the same reason, it was decided to simplify the release surface, drawing a square (37 cm sides) instead of a circle. The release height should finally be defined, accordingly to the release volume. RAMMS calculate the release volume as:

$$V = A_{inclined}h$$

Where $A_{inclined}$ is the inclined area ($A/\cos(\text{inclination}) = 37^2/\cos 36^\circ = 17 \text{ cm}^2$).

Therefore, the release heights are defined as follows (Table 11):

V [L]	H [m]
25	0.147
30	0.176
35	0.206

Table 11: definition of release heights based on release volume

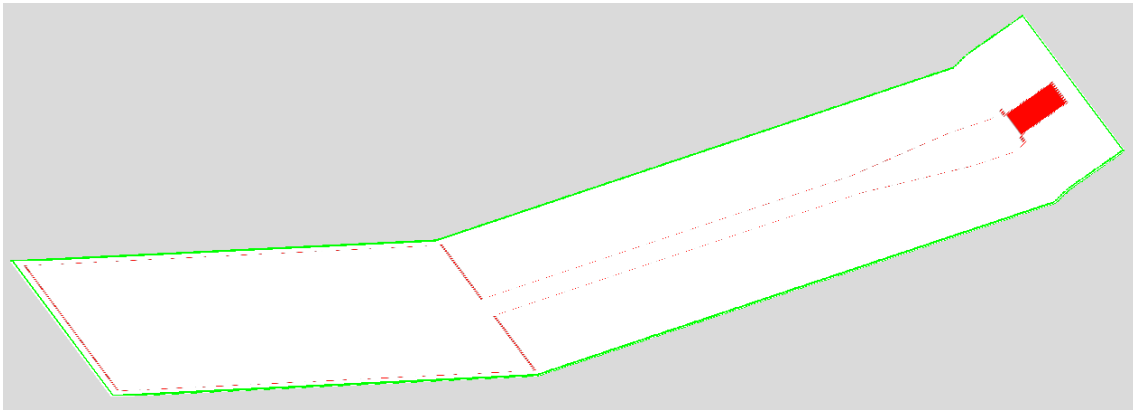


Figure 58: three-dimensional geometry of the model

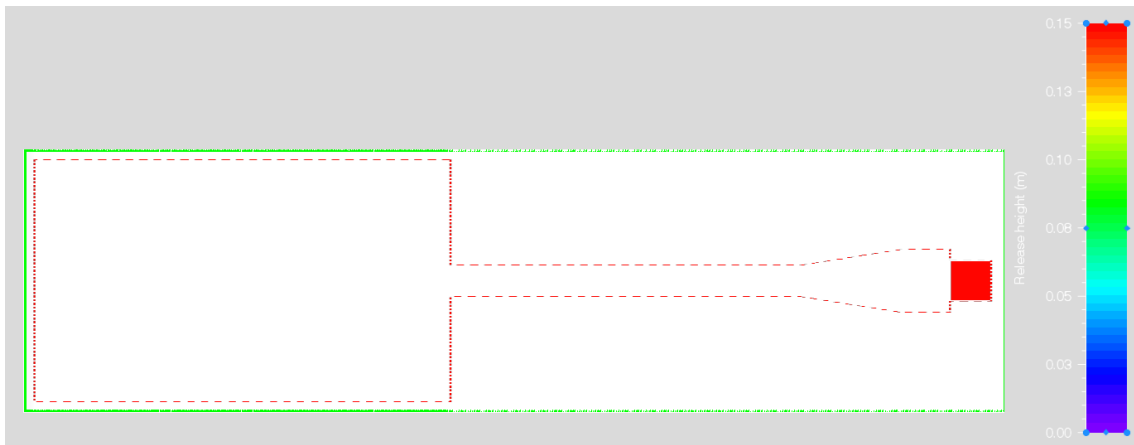


Figure 59: planimetric geometry of the model

iv. To represent the vertical walls, it is necessary to create an ‘Obstacle/Dam File’ which corresponds to a no flux boundary condition (red dashed line in Figures 58 and 59). This

is the best approximation of the lateral surface to obtain meaningful results. However, as it will be shown in the discussion of the results, such surface is frictionless and therefore the velocity will be greater at the borders than at the centre of the flow.

v. The input parameters can then be set (Appendix 6):

- Stop parameter: percentage of total momentum equal to 5%. Different values have been tried. The results are independent of this.

- Simulation resolution: 0.01 m.

- End time: 1000 s. This doesn't affect the results since the simulation time of these laboratory tests is always equal to 10 s.

- Dump step: 0.1 s, it defines the resolution of the animation, but does not affect the simulation results.

- Density: 2000 kg/m³. This value will not affect the runout distance, flow velocity and flow height. It is therefore kept constant for all simulations.

- Lambda: the earth pressure coefficient is set to 1. This value has not been calibrated since RAMMS manual does not recommend changing this default value.

- Numerical scheme: second order scheme.

- Cut-off height: 0.000001 m.

- Curvature effects are active.

- Mu and xi values are then input and are kept constant on all the flow area. These values are varied for each simulation and have to be calibrated in order to find the couple of values capable of simulating the laboratory tests results.

- Yield stress is set to zero for all the simulations. The effect of this material parameter has not been analysed in this thesis.

- Block release is used, taking the area and the flow height previously defined.

- Erosion is absent in these experiments and is therefore not considered.

Finally, the simulation is started and the results can be analysed.

4.1.2. Output results in RAMMS

The software keeps calculating until the percentage of total momentum falls below 5%. However, in the simulation of these small-scale laboratory tests, the software

continued the calculation also below the threshold value, for a simulation time of 10 s. This is probably due to a software setting, which cannot be modified.

The output parameters recorded after each simulation are the following:

- Deposition shape at the end of the flow, $t=10$ s (Figure 60).
- Runout length. The value has been calculated from the end of the flume (beginning of the deposition area) and corresponding to a flow height of 1 mm (Figure 61).
- Maximum flow velocity and flow height at -2 m, -1 m (Figures 62 and 63).

Furthermore, it is useful to calculate the following quantities:

- Froude number (at -2 m and -1 m) as:

$$Fr = \frac{v_{max}}{\sqrt{gh_{max}}} \quad (49)$$

- Dimensionless numbers (Savage, Bagnold, friction numbers) in both locations. Analysing the structure of these dimensionless numbers, they are made of two components: a function of debris flow properties and parameters which can be considered constant during the motion ($\rho_s, \rho_f, \delta, v_s, \mu, g, \tan(\varphi)$); a dynamic component (depending on $\dot{\gamma}$ and h). Since the numerical simulation only depends on the latter, it is useful to compare the laboratory tests and the RAMMS results, through these numbers, which are closely related to the dimensionless numbers defined previously:

$$N'_{Sav} = \frac{\dot{\gamma}^2}{h} \quad (50)$$

$$N'_{Bag} = \dot{\gamma} \quad (51)$$

$$N'_{fric} = \frac{h}{\dot{\gamma}} \quad (52)$$

In the following, with abuse of notation, these numbers will be called ‘dimensionless numbers’.

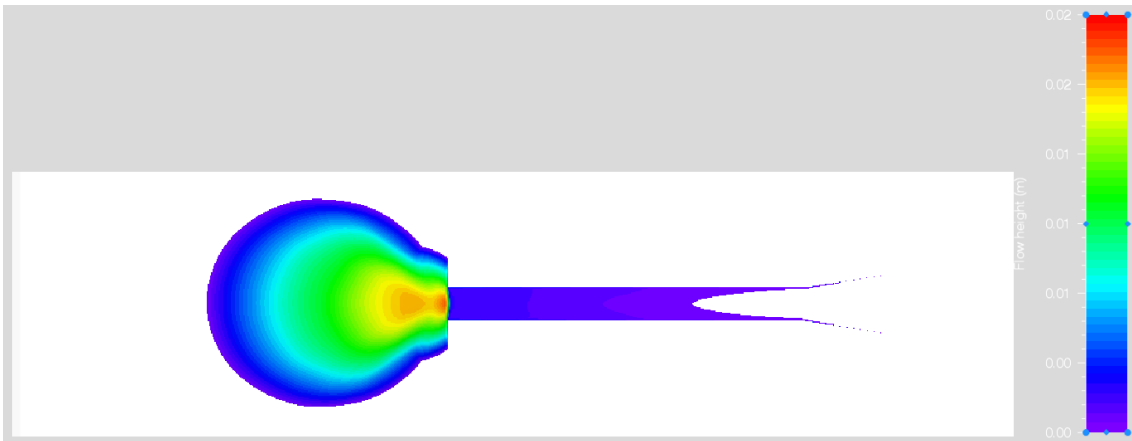


Figure 60: deposit shape (for VI, $\mu=0.05$, $\xi=500 \text{ m/s}^2$)

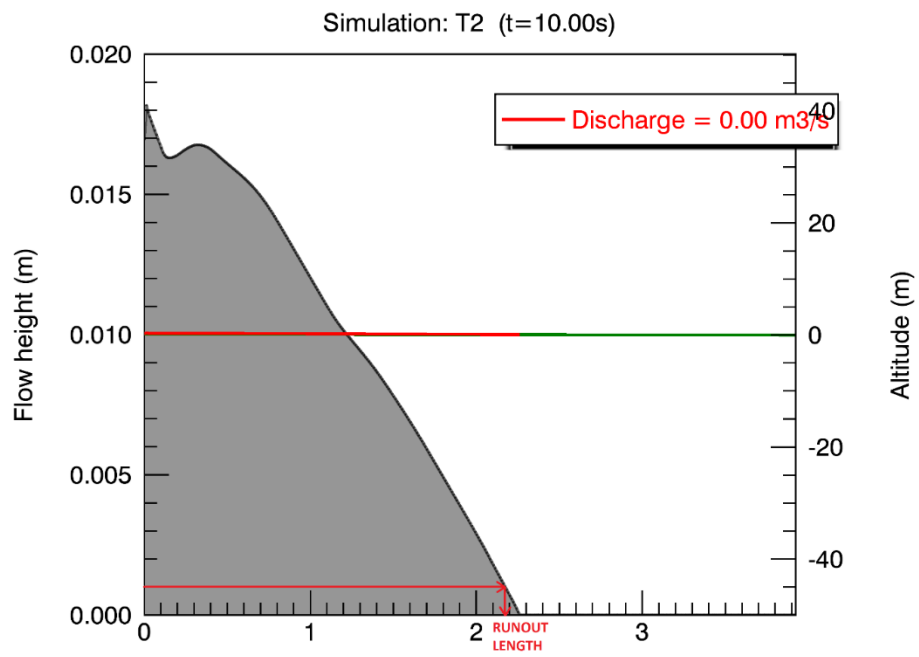


Figure 61: calculation of runout length (for VI, $\mu=0.05$, $\xi=500 \text{ m/s}^2$)

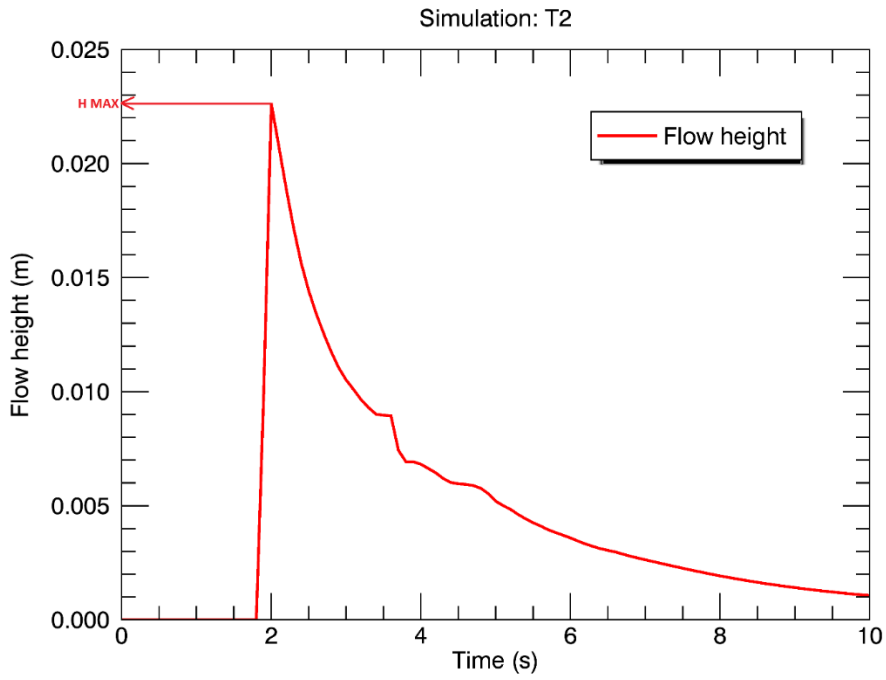


Figure 62: calculation of maximum flow height (at -1 m, for V1, $\mu=0.05$, $\xi=500 \text{ m/s}^2$)

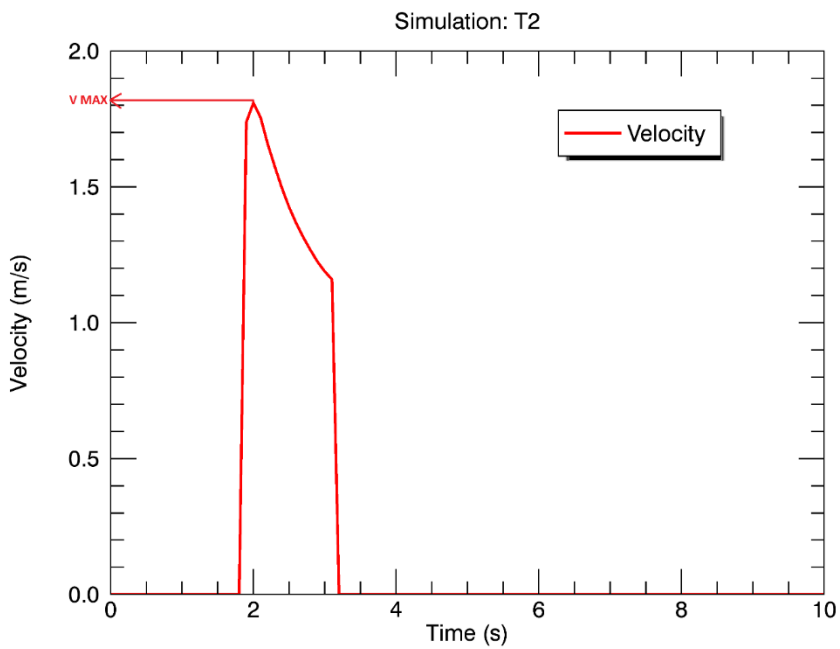


Figure 63: calculation of maximum flow velocity (at -1 m, for V1, $\mu=0.05$, $\xi=500 \text{ m/s}^2$)

4.2. Influence of Voellmy input parameters on the flow behavior

In this chapter, the influence of the parameters of the Voellmy rheology (friction parameter, μ , and turbulence factor, ξ) is analysed in terms of runout distance, flow velocity, flow height, Froude number and dimensionless parameters. This will allow to understand the physical significance of these material parameters and which output they are affecting mostly.

The choice of the values for the numerical simulation is not straightforward. RAMMS manual suggests the following values:

- μ normally ranges between 0.05 and 0.4. Some authors suggest to use $\mu = \tan(\alpha)$ where α is the slope angle of the depositional zone (in this case 2° and therefore $\mu=0.035$)
- ξ normally varies between 100 and 1000 m/s^2 . Granular flows usually exhibit values of 100-200 m/s^2 , while mud flows show values of 200-1000 m/s^2 .

Furthermore, it must be considered that these suggestions are given for full-scale debris flows. These recommendations might not be valid for small-scale debris flows, since, as it was discussed in chapter 3.9., stress generation mechanisms are different from natural debris flows. Calibration of these parameters is therefore fundamental.

In this work, it was chosen, after some trials, to vary μ between 0.03 and 0.15 and ξ between 250 m/s^2 and 2500 m/s^2 . Several combinations of these parameters have been tried.

4.2.1. Flow behavior

The flow behaviour is shown in Figures i to ix in Appendix 7, in terms of flow height at different times along all the flume. The screenshots are taken from the software RAMMS for volume 1 (25 L) and $\mu=0.05$ and $\xi=500 \text{ m/s}^2$.

In general, for all these combinations, the flow exhibits an initial splash, due to the fall of the release volume. Successively, the debris volume flows down along the flume and is characterized by some collisions against the lateral walls (Figure ii in Appendix 7). Then, the flow decelerates downstream, without showing any increase of velocity at the

almost end of the flume, as it was observed in the laboratory experiments. The front shape presents a wrong convexity: the flowing mass near the lateral wall travels quicker than the mass at the centre of the flume (Figure iii in Appendix 7). This is due to the frictionless boundary condition.

In the deposition zone, the debris volume is subjected to a lateral expansion greater than in the laboratory tests (Figure ix in Appendix 7). This may be due to the earth-pressure coefficient, λ , set equal to 1. As it was demonstrated by Gray et al. (1999) and Pirulli (2005), the introduction of passive and active earth-pressure coefficients (λ different from 1) is fundamental to correctly simulate the deposit shape.

4.2.2. Influence of μ and ξ on runout, flow velocity and flow height

Runout distance, flow velocity and flow height (at -2 m and -1 m), calculated for different values of μ and ξ , are reported in Figures 64 to 68, for volume 1. In these figures, the values observed experimentally are also reported (straight lines, for concentrations 1 and 2).

An increase of ξ and a decrease of μ cause an increase of runout distance and flow velocity. The influence of ξ is more important for low values of μ . The runout length is strongly controlled by μ , which particularly affects the behaviour in the deposition zone. Even ξ affects the runout distance, by controlling the flow velocity at the end of the channel. Flow velocity is mainly influenced by ξ and, to a lower extent, by μ .

The influence of these rheological parameters on the flow height is not clear from the trend of Figures 67 and 68 (in particular at -1 m). It is believed that they don't influence significantly the flow height. The small variations observed could be due to the 'splash' produced by the impact of the flowing mass against the walls.

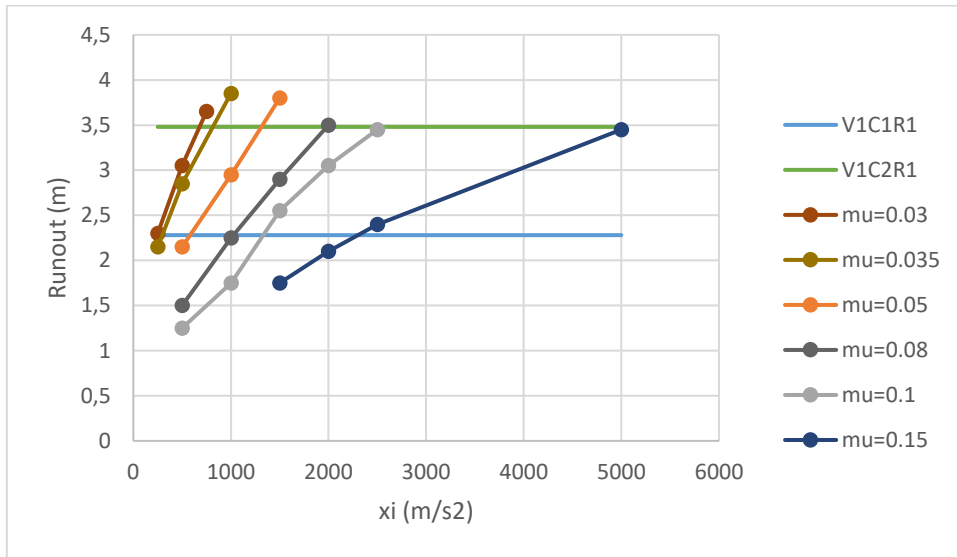


Figure 64: runout distance, in function of mu and xi (series at constant mu)

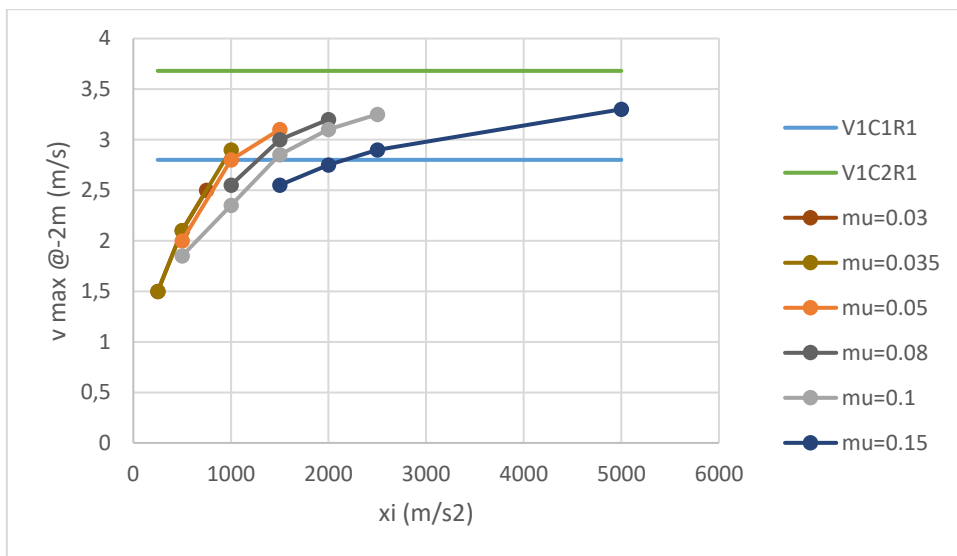


Figure 65: maximum flow velocity at -2 m, in function of mu and xi (series at constant mu)

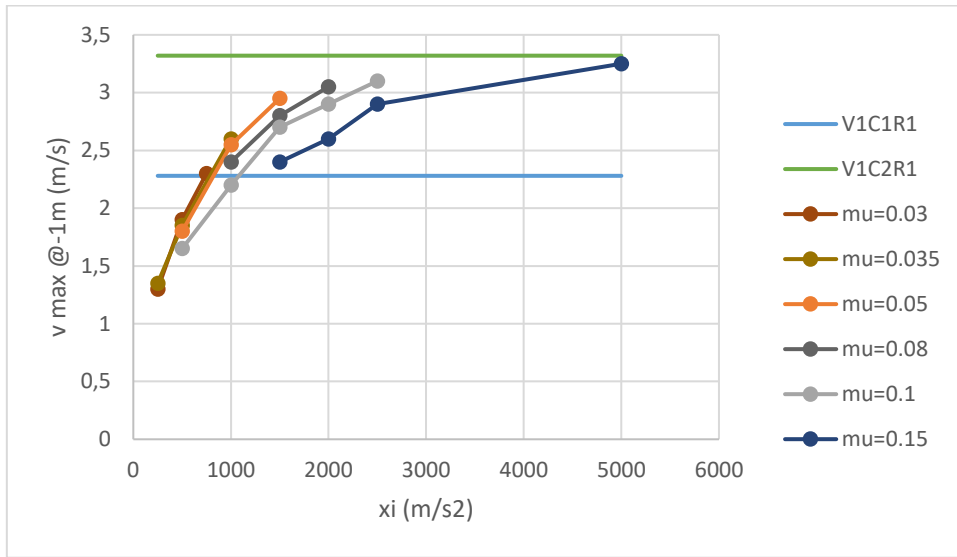


Figure 66: maximum flow velocity at -1 m, in function of μ and ξ (series at constant μ)

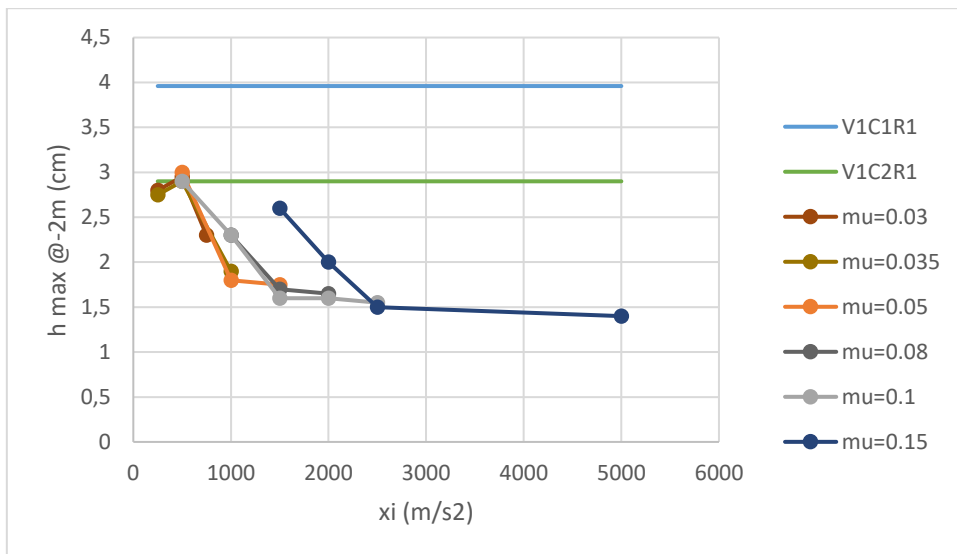


Figure 67: maximum flow height at -2 m, in function of μ and ξ (series at constant μ)

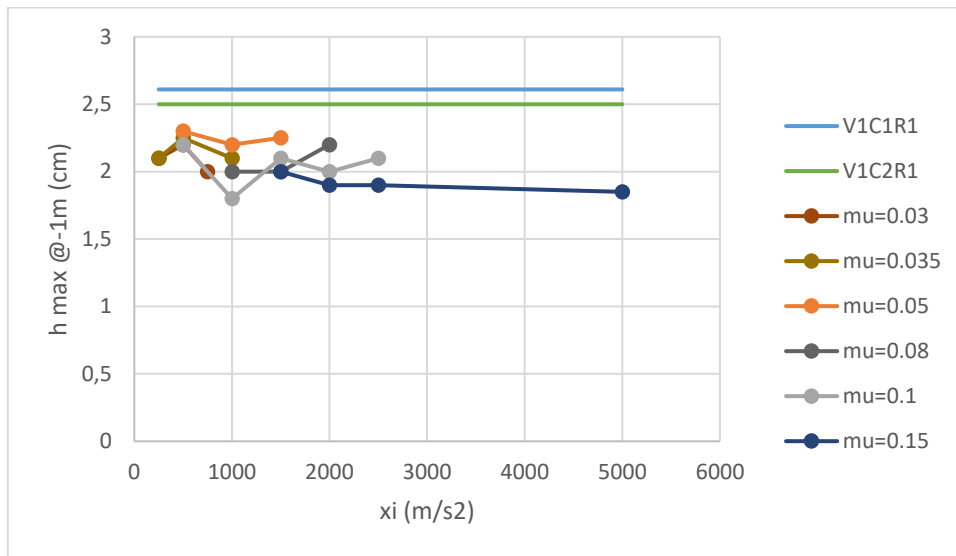


Figure 68: maximum flow height at -1 m, in function of mu and xi

Results (and in particular the runout distance) can also be plotted as series at constant xi (Figure 69).

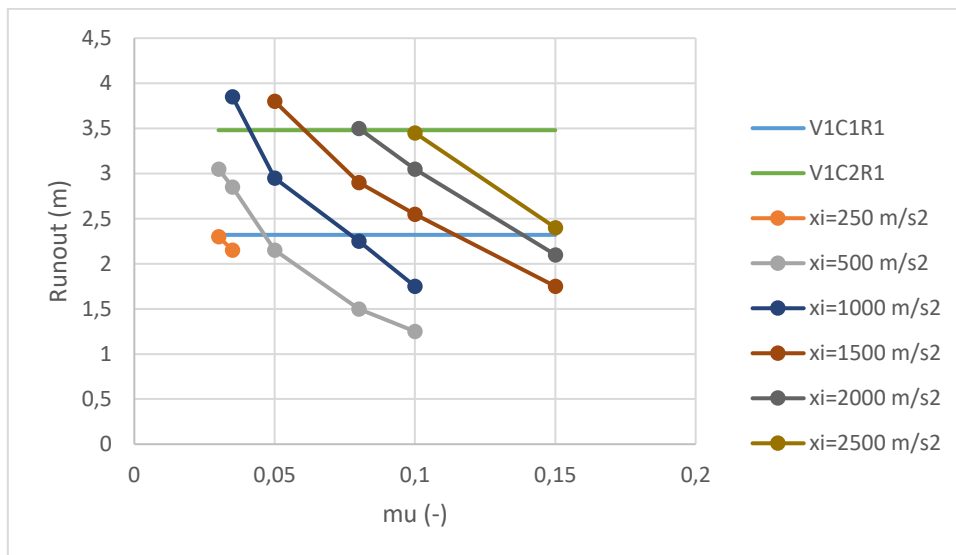


Figure 69: runout distance, in function of mu and xi (series at constant xi)

4.2.3. Influence of μ and ξ on Froude number and dimensionless parameters

Froude number is particularly influenced by ξ , while the effect of μ is very low (Figures 70 to 73). Froude number increases with ξ , as the flow is faster and thinner. High values of μ (from 0.1 to 0.15) reduce the Froude number.

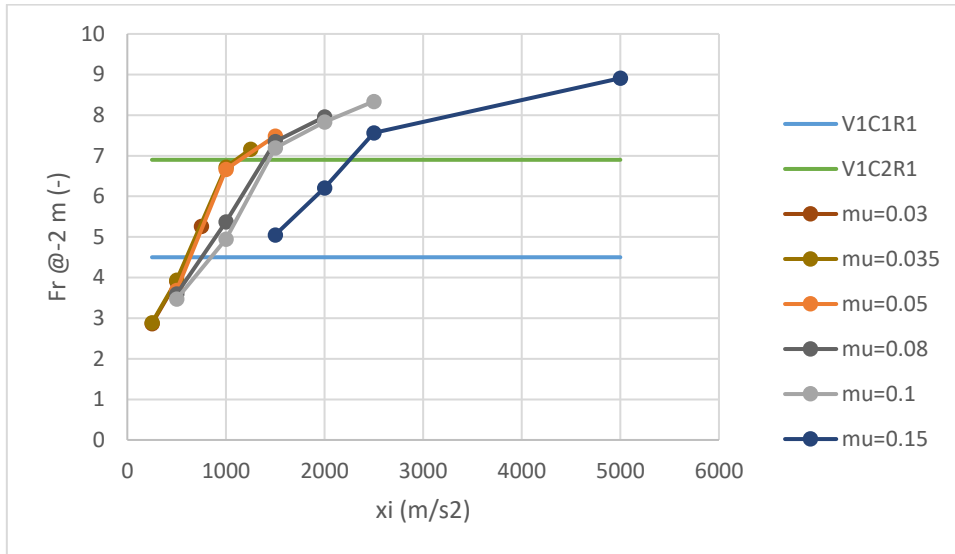


Figure 70: Froude number at -2 m, in function of μ and ξ (series at constant μ)

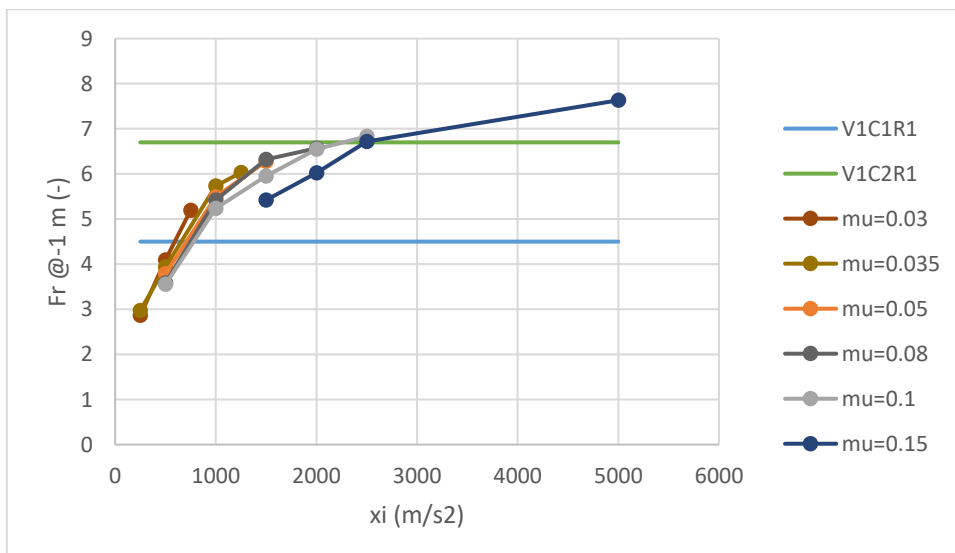


Figure 71: Froude number at -1 m, in function of μ and ξ (series at constant μ)

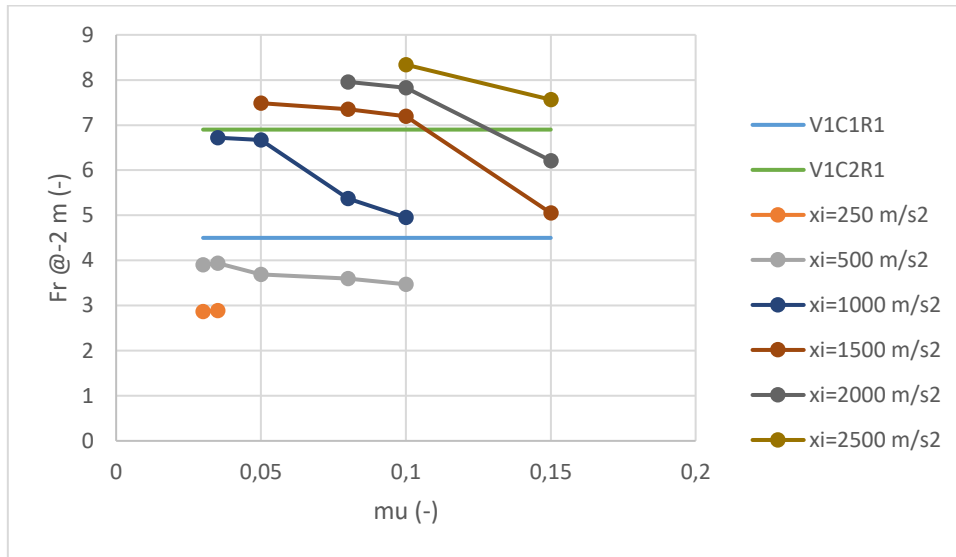


Figure 72: Froude number at -2 m, in function of mu and xi (series at constant xi)

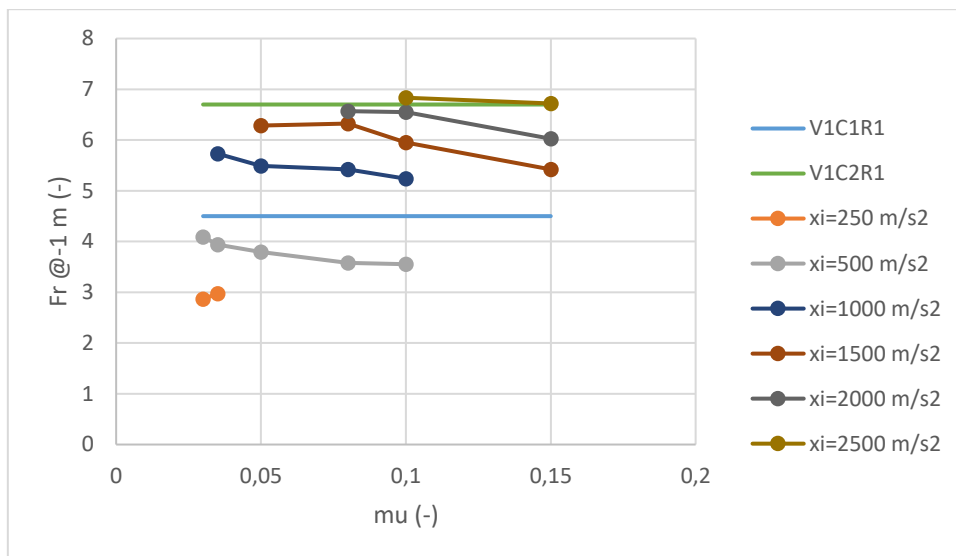


Figure 73: Froude number at -1 m, in function of mu and xi (series at constant xi)

Dimensionless numbers (N'_{sav} , N'_{Bag} , N'_{fric}) are almost constant with mu and vary with xi (Figures 74 to 85):

- An increase of xi both increases N'_{sav} and N'_{Bag} . This means that high xi values correspond to flows where collisional stresses dominate on frictional and viscous stresses.

- An increase of ξ decreases N'_{fric} . In this case, the viscous stresses dominate on the frictional ones.

ξ can thus be defined as a collisional-viscous parameter, as its increase determines a decrease of the importance of frictional stresses against collisional and viscous ones.

The effect of μ on the dimensionless numbers can only be seen at -2 m and for the highest values of μ (from 0.1 to 0.15): in this case, N'_{sav} and N'_{Bag} decrease, as frictional and viscous stresses dominate on collisional ones; N'_{fric} increases, as friction dominates on viscosity. In this sense, and for these values of μ , μ represent a friction parameter. For lower values of μ , the behaviour is almost independent of μ .

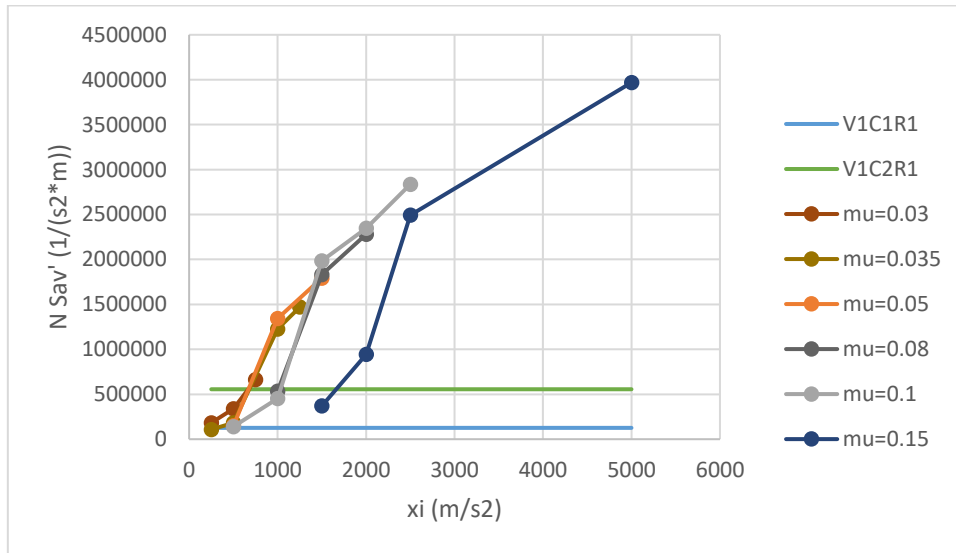


Figure 74: N'_{sav} at -2 m, in function of μ and ξ (series at constant μ)

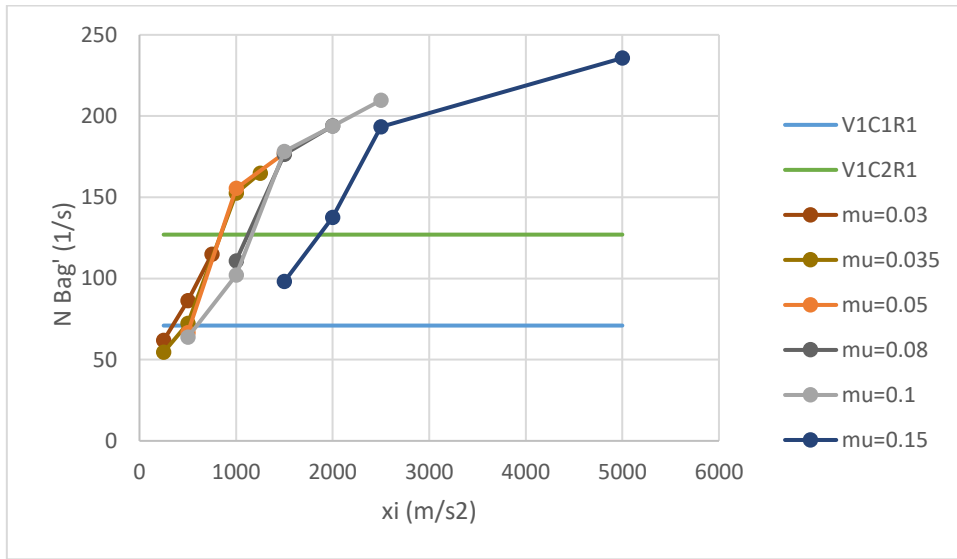


Figure 75: N'_{Bag} at -2 m, in function of μ and ξ (series at constant μ)

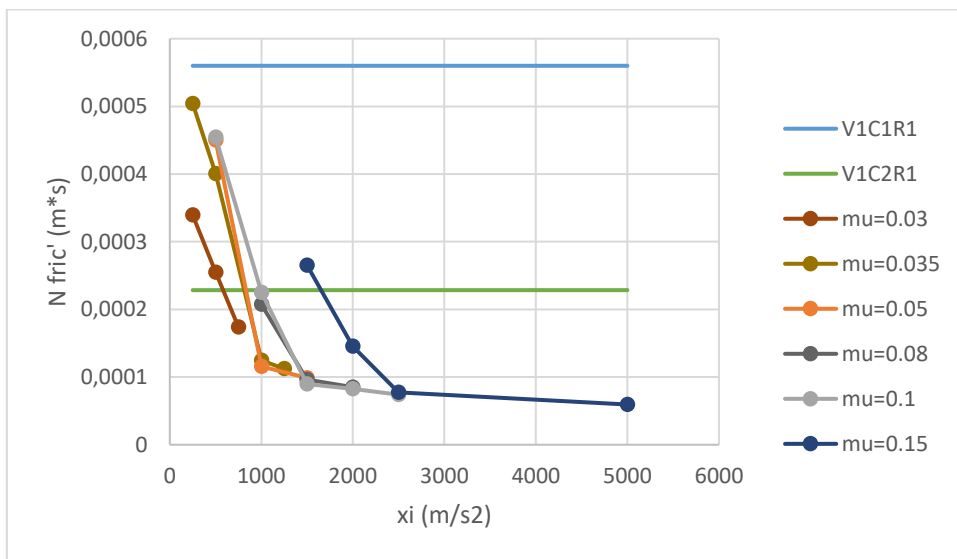


Figure 76: N'_{fric} at -2 m, in function of μ and ξ (series at constant μ)

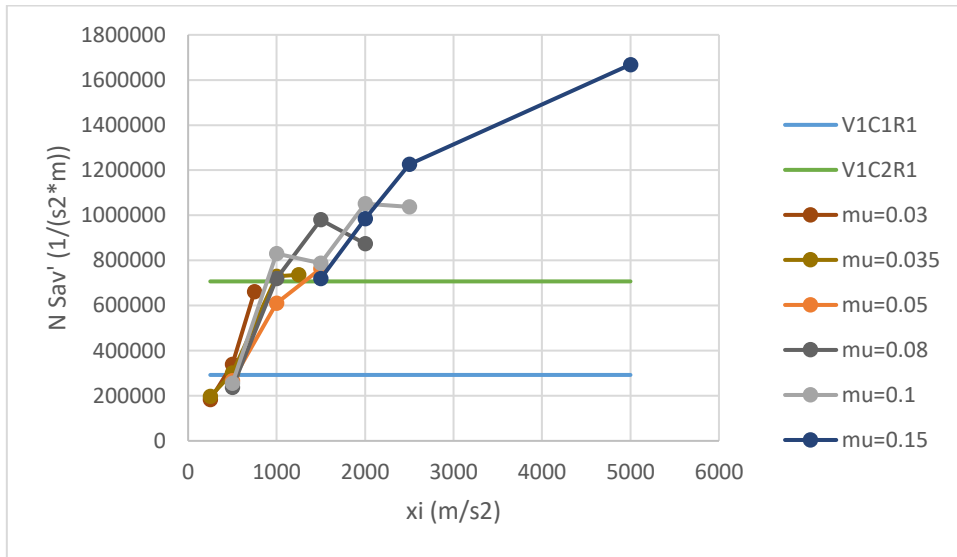


Figure 77: N'_{Sav} at -1 m, in function of μ and ξ (series at constant μ)

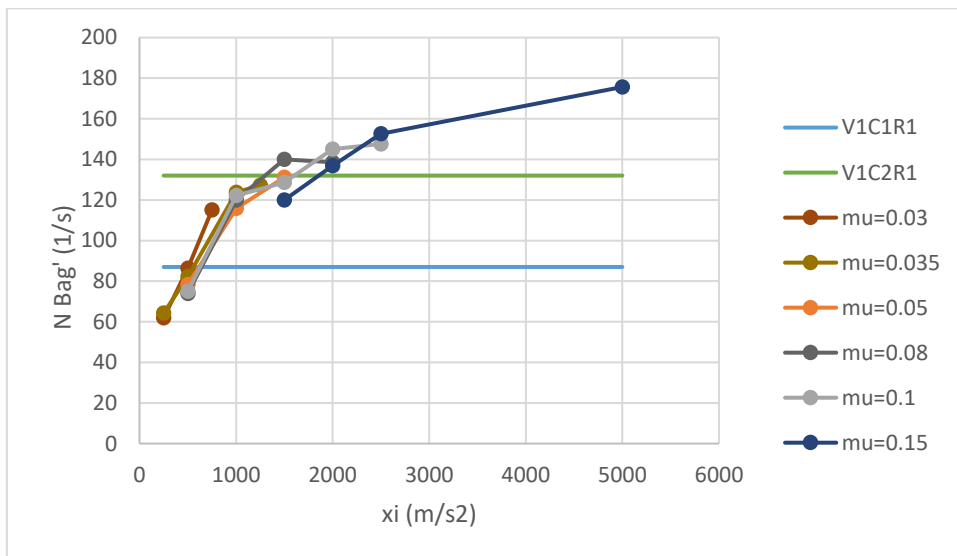


Figure 78: N'_{Bag} at -1 m, in function of μ and ξ (series at constant μ)

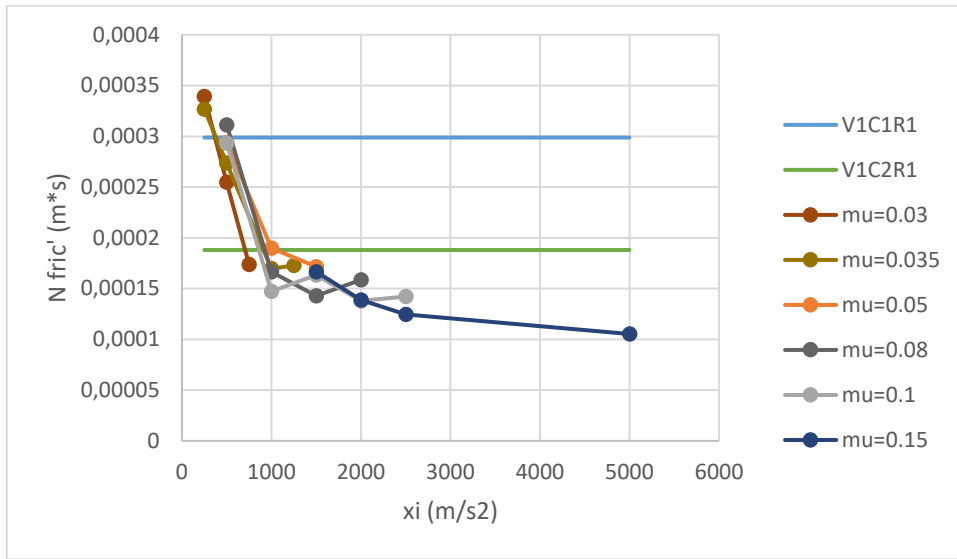


Figure 79: N'_{fric} at -1 m, in function of μ and ξ (series at constant μ)

The results can also be plotted as series at constant ξ :

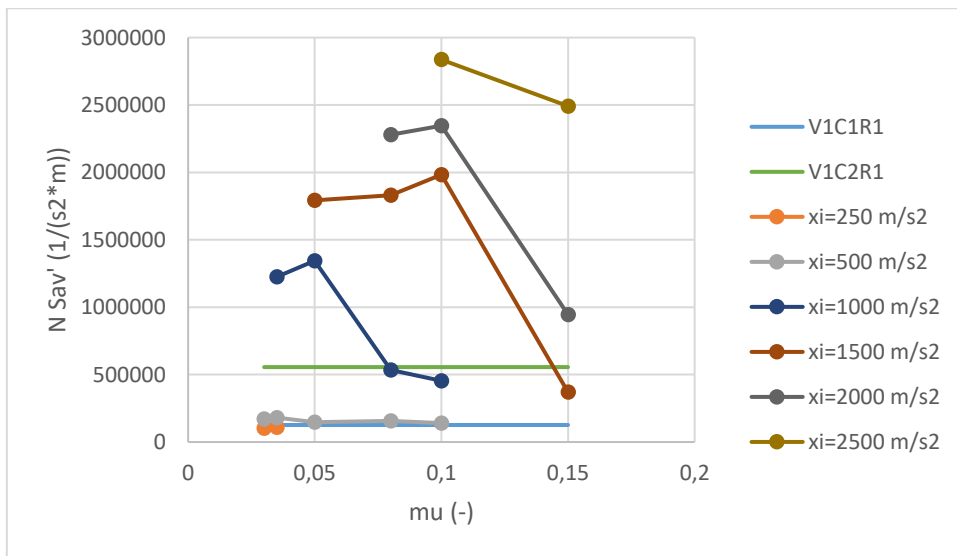


Figure 80: N'_{Sav} at -2 m, in function of μ and ξ (series at constant ξ)

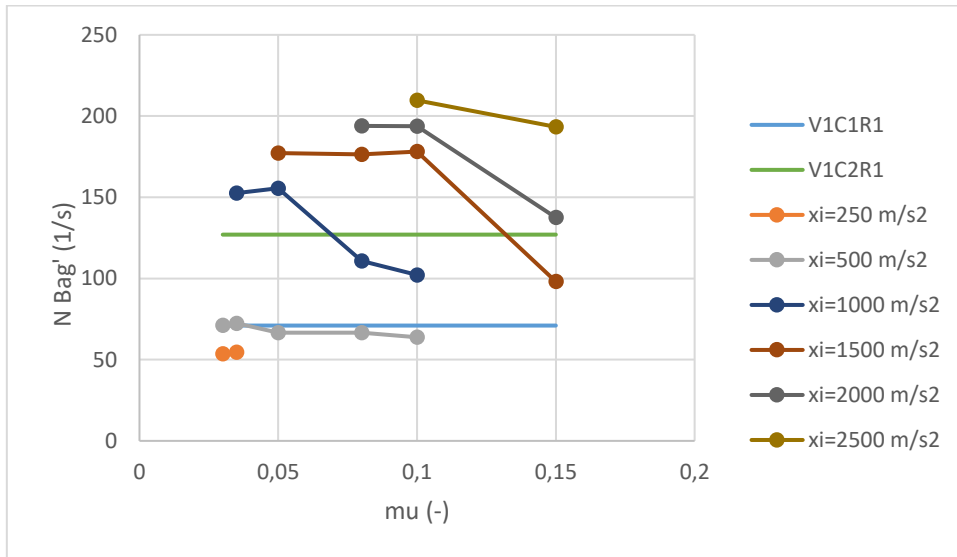


Figure 81: N'_{Bag} at -2 m, in function of μ and ξ (series at constant ξ)

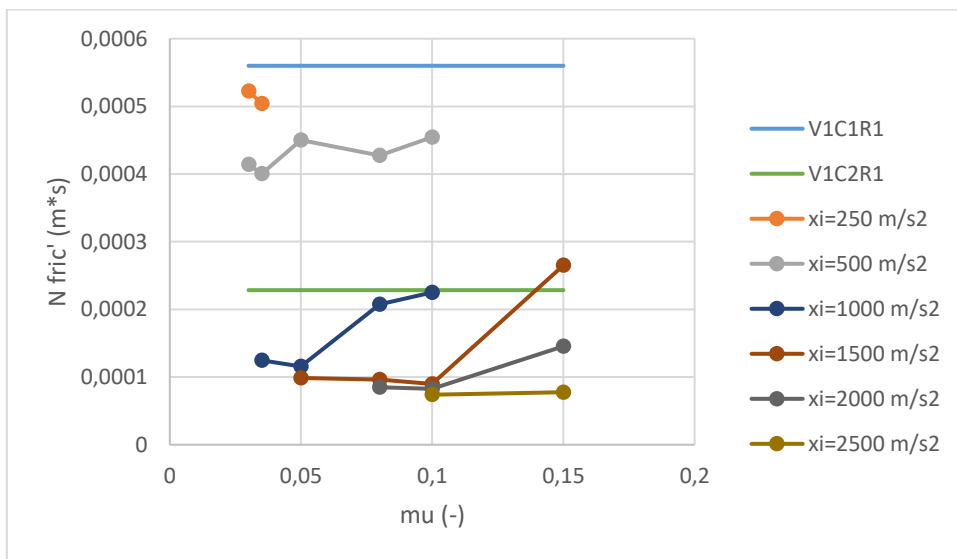


Figure 82: N'_{fric} at -2 m, in function of μ and ξ (series at constant ξ)

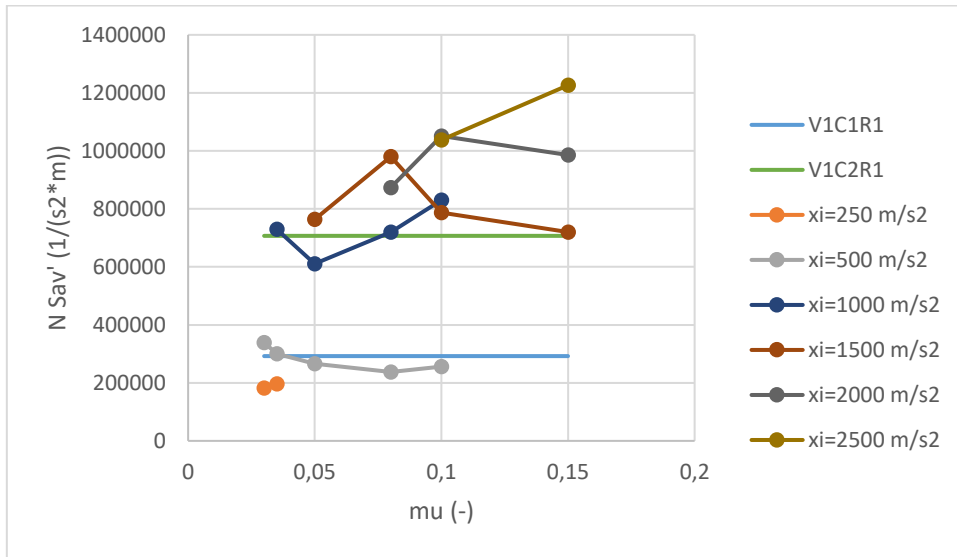


Figure 83: N'_{Sav} at -1 m, in function of μ and ξ (series at constant ξ)

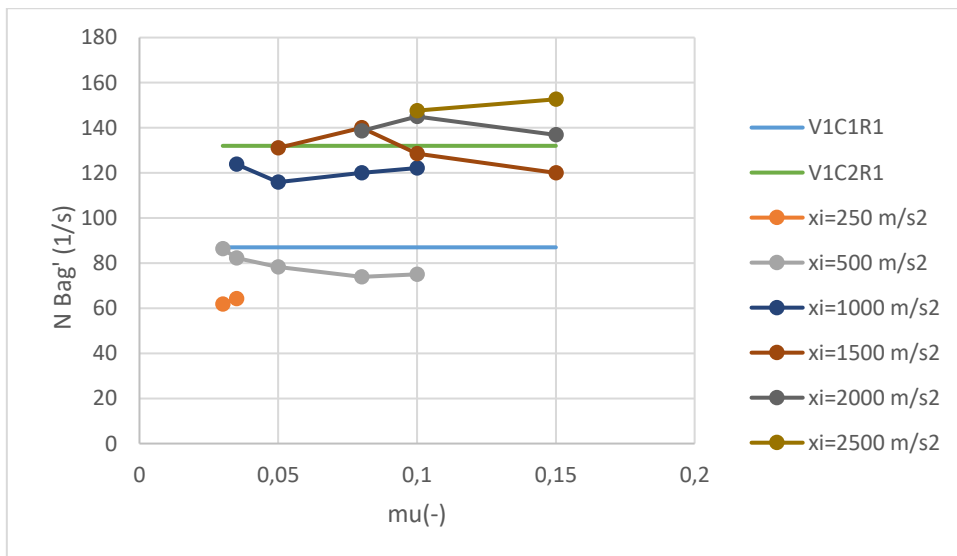


Figure 84: N'_{Bag} at -1 m, in function of μ and ξ (series at constant ξ)

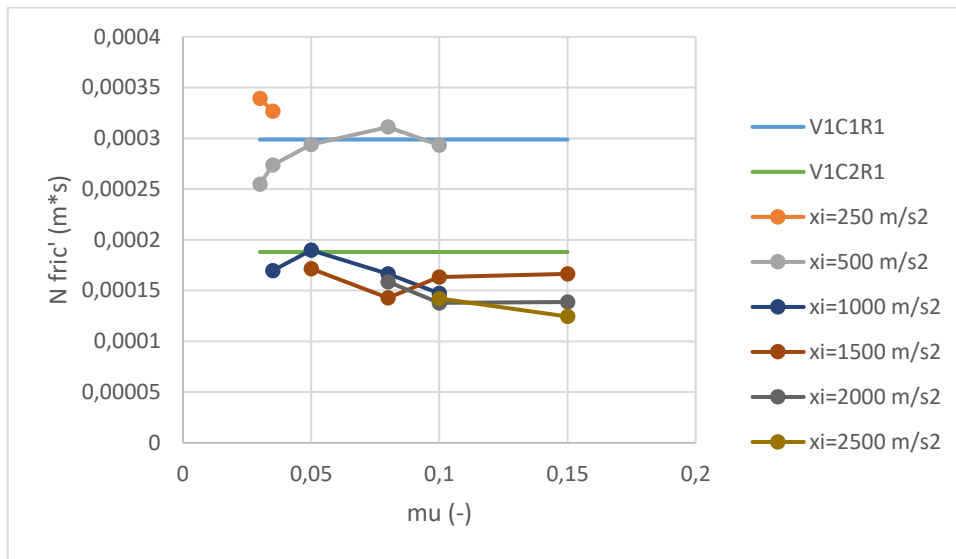


Figure 85: N'_{fric} at -1 m, in function of μ and ξ (series at constant ξ)

4.3. Parameter calibration

Based on the several numerical tests summarized previously, it is possible to calibrate the parameters of the Voellmy rheology (i.e. ξ and μ) to simulate the laboratory test results. In particular, in this section, it will be discussed the calibration of the tests with the material G2 and volume 1 (25 L) and for concentrations 1 (60%) and 2 (55%).

Calibration is performed taking into account two distinct phases:

- The behaviour along the channel (in particular at -2 m and -1 m). Velocity and flow height are not considered separately, since this would give erroneous results (as discussed in the previous section), but through the Froude number and the dimensionless parameters.
- The deposition. The numerical model considered here is not able to replicate the deposit shape: only the runout length will be considered.

First, the parameter ξ is calibrated based on the behaviour in the channel, i.e. considering the Froude and the dimensionless numbers and using the plots in Figures 72,

73 and 80 to 85 (curves at constant ξ). In fact, these dynamic parameters mainly depend on ξ .

Then, for the selected value of ξ , the correct value of μ is chosen by looking at the runout distance (Figure 64, with curves at constant μ).

The dynamic behaviour of the test G2V1C1R1 is well simulated by $\xi=500 \text{ m/s}^2$. The simulated values of the Froude number are a bit lower than the experimental ones. However, the dimensionless parameters are well replicated. Finally, the value $\mu=0.05$ (with $\xi=500 \text{ m/s}^2$) simulates the runout distance.

The dynamic behaviour of the test G2V1C2R1 can be simulated by both $\xi=1000 \text{ m/s}^2$ and $\xi=1500 \text{ m/s}^2$. In the first case, $\mu=0.035$ should be chosen to simulate the runout distance, while, in the second case, $\mu=0.05$ should be selected.

A summary of the selected parameters (with the ratio of the simulated value over the experimental one) is reported in table 12. These values are able to well simulate the runout distance, Froude number and dimensionless parameters at -1 m. The calibration is not precise, as it is not able to model exactly all the dynamic and depositional features. Testing more values of ξ and μ could give more precise results, as well as introducing an active/passive earth-pressure coefficient. Furthermore, it should also be considered that the experimental results (and in particular the flow velocity) are subjected to an error, as discussed in chapter 2.4.1.

TEST	ξ (m/s^2)	μ (-)	%Runout	%Fr @-2 m	%Fr @-1 m	%N'Sav @-2 m	%N'Bag @-2 m	%N'fric @-2 m	%N'Sav @-1 m	%N'Bag @-1 m	%N'fric @-1 m
G2V1C1R1	500	0.05	93%	82%	84%	117%	94%	80%	91%	90%	98%
G2V1C2R1	1000	0.035	111%	97%	86%	221%	120%	54%	103%	94%	90%
	1500	0.05	109%	108%	94%	323%	139%	43%	108%	99%	91%

Table 12: selected parameters and ratios between the simulated value over the experimental one

4.4. Discussion

The results obtained through the numerical simulation are able to well represent the laboratory test results, in terms of runout distance and dimensionless parameters. However, the flow front and deposit shape cannot be correctly simulated. The introduction of an active/passive earth-pressure coefficient could give better results for the deposition stage. Improving the flume walls can, on the other hand, give more meaningful output during the runout stage.

The calibrated values of ξ and μ allow to show the influence of solid concentration on the parameters and to compare them to the typical values of natural debris flows.

An important preliminary observation is that the calibrated value of μ (0.05 or 0.035) is approximately equal to the tangent of the slope angle of the deposition zone ($\tan(2^\circ)$). This experimental correlation is thus verified.

Decreasing the solid concentration from 60% to 55% leads to an increase of ξ from 500 m/s^2 to 1000 m/s^2 (or 1500 m/s^2), which means an increase of the collisional behaviour. This has already been observed with the experimental results. Decreasing the concentration also cause a decrease of μ from 0.05 to 0.035: this corresponds to the decrease of the importance of frictional behaviour.

The obtained values of μ and ξ can be compared to the ones suggested by the RAMMS manual and to some values calibrated on natural debris flows (e.g. Hungr and Evans, 1996). The values of μ are close to the lower suggested boundary (0.05), while the values of ξ are close to the upper boundary (1000 m/s^2). This indicates that such kind of small-scale tests are representative of low friction and highly turbulent debris flows.

5. Conclusions

Laboratory tests on debris flows were run to simulate real debris flows with a scale of 1/20. The results can be considered meaningful, as typical characteristics of debris flows are maintained, such as longitudinal grain segregation, coarser flow front, liquefied tail, levees formation.

The influence of release volume (25 L, 30 L, 35L) and sediment concentration (60%, 55%, 50%) was studied. Sediment concentration was found to be the parameter that mostly affects the behaviour. Its increase determines a decrease of runout distance, deposit width, flow velocity and Froude number. The effect on flow height is not clear. Volume increase determines an increase of flow height and runout distance.

The repeatability of runout distance is high. A linear relationship between runout length and sediment concentration was found. Runout distance varies between 2.23 m and 4.5 m: the effect of sediment concentration (from 60% to 50%) is therefore important. The other parameters (flow height, flow velocity) show a lower repeatability and trends are less evident.

Froude number, which is a representative parameter for the scaling issues, was found to vary between 4 and 8, while the full-scale debris flows show a typical value of 3. The high Froude numbers are a consequence of the thin and fast flows generated in these small-scale experiments. Even other laboratory experiments on debris flows presented such high values (Braat, 2014; Iverson, 1997).

To understand the influence of the scale on the debris flow behaviour, dimensionless parameters were calculated, with a particular regard to Savage, Bagnold and friction numbers. The values obtained showed that the three mechanisms of stress generation, i.e. collisional, viscous and frictional, have almost the same importance, while, in full-scale debris flows, friction dominates on viscosity which in turn dominates on collisions. Collisional stresses are therefore overestimated, which can be considered a consequence of the small-scale, since the dimensionless parameters have similar values of other laboratory tests (Braat, 2014; USGS test, Iverson, 1997).

To overcome these issues, testing debris flows with a sediment concentration higher than 60% could create a thicker and slower flow with the consequent reduction of Froude number and Savage and Bagnold numbers. However, very high concentrations may create a too dry material, which could be more like rock avalanches. Furthermore, also a rougher flowing surface would slow down the flow. This solution is however not easy to be applied, since the cleaning of the model would be longer and difficult.

Regarding the measurements on the flow, an attempt could be made to improve the pore pressure readings, which, in these experiments, were not correct and probably affected by grain collisions. The analysis of the force measurements, and its correlation to sediment concentration and release volume can be the basis of further works.

The numerical simulation of these laboratory tests with RAMMS::Debris flow software was an issue. Some simplifications had to be made, in particular for the release mechanism and the lateral walls of the flume.

The Voellmy rheology was used and the parameters - μ and ξ - were calibrated to match with Froude and dimensionless numbers along the channel (for ξ) and with runout distance (for μ). A complete representation of the flow was not possible. Flow velocities and flow heights could not be well represented, which is probably affected by the frictionless walls and by the mono-phase material considered by the software. The elongated deposition shape, observed experimentally, was impossible to be reproduced, which could be due to the use of the earth-pressure coefficient equal to 1. The introduction of active/passive earth-pressure coefficients, differentiated in the two orthogonal directions, could lead to better results (Gray et al., 1999). Furthermore, to overcome all these issues, other rheology could be tested in further works.

References

- Armanini, A. 1997. On the dynamic impact of debris flows. In: Armanini A, Masanori M (eds) Recent developments on debris flows, lecture notes in earth sciences, Springer, Berlin. 208–226.
- Bagnold, R. A., and F. R. S. 1954. ‘Experiments on a Gravity-Free Dispersion of Large Solid Spheres in a Newtonian Fluid under Shear’. *Proc. R. Soc. Lond. A* 225 (1160): 49–63.
- Bartlet, Bieler, Buehler, Christen, Deubelbeiss, Graf, McArdeell, Salz, Schneider. 2017. RAMMS User Manual v1.7.0 Debris Flow. In: WSL-SLF (ed.). Switzerland.
- Bettella, Bisantino, D’Agostino, Gentile. 2012. Debris-flow runout distance: laboratory experiments on the role of Bagnold, Savage and friction numbers. *WIT Transactions on Engineering Sciences, Vol 73*. 27-36.
- Braat, L., 2014. *Debris flows on Mars: An experimental analysis*. University Utrecht.
- Calligaris, C., and Zini, L. 2012. Debris Flow Phenomena: A Short Overview?. INTECH Open Access Publisher.
- Christen, M., Kowalski, J., Bartelt, P. 2010. RAMMS: Numerical simulation of dense snow avalanches in three-dimensional terrain. *Cold Regions Science and Technology*. 63. 1-14.
- Christiansen, L. F. (2013). Flomskred: Litteraturstudie og modellforsøk med voller som sikringstiltak. Institutt for bygg, anlegg og transport.
- Coussot, P., and M. Meunier. 1996. ‘Recognition, Classification and Mechanical Description of Debris Flows’. *Earth-Science Reviews* 40 (3): 209–27.
- Costa, J. E. 1984. Physical geomorphology of debris flows Developments and applications of geomorphology. *Springer*. 268-317.
- Crowe, C. T., Elger, D. F., Williams, B. C., & Roberson, J. A. 2009. Dimensional analysis and similitude Engineering fluid mechanics. 249-273. John Wiley & Sons, Inc.

- De Blasio, Breien, Elverhøi. 2011. Modelling a cohesive-frictional debris flow: an experimental, theoretical, and field-based study. *Earth Surf. Process. Landforms* 36. 753–766.
- Denlinger, Roger P., and Richard M. Iverson. 2001. 'Flow of Variably Fluidized Granular Masses across Three-Dimensional Terrain: 2. Numerical Predictions and Experimental Tests'. *Journal of Geophysical Research: Solid Earth* 106 (B1): 553–66.
- Fisher, Richard V. 1971. 'Features of Coarse-Grained, High-Concentration Fluids and Their Deposits'. *Journal of Sedimentary Research* 41 (4): 916–27.
- Fiskum, E. 2012., Flomskred: Testing av ulike sikringstiltak i modellforsøk: Institutt for bygg, anlegg og transport.
- Gray, J. M. N. T., Wieland, M., Hutter, K. 1999. Gravity-driven free surface flow of granular avalanches over complex basal topography. *Proc. R. Soc. Lond. A.* 455. 1841-1874.
- Heller, P., & Jenssen, L. 2009. Modellforsøk med flomskred mot bruer : virkning av bruåpning og ledevoller Teknologi-rapport (online), Vol. nr. 2582.
- Holmes, J. L., 2017. *An Assessment of Experimental Debris-Flow Scaling Relationships*. Durham University.
- Huang, Yang, Lai. 2007. *Impact Force of Debris Flow on Filter Dam*.
- Hungr O. 1995. 'A Model for the Runout Analysis of Rapid Flow Slides, Debris Flows, and Avalanches'. *Canadian Geotechnical Journal* 32 (4): 610–23.
- Hungr, O., and Evans, S. Rock avalanche runout prediction using a dynamic model. *Proceedings of the 7th International Symposium on Landslides, Trondheim, Norway.* 21. 1996.
- Hungr, Oldrich, S. G. Evans, M. J. Bovis, and Hutchinson J. N. 2001. 'A Review of the Classification of Landslides of the Flow Type'. *Environmental and Engineering Geoscience* 7 (3): 221–38.
- Iverson, R. M., and Denlinger, R. P. 1987. The physics of debris flows - a conceptual assessment. *Erosion and Sedimentation in the Pacific Rim (Proceedings of the Corvallis Symposium, August, 1987).* 155-165.

Iverson, R.M., and R.G. LaHusen. 1993. Friction in debris flows: Inferences from large-scale flume experiments: Hydraulic Engineering '93. *Proceedings of the 1993 Conference of the Hydraulics Division of the American Society of Civil Engineers*. v. 2. 1604-1609

Iverson, Richard M. 1997. 'The Physics of Debris Flows'. *Reviews of Geophysics* 35 (3): 245–96.

Iverson, Richard M., Matthew Logan, and Roger P. Denlinger. 2004. 'Granular Avalanches across Irregular Three-Dimensional Terrain: 2. Experimental Tests'. *Journal of Geophysical Research: Earth Surface* 109 (F1): F01015.

Iverson, Richard M., Matthew Logan, Richard G. LaHusen, and Matteo Berti. 2010. 'The Perfect Debris Flow? Aggregated Results from 28 Large-Scale Experiments'. *Journal of Geophysical Research: Earth Surface* 115 (F3): F03005.

Jakob, Matthias, and Oldrich Hungr. 2005. *Debris-Flow Hazards and Related Phenomena*. Geophysical Sciences. Berlin Heidelberg: Springer-Verlag.

Laache, E., 2016. *Model Testing of the Drainage Screen Type Debris Flow Breaker*. NTNU.

Lichtenhahn, C. 1973. 'Die Berechnung von Sperren in Beton und Eisenbeton'. In: *Kolloquium u"ber Wildbachsperren, Mitteilungen der Forstlichen Bundesanstalt Wien*, vol 102, 91–127.

Major, J.J. 1997. 'Depositional Processes in Large-Scale Debris-Flow Experiments'. *Journal of Geology* 105 (3): 22.

Ogawa, S. 1978. Multi-temperature theory of granular materials. *Proceedings US-Japan Seminars on Continuum-Mechanics and Statistical Approaches to Mechanical Granular Materials*. 208-217.

Parsons, J. D., K. X. Whipple, and A. Simoni. 2001. 'Experimental Study of the Grain Flow, Fluid-Mud Transition in Debris Flows'. *Journal of Geology* 109 (4): 427–47.

Pierson, Thomas C., and Kevin M. Scott. 1985. 'Downstream Dilution of a Lahar: Transition from Debris Flow to Hyperconcentrated Streamflow'. *Water Resources Research* 21 (10): 1511-1524.

Pierson, T. 1986. Flow behavior of channelized debris flows Mount St. Helens Washington. *Hillslope processes*. 269-296.

Pierson, T. C., and Costa, J. E. 1987. 'A rheologic classification of subaerial sediment-water flows'. *Reviews in Engineering Geology*. Volume VII. 1-12

Pirulli, M., 2005. *Numerical modelling of landslide runout. A continuum mechanics approach*. Politecnico di Torino.

Pouliquen, Olivier, and Yoël Forterre. 2002. 'Friction Law for Dense Granular Flows: Application to the Motion of a Mass down a Rough Inclined Plane'. *Journal of Fluid Mechanics* 453 (February): 133–51.

Pradhan, R. N., 2017. *Physical Modeling of Debris Flow by Varying Sediment Concentration*. NTNU.

Pudasaini, S.P., and Hutter, K. 2007. Saint-Venant Equations and Friction Law for Modelling Self-Channeling Granular Flows: From Analogue to Numerical Simulation. *Avalanche Dynamics*. Springer, Berlin.

Rodine, J. D., Johnson, A. M., Rich, E. I. 1974. Analysis of the Mobilization of Debris Flows. STANFORD UNIV CA DEPT OF GEOLOGY.

Savage, S. B., and K. Hutter. 1989. 'The Motion of a Finite Mass of Granular Material down a Rough Incline'. *Journal of Fluid Mechanics* 199 (February): 177–215.

Scheidl, Christian, Michael Chiari, Roland Kaitna, Matthias Müllegger, Alexander Krawtschuk, Thomas Zimmermann, and Dirk Proske. 2013. 'Analysing Debris-Flow Impact Models, Based on a Small Scale Modelling Approach'. *Surveys in Geophysics* 34 (1): 121–40.

Sherchan, B., 2016. *Entrainment of Bed Sediments by Debris Flow*. NTNU

Schlemon, Wright, Montgomery. 1987. Anatomy of a debris flow, Pacifica, California. *Reviews in Engineering geology, Volume VII*. 181-199.

Sosio, R., G. B. Crosta, and P. Frattini. 2007. 'Field Observations, Rheological Testing and Numerical Modelling of a Debris-Flow Event'. *Earth Surface Processes and Landforms* 32 (2): 290–306.

Takahashi, Tamotsu. 2014. *Debris Flow: Mechanics, Prediction and Countermeasures, 2nd edition*. CRC Press.

Varnes, D.J. 1958. LANDSLIDE TYPES AND PROCESSES. *Highway Research Board*. 20-47.

Varnes, D.J. 1978. Slope Movement Types and Processes. *Transportation Research Board*. 11-33.

Viccione, Genovese, Rossi. 2015. Physical modelling of laboratory debris flows by using the Sodium Carboxymethylcellulose (Na-CMC). *WSEAS TRANSACTIONS on FLUID MECHANICS*. 163-173.

Yifru, A. L., 2014. *Assessment of Rheological Models for Run-out Distance Modeling of Sensitive Clay Slides, Focusing on Voellmy Rheology*. NTNU.

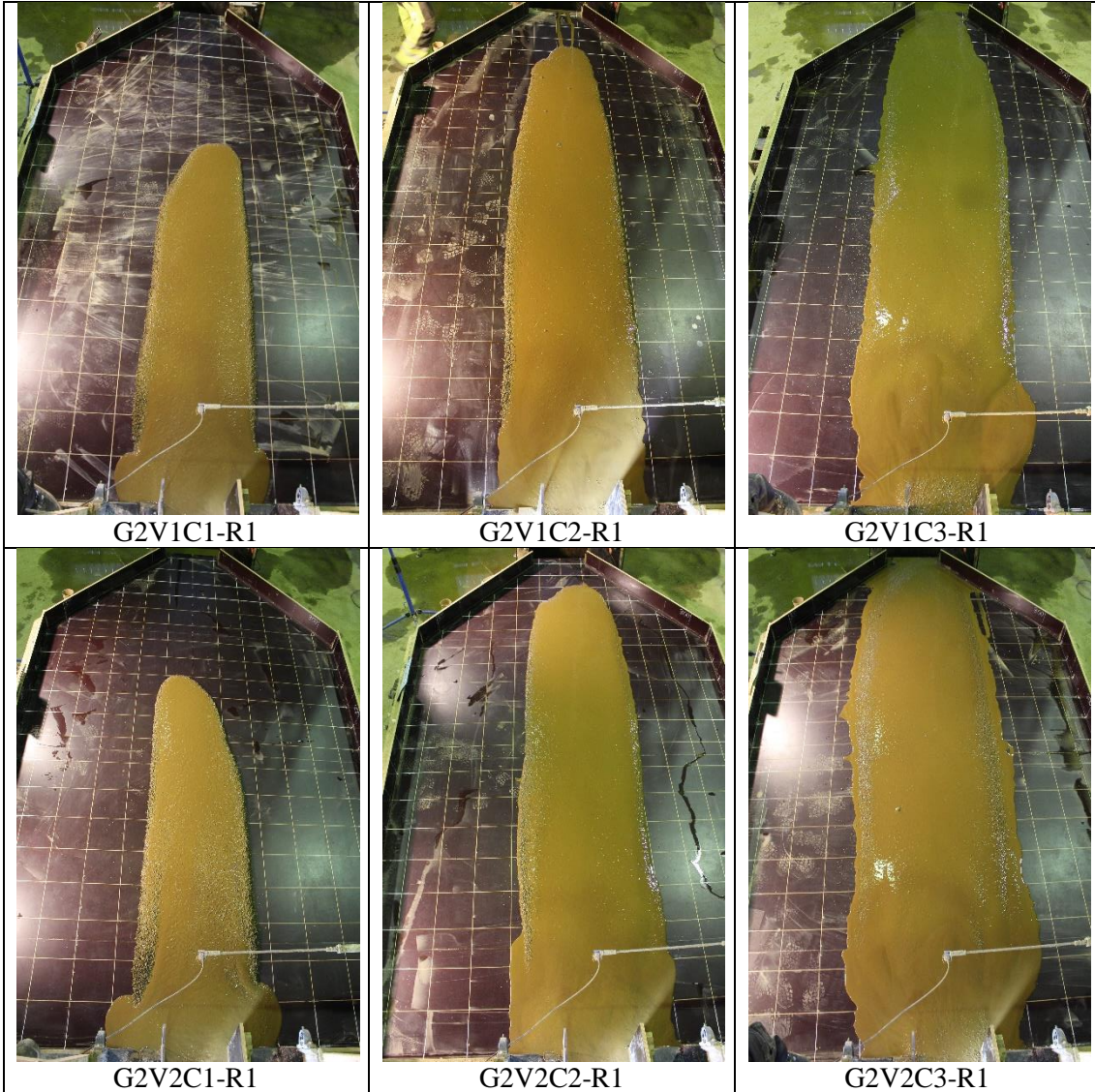
Appendix 1: results of laboratory flume tests (G2)

Name	V [L]	Cs	Runout [m]	Maximum Height @-3 m [cm]	Front Velocity @-2 m [m/s]	Maximum Height @-2 m [cm]	Front Velocity @-1 m [m/s]	Maximum Height @-1 m [cm]	Front Velocity @-0.2 m [m/s]	Maximum Height @0.4 m [cm]
G2v1c1-r1	25	60%	2.32	5	2.8	3.96	2.28	2.61	2.9	2.41
G2v1c1-r2	25	60%	2.23	4.6	2.75	3.98	2.28	2.31	2.81	2.53
G2v1c1-r3	25	60%		4.79	2.57	4.01	2.31	2.68	2.59	2.29
G2v1c2-r1	25	55%	3.48	7.5	3.68	2.9	3.32	2.5	3.16	2.4
G2v1c2-r2	25	55%	3.55	8.45	3.35	3.4	3.69	2.65	3.03	2.07
G2v1c2-r3	25	55%			3.92		3.55		3.32	
G2v1c3-r1	25	50%	4.3	8.8	4.23	2.8	3.98	3.3	3.99	2.02
G2v1c3-r2										
G2v1c3-r3	25	50%		10.82	3.57	2.47	3.76	2.71	3.34	1.67
G2v2c1-r1	30	60%	2.4	5.51	2.56	4.35	2.64	2.95	2.65	2.84
G2v2c1-r2	30	60%	2.41	5.12	2.7	3.78	2.58	3.19	2.86	2.61
G2v2c1-r3	30	60%		4.13	2.91	3.38	2.63	2.44	2.73	2.17
G2v2c2-r1	30	55%	3.6	5.89	4.11	3.11	3.22	2.84	3.13	2.13
G2v2c2-r2	30	55%	3.6	6.23	3.1	3	3.81	2.6	3.55	2.55
G2v2c2-r3	30	55%		7.96	3.51	3.28	3.15	2.57	3.26	1.74
G2v2c3-r1	30	50%	4.2	8.71	4.05	3.04	3.7	3.27	4.12	2.42
G2v2c3-r2										
G2v2c3-r3	30	50%		9.82	3.01	2.98	3.89	3.41	4.04	2.03
G2v3c1-r1	35	60%	2.68	6.13	3.07	4.4	2.9	3.04	3.32	2.54
G2v3c1-r2										
G2v3c1-r3	35	60%		6.86	3.17	5.3	3.12	3.45	3.52	2.29
G2v3c2-r1	35	55%	4	9.91	3.23	3.12	3.56	3.25	3.79	2.64
G2v3c2-r2										
G2v3c2-r3	35	55%		12.31	3.93	2.99	3.63	3.52	3.82	2.08
G2v3c3-r1	35	50%	4.5	13.92	4.09	3.79	3.95	3.98	3.14	2.88
G2v3c3-r2										
G2v3c3-r3	35	50%		9.93	3.28	2.8	3.74	3.7	4.29	2.1

Appendix 2: results of laboratory flume tests (G1)

Name	V [L]	Cs	Runout [m]	Maximum Height @-3 m [cm]	Front Velocity @-2 m [m/s]	Maximum Height @-2 m [cm]	Front Velocity @-1 m [m/s]	Maximum Height @-1 m [cm]	Front Velocity @-0.2 m [m/s]	Maximum Height @0.4 m [cm]
G1v1c1-r1	25	60%	1.89							
G1v1c1-r2	25	60%		4.89	2.86	3.79	2.84	3.27	3.01	2.84
G1v1c3-r1	25	50%	3.78	7.91	4.08	2.81	3.78	2.73	3.72	2.25
G1v2c1-r1	30	60%								
G1v2c1-r2	30	60%								
G1v2c2-r1	30	55%	3.75							
G1v2c2-r2	30	55%	3.75	6.67	3.75	3.61	3.64	3.10	3.69	2.61
G1v3c3-r1	35	50%	4	9.18	3.77	3.56	3.84	2.77	3.62	2.40

Appendix 3: deposition shape (G2, repetition 1)





G2V3C1-R1



G2V3C2-R1



G2V3C3-R1

Appendix 4: force measurement and impact pressure calculation

Name	V [L]	Cs	Fmax [N]	p [Pa]	p hyro [Pa]	k	p kin [Pa]	a
G2v1c1-r3	25	60%	13.80	20565	460	44.7	13387	0.65
G2v1c2-r3	25	55%	-					
G2v1c3-r3	25	50%	14.91	21978	308	71.5	22357	1.02
G2v2c1-r3	30	60%	10.38	17057	436	39.1	14877	0.87
G2v2c2-r3	30	55%	19.26	30008	336	89.4	21259	0.71
G2v2c3-r3	30	50%	19.15	22484	373	60.3	32652	1.45
G2v3c1-r3	35	60%	12.10	14041	460	30.5	24731	1.76
G2v3c2-r3	35	55%	17.80	20204	399	50.6	29154	1.44
G2v3c3-r3	35	50%	15.65	16904	385	43.9	36874	2.18

Appendix 5: calculation of dimensionless numbers

Name	v _{fin}	Viscosity [Pa.s]	ρ _f [kg/m ³]	-2 m					
				Fr	N	dy/dt [1/s]	NSav	N _{Bag}	N _{fric}
G2v1c1-r1	0.13	0.00133	1243	4.5	45.2	70.7	0.049	168.3	3400.6
G2v1c1-r2	0.13	0.00133	1243	4.4	45.4	69.2	0.047	164.7	3490.6
G2v1c1-r3	0.13	0.00133	1243	4.1	45.8	64.1	0.04	152.5	3800.4
G2v1c2-r1	0.11	0.00127	1201	6.9	33.1	127	0.212	257.1	1213.8
G2v1c2-r2	0.11	0.00127	1201	5.8	38.8	98.6	0.109	199.7	1831.1
G2v1c2-r3	0.11	0.00127	1201						
G2v1c3-r1	0.09	0.00123	1166	8.1	31.9	151.3	0.305	260.3	852.4
G2v1c3-r2	0.09	0.00123	1166						
G2v1c3-r3	0.09	0.00123	1166	7.3	28.2	144.8	0.317	249.1	785.8
G2v2c1-r1	0.13	0.00133	1243	3.9	49.7	58.8	0.031	140	4488.3
G2v2c1-r2	0.13	0.00133	1243	4.4	43.2	71.4	0.053	169.9	3214.8
G2v2c1-r3	0.13	0.00133	1243	5	38.6	85.9	0.086	204.5	2389.5
G2v2c2-r1	0.11	0.00127	1201	7.4	35.5	132.1	0.214	267.5	1250.8
G2v2c2-r2	0.11	0.00127	1201	5.7	34.2	103.3	0.136	209.2	1542.6
G2v2c2-r3	0.11	0.00127	1201	6.2	37.4	107.2	0.134	217.2	1623.8
G2v2c3-r1	0.09	0.00123	1166	7.4	34.7	133.3	0.218	229.3	1053.2
G2v2c3-r2	0.09	0.00123	1166						
G2v2c3-r3	0.09	0.00123	1166	5.6	34	100.9	0.127	173.6	1363
G2v3c1-r1	0.13	0.00133	1243	4.7	50.2	69.8	0.043	166.2	3822
G2v3c1-r2	0.13	0.00133	1243						
G2v3c1-r3	0.13	0.00133	1243	4.4	60.5	59.8	0.026	142.3	5381.2
G2v3c2-r1	0.11	0.00127	1201	5.8	35.6	103.6	0.131	209.8	1597.7
G2v3c2-r2	0.11	0.00127	1201						
G2v3c2-r3	0.11	0.00127	1201	7.2	34.2	131.1	0.219	265.6	1213.1
G2v3c3-r1	0.09	0.00123	1166	6.7	43.2	108.1	0.115	186	1615.8
G2v3c3-r2	0.09	0.00123	1166						
G2v3c3-r3	0.09	0.00123	1166	6.3	31.9	117.1	0.183	201.5	1102

Name	vfines	Viscosity [Pa.s]	ρf [kg/m ³]	-1 m					
				Fr	N	dy/dt [1/s]	NSav	NBag	Nfric
G2v1c1-r1	0.13	0.00133	1243	4.5	29.8	87.4	0.115	207.9	1814.9
G2v1c1-r2	0.13	0.00133	1243	4.8	26.4	98.5	0.164	234.4	1426.4
G2v1c1-r3	0.13	0.00133	1243	4.5	30.7	86	0.108	204.7	1895.4
G2v1c2-r1	0.11	0.00127	1201	6.7	28.6	132.9	0.269	269.3	999.3
G2v1c2-r2	0.11	0.00127	1201	7.2	30.3	138.9	0.277	281.3	1015.9
G2v1c2-r3	0.11	0.00127	1201						
G2v1c3-r1	0.09	0.00123	1166	7	37.7	120.4	0.163	207.1	1266.7
G2v1c3-r2	0.09	0.00123	1166						
G2v1c3-r3	0.09	0.00123	1166	7.3	31	138.5	0.263	238.2	904.2
G2v2c1-r1	0.13	0.00133	1243	4.9	33.7	89.3	0.106	212.4	2009.3
G2v2c1-r2	0.13	0.00133	1243	4.6	36.4	81.1	0.081	193	2384.8
G2v2c1-r3	0.13	0.00133	1243	5.4	27.8	108	0.188	257	1369.2
G2v2c2-r1	0.11	0.00127	1201	6.1	32.4	113.5	0.173	229.9	1329.3
G2v2c2-r2	0.11	0.00127	1201	7.5	29.7	146.5	0.315	296.7	942.4
G2v2c2-r3	0.11	0.00127	1201	6.3	29.3	122.5	0.223	248.2	1113.3
G2v2c3-r1	0.09	0.00123	1166	6.5	37.3	113.2	0.146	194.8	1332.4
G2v2c3-r2	0.09	0.00123	1166						
G2v2c3-r3	0.09	0.00123	1166	6.7	38.9	114.2	0.143	196.5	1376.2
G2v3c1-r1	0.13	0.00133	1243	5.3	34.7	95.5	0.118	227.3	1930.9
G2v3c1-r2	0.13	0.00133	1243						
G2v3c1-r3	0.13	0.00133	1243	5.4	39.4	90.4	0.093	215.2	2313.8
G2v3c2-r1	0.11	0.00127	1201	6.3	37.2	109.5	0.14	221.8	1579.1
G2v3c2-r2	0.11	0.00127	1201						
G2v3c2-r3	0.11	0.00127	1201	6.2	40.3	102.9	0.114	208.4	1820.6
G2v3c3-r1	0.09	0.00123	1166	6.3	45.5	99.1	0.092	170.4	1855.9
G2v3c3-r2	0.09	0.00123	1166						
G2v3c3-r3	0.09	0.00123	1166	6.2	42.3	101.1	0.103	173.9	1690.4

Appendix 6: input parameters for RAMMS simulation

The image displays two screenshots of the RAMMS Run Simulation dialog box, showing different tabs.

Left Screenshot: GENERAL SIMULATION INFORMATION

- General** | Params | Mu/Xi | Release | Erosion
- GENERAL SIMULATION INFORMATION**
- OUTPUT Name: T2
- Additional Information**
- Project name: T2
- Details: [Empty text area]
- Calculation domain: T2.dom
- Digital elevation info: T2.xyz
- Stop Parameter** ⓘ
- Percentage of total momentum (%): 5.00
- Save Max Values Only ("_Max" will be appended to the output name)
- Remarks**
- use "Escape" to close/cancel this window
- use "Ctrl+R" to start a simulation
- Run in background
- Cancel
- RUN SIMULATION

Right Screenshot: PARAMETERS

- General** | Params | Mu/Xi | Release | Erosion
- PARAMETERS**
- Simulation Parameters**
- Sim resolution (m): 0.01 (DEM: 0.01m)
- End time (s): 1000
- Dump step (s): 0.10
- Density (kg/m3): 2000.00
- Lambda (): 1.00 ⓘ
- Numerical Parameters**
- Numerical scheme: SecondOrder
- H Cutoff (m): 0.000001
- Miscellaneous Parameters**
- Obstacle/Dam File: NoFlux2.shp ⓘ
- Curvature: On Off
- Run in background
- Cancel
- RUN SIMULATION

RAMMS | Run Simulation




General Params Mu/Xi Release Erosion

MU/XI FRICTION PARAMETERS ?




Xi (m/s²): 500

Mu (): 0.05

Define additional MuXi areas

1st additional MuXi shapefile   

Xi (m/s²): 200 Mu (): 0.10




2nd additional MuXi shapefile   

Xi (m/s²): 200 Mu (): 0.10

YIELD STRESS ?

Be careful in using the yield stress parameter! Mu and Xi have to be newly calibrated when using this parameter! ^

Yield stress (Pa): 0.0

Yield stress zone:   

Run in background Cancel **RUN SIMULATION**

RAMMS | Run Simulation

General Params Mu/Xi Release Erosion



RELEASE PARAMETERS ? Use BLOCK release

Hydrograph Block Release

Block Release Information ?

Subtract release depth from DEM

Shapefile and Volume Information

Filename	Volume (m3)	Depth (m)	Delay (s)	
Release.shp	0.0	0.1	0.0	

Total Volume (m3) 0.0

Run in background Cancel **RUN SIMULATION**

Appendix 7: results of numerical simulations (RAMMS)

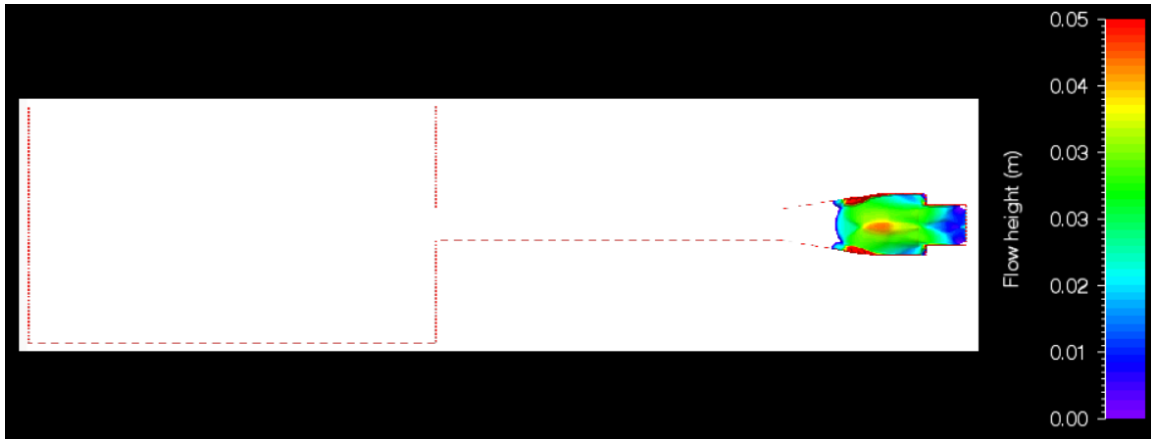


Figure i: flow height at $t=0.5$ s (for V1, $\mu=0.05$, $\xi=500$ m/s²)

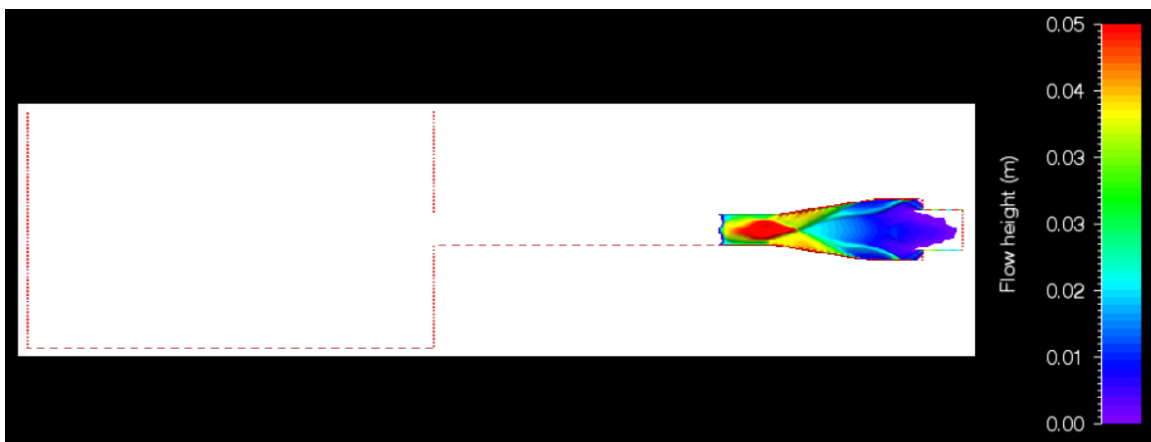


Figure ii: flow height at $t=1$ s (for V1, $\mu=0.05$, $\xi=500$ m/s²)

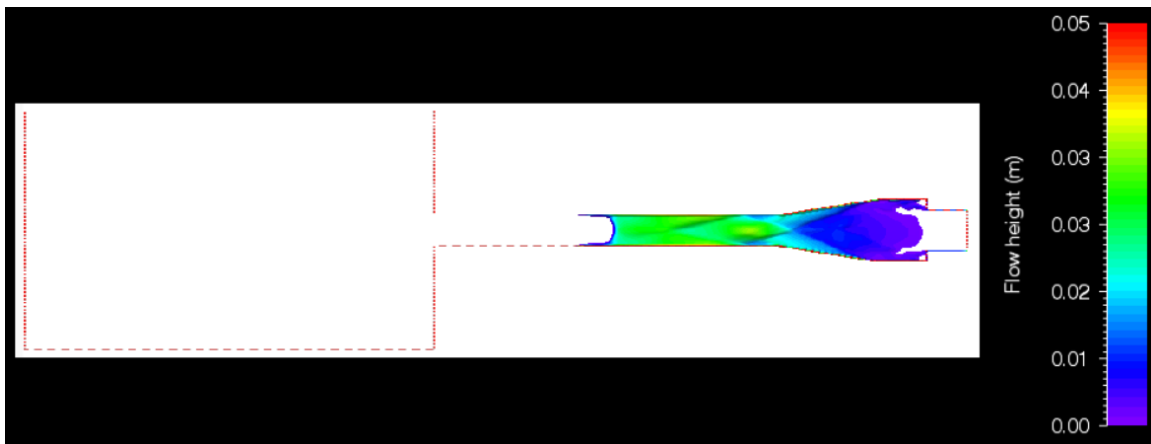


Figure iii: flow height at $t=1.5$ s (for V1, $\mu=0.05$, $\xi=500$ m/s²)

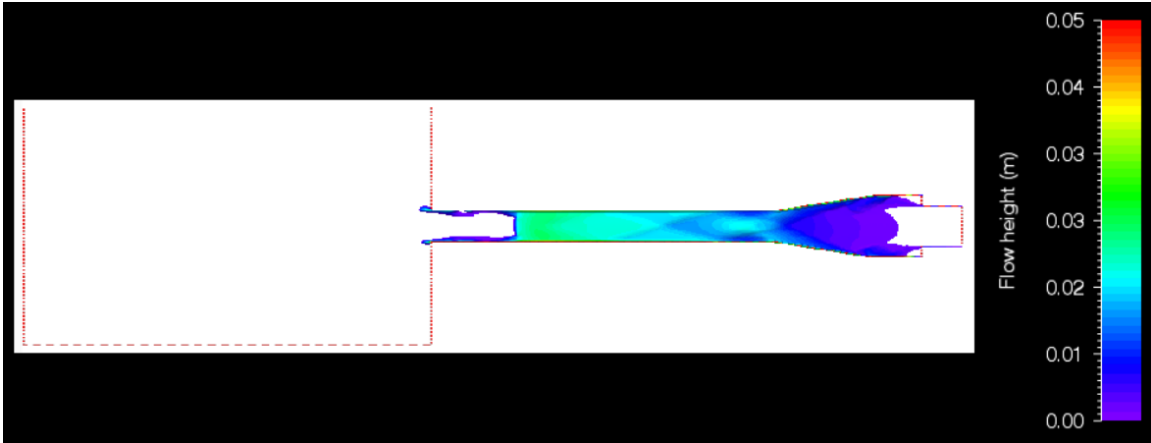


Figure iv: flow height at $t=2$ s (for V1, $\mu=0.05$, $\xi=500$ m/s²)

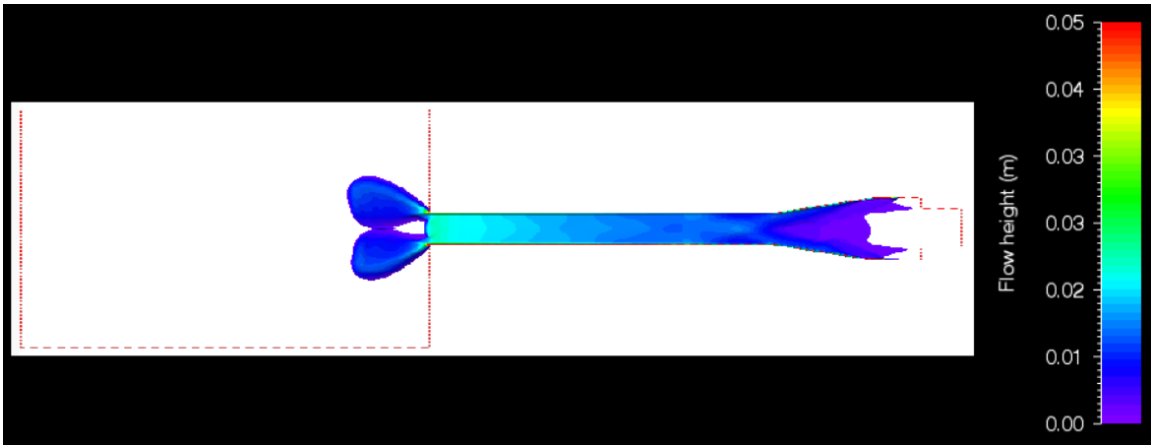


Figure v86: flow height at $t=2.5$ s (for V1, $\mu=0.05$, $\xi=500$ m/s²)

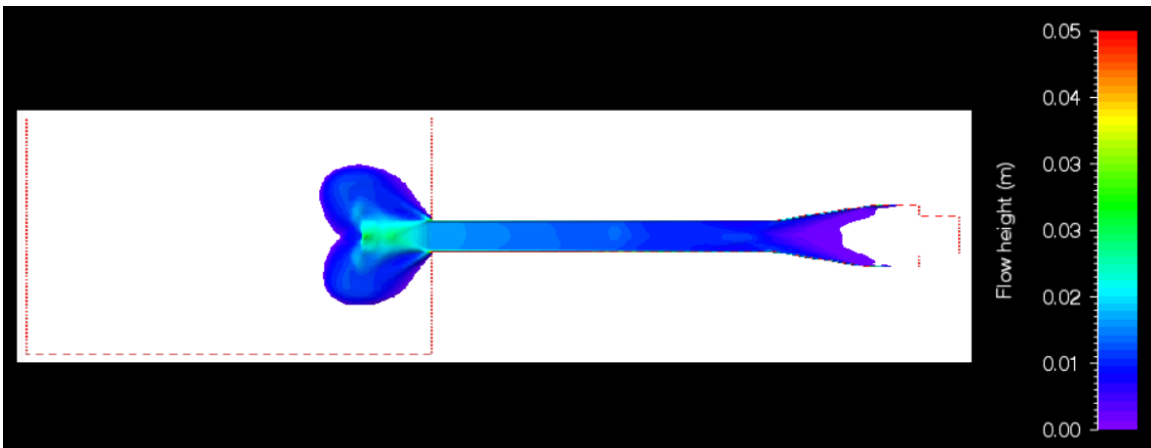


Figure vi: flow height at $t=3$ s (for V1, $\mu=0.05$, $\xi=500$ m/s²)

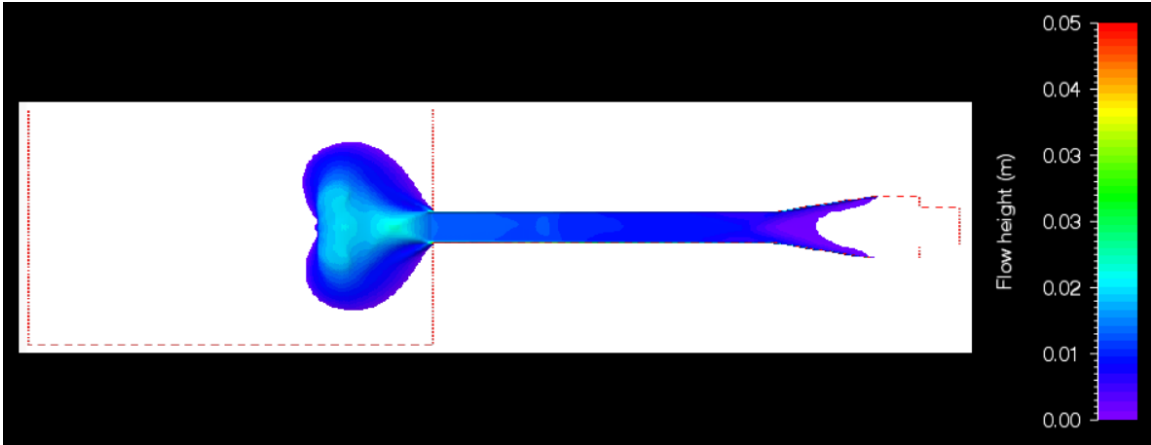


Figure vii: flow height at $t=3.5$ s (for VI, $\mu=0.05$, $\xi=500$ m/s²)

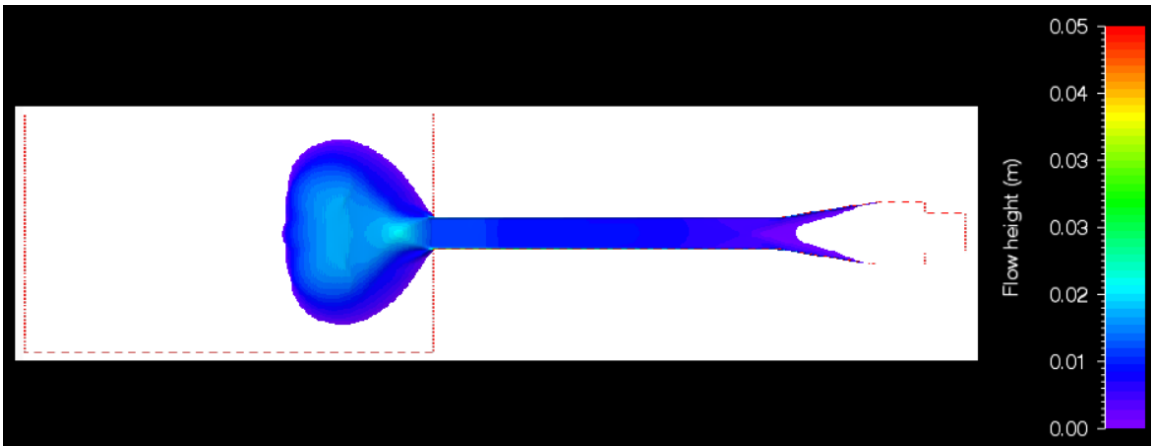


Figure viii: flow height at $t=4$ s (for VI, $\mu=0.05$, $\xi=500$ m/s²)

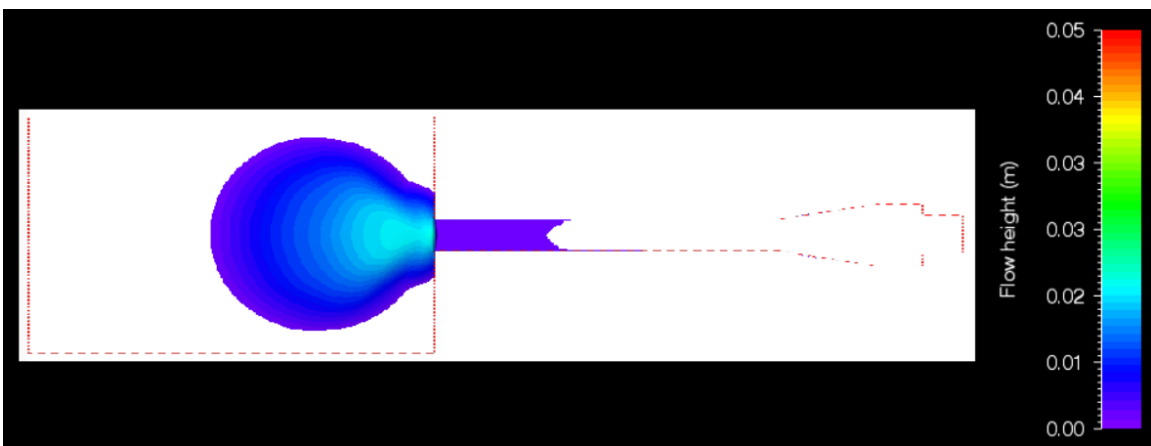


Figure ix: flow height at $t=10$ s (for VI, $\mu=0.05$, $\xi=500$ m/s²)